13. SITE 848[1]

Shipboard Scientific Party[2]

HOLE 848A

Date occupied: 4 June 1991

Date departed: 4 June 1991

Time on hole: 8 hr, 10 min

Position: 2°59.634′S, 110°28.791′W

Bottom felt (rig floor; m, drill-pipe measurement): 3865.1

Distance between rig floor and sea level (m): 11.7

Water depth (drill-pipe measurement from sea level, m): 3853.4

Total depth (rig floor, m): 3874.5

Penetration (m): 9.4

Number of cores (including cores with no recovery): 1

Total length of cored section (m): 9.4

Total core recovered (m): 9.54

Core recovery (%): 101.5

Oldest sediment cored:
Depth (mbsf): 9.4
Nature: diatom foraminifer nannofossil ooze
Earliest age: Pleistocene

HOLE 848B

Date occupied: 4 June 1991

Date departed: 5 June 1991

Time on hole: 20 hr, 11 min

Position: 2°59.634′S, 110°28.791′W

Bottom felt (rig floor; m, drill-pipe measurement): 3867.3

Distance between rig floor and sea level (m): 11.7

Water depth (drill-pipe measurement from sea level, m): 3855.6

Total depth (rig floor, m): 3961.1

Penetration (m): 93.8

Number of cores (including cores with no recovery): 12

Total length of cored section (m): 93.8

Total core recoved (m): 97.75

Core recovery (%): 104.2

Oldest sediment cored:
Depth (mbsf): 93.8
Nature: foraminifer nannofossil ooze
Earliest age: late Miocene

HOLE 848C

Date occupied: 5 June 1991

Date departed: 6 June 1991

Time on hole: 13 hr, 59 min

Position: 2°59.651′S, 110°28.805′W

Bottom felt (rig floor; m, drill-pipe measurement): 3867.0

Distance between rig floor and sea level (m): 11.7

Water depth (drill-pipe measurement from sea level, m): 3855.3

Total depth (rig floor, m): 3961.2

Penetration (m): 94.2

Number of cores (including cores with no recovery): 11

Total length of cored section (m): 94.2

Total core recoved (m): 97.74

Core recovery (%): 103.8

Oldest sediment cored:
Depth (mbsf): 94.2
Nature: nannofossil ooze with foraminifers and radiolarians
Earliest age: late Miocene

HOLE 848D

Date occupied: 6 June 1991

Date departed: 6 June 1991

Time on hole: 20 hr, 20 min

Position: 2°59.660′S, 110°28.808′W

Bottom felt (rig floor; m, drill-pipe measurement): 3866.1

Distance between rig floor and sea level (m): 11.7

Water depth (drill-pipe measurement from sea level, m): 3854.4

Total depth (rig floor, m): 3960.0

Penetration (m): 93.9

Number of cores (including cores with no recovery): 10

Total length of cored section (m): 93.9

Total core recoved (m): 96.88

Core recovery (%): 103.2

Oldest sediment cored:
Depth (mbsf): 93.9
Nature: radiolarian foraminifer nannofossil ooze
Earliest age: late Miocene

Principal results: Site 848 (proposed Site WEQ-5) is the southernmost site of the western transect of Leg 138. This transect, situated along 110°W, was designed to sample the various elements of the equatorial circulation system in an area far removed from the influence of the eastern boundary of the Pacific Ocean. The transect also serves as the eastern end-member of a series of studies (Legs 85 and 130) aimed at understanding the regional and global response of the equatorial Pacific Ocean to changes in climate.

[1] Mayer, L., Pisias, N., Janecek, T., et al., 1992. *Proc. ODP, Init. Repts.,* 138: College Station, Tx (Ocean Drilling Program).
[2] Shipboard Scientific Party is as given in the list of participants preceding the contents.

Four holes were drilled at Site 848. Hole 848A was a single APC mud-line core dedicated to whole-round geochemical and physical property measurements. Hole 848B was APC-cored to 93.3 mbsf, at which depth the APC struck basement; small amounts of basaltic glass were recovered in the core catcher. One XCB core was attempted in basement, but the XCB returned empty. The section was repeated in Holes 848C (APC to 91 mbsf, one XCB to 94.2 mbsf) and 848D (93.9 mbsf) to assure continuous recovery and to provide the volume of material needed for high-resolution paleoceanographic studies. Real-time analysis of continuous GRAPE, susceptibility, and color reflectance measurements showed that, after triple coring, no gaps in sediment recovery remained in the section.

The sedimentary sequence can be described as a single lithologic unit dominated by foraminifer nannofossil ooze; carbonate contents typically are greater than 60%. Siliceous microfossils are present in minor amounts throughout the section; however, thin layers of diatom nannofossil ooze with radiolarians (containing up to 30% diatoms and increased radiolarian and clay percentages) are rhythmically interbedded throughout the entire sequence. Near the bottom of the section, the sediments are characterized by an increase in reddish-brown, semi-opaque oxides that represent the influence of hydrothermal deposition near the ridge crest.

Biostratigraphic age control was provided by all four of the chief planktonic microfossil groups, although their abundances and states of preservation were variable throughout. Radiolarians and diatoms are abundant, with moderate to good preservation from the upper Miocene to the Pleistocene, although the lower 10 m of the section was barren of diatoms. Calcareous nannofossils are generally abundant, with good to moderate preservation that allowed us to zone the entire section. Foraminifers are abundant in the upper Pleistocene, although their abundances and preservation deteriorate down the section.

The paleomagnetic signal at Site 848 was variable; polarity reversals were resolvable in the upper 47 mbsf (0–4.7 Ma) and in the interval from 72 mbsf to basement (6.8–10.5 Ma). The upper zone contains every major polarity chronozone and subchronozone between the Brunhes and the Thvera. At these low latitudes, polarity reversals were primarily identified by declination patterns. The success of the multishot tool in providing core orientation was directly responsible for providing this extremely rare, deep-ocean, equatorial Pacific Ocean magnetic reversal record. Once again, the susceptibility record proved to be valuable as an interhole correlation tool. The strength of both susceptibility and remanence intensity may be inversely correlated to both sedimentation rate and carbonate content, suggesting that recovery of the paleomagnetic record may be the result of increased carbonate dissolution that concentrated clay minerals.

The continuous sedimentary section spans the time interval from the Quaternary to the middle Miocene. Excellent biostratigraphic and magnetostratigraphic (in much of the section) controls resulted in a fairly detailed sedimentation rate curve. Sedimentation rates were relatively low (about 5 m/m.y.) in the early late Miocene and Pliocene and were elevated (greater than 15 m/m.y.) in the late Miocene and Pleistocene.

A single logging run using the geochemical tool was conducted in this short hole. While the geochemical log needs further shore-based processing, clearly, variations on many scales of calcium and silica are indicated as well as the presence of a zone of metalliferous sediments.

Interstitial water sampling shows that the influence of diagenesis was restricted to the top of the sediment column by the low sedimentation rates. Calcium, silica, strontium, and lithium values indicate that while some recrystallization occurs within the sediment column, it is limited. However, evidence for the alteration of basaltic basement exists in the profiles of sodium, chloride, alkalinity, magnesium, potassium, and silica, although this is restricted to the bottom of the hole.

We were impressed with the quality (as well as the quantity) of the core material and data that were collected as Leg 138 progressed. Continuous profiles of susceptibility, color, and GRAPE data proved invaluable as interhole correlation tools. These data also provided a means for intersite (and thus regional) correlations and for spectral tuning of stratigraphies necessary for extremely high-resolution paleoceanographic studies. The combination of these continuous data sets brought "joy to Mudville,"—the paleomagnetics doldrums had a short reprieve, and we continued to mine a unique accumulation of paleoceanographic "gold." At the conclusion of Site 848, we had completed 8.5 log(m^2kt; corrected).

BACKGROUND AND SCIENTIFIC OBJECTIVES

Site 848, the first site drilled along a north-south transect centered at 110°W, is located beneath the Southern Equatorial Current (SEC). This transect was designed to sample different elements of the equatorial circulation system in an area separated from the direct effects of the eastern boundary of the Pacific Ocean. Site 848 is located beneath the westward-flowing SEC (Fig. 1) and complements Site 846, which also is located within this current system, but within an area affected by the Peru Current (PC).

Site 848 is located on crust formed at the East Pacific Rise (Fig. 2) and, based on calculations of spreading rate and crustal subsidence, we expected the basement age to be about 10 Ma. Local topography at the site displays a north-south grain (Fig. 3), with the site located on the crest of a gentle topographic swell. To the west, both the surface and basement topographies become rugged, with a number of small peaks and troughs. However, the site is well removed from this area of rugged topography. Sediment cover here is much thinner than that at sites farther north, because this site has not yet passed under the equatorial divergence; the average sediment thickness in the area is approximately 110 m. The seismic section in the vicinity of the site (Fig. 4) shows numerous, apparently undisturbed, flat-lying reflectors, indicating pelagic depositional processes.

OPERATIONS

Transit from Site 847 to Site 848 (WEQ-5)

The transit from Sites 847 to 848 (proposed Site WEQ-5) covered 932 nmi at an average speed of 10 kt. At 0645 hr (all times in text refer to local time, L, where L = Universal Time Coordinated (UTC) minus 7 hr. All times in Table 1 are UTC) 4 June, the *JOIDES Resolution* slowed to 6 kt to deploy the seismic gear in preparation for the site survey. The survey covered 14 nmi at an average speed of 6 kt. At 0820L 4 June, a beacon was deployed at the proposed location. The *Resolution* returned to the location after a 10-min survey past the site, and hydrophones and thrusters were lowered by 0915L 4 June. The depth to the seafloor, based upon the precision depth recorder (PDR), was 3871.5 mbrf. As the drill string was lowered to the seafloor, the beacon pulse rate was switched to half rate. A backup beacon was quickly deployed, and the first beacon was successfully retrieved.

Hole 848A

This hole consisted of a single mud-line core dedicated to whole-round geochemical and physical property measurements. Pipe was lowered to 3865 mbrf, and the first (and only) piston core was recovered at 1655L 4 June. The core contained 9.54 m of sediment (Table 1).

Hole 848B

The pipe was raised to 3860 mbrf to provide a vertical offset from the previous hole. At 1800L 4 June, Core 138-848B-1H was taken, and 2.23 m of sediment was recovered to establish the mud line at 3867.3 mbrf.

APC-coring continued through Core 138-848B-10H (78.2–87.7 mbsf) with orientation beginning at Core 138-848B-4H. As Core 138-848B-11H was taken, the barrel hit a hard surface that prevented a full stroke. The core was retrieved with 5.6 m of sediment in the liner. Assuming that the barrel was advanced by the amount of recovery, basement contact was estimated at 93.2 mbsf.

In hopes of retrieving basement material, the drilling crew used the XCB to cut Core 138-848B-12X. After penetrating approximately 0.5 m, the barrel was retrieved, but no sediment or basement material was

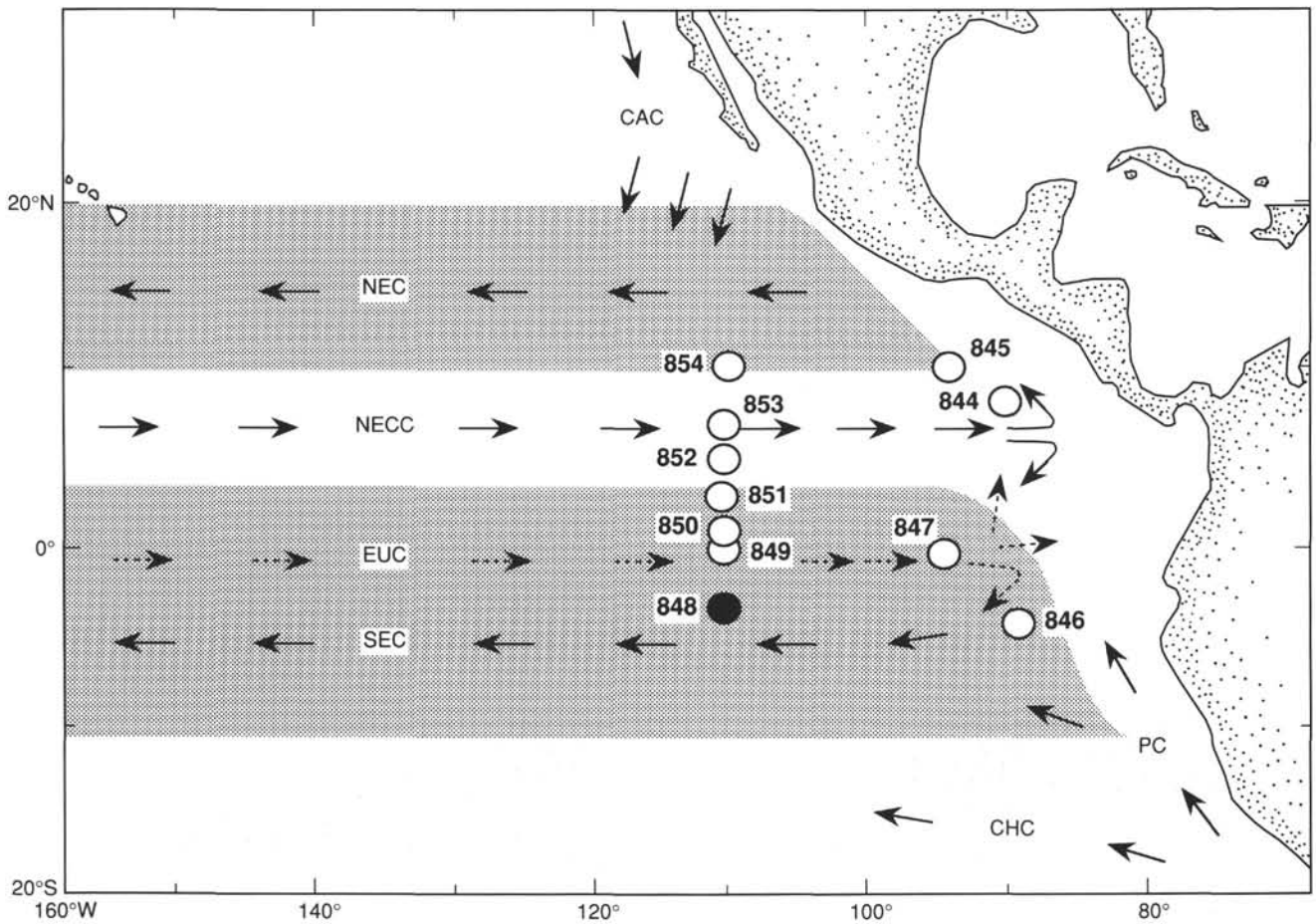

Figure 1. Location of Site 848 and generalized circulation system of the eastern equatorial Pacific Ocean. Other Leg 138 sites are shown for reference. Surface current shown as solid arrows; subsurface current as dashed arrows. CAC = California Current; NEC = North Equatorial Current; NECC = North Equatorial Countercurrent; EUC = Equatorial Undercurrent; SEC = South Equatorial Current; PC = Peru Current; and CHC = Chile Current. Shaded area illustrates general latitudinal extent of the SEC and NEC.

recovered. The coring program was terminated at this point, and the hole was prepared for logging. Recovery in the APC section was 104.3%.

Logging at Hole 848B

The hole was swept with mud and pipe was pulled to 88 mbsf in preparation for logging. Only the geochemical tool string was run because only 6 m of the hole was open below the pipe (Table 2). The geochemical tool string was lowered down the pipe after it had been rigged up and after it had been calibrated. At total depth (94.5 mbsf), the tool string was raised slowly while the geochemical spectral tool (GST) was calibrated. This calibration pass activated the bottom of the borehole, as one can see from the high natural gamma-ray counts recorded at the base of the hole during the main logging pass. In addition, a spike in the aluminum log was recorded at 63.3 mbsf in the borehole section opposite where the californium source in the aluminum clay tool (ACT) stopped. The tool string was lowered back to total depth (93.9 mbsf) after calibration for the main logging pass.

This log was run without the heave compensator to avoid differential motion between the pipe and the logging tool string. Had the heave compensator been on, heave in the pipe might have caught and broken the logging tool when it extended beyond the bit. The main logging pass was run from 93.9 mbsf to the mud line, when the tool string was pulled from the hole. After it was rigged down from logging, the top drive was set back, and the pipe pulled out of the hole. At 1241L 5 June, the mud line was cleared, ending Hole 848B.

Hole 848C

After the *JOIDES Resolution* was offset 20 m south, pipe was lowered to 3863 mbrf. The first piston core was taken at 1425L 5 June, and 5.47 m of sediment was retrieved, establishing the mud line at 3867.0 mbrf. APC-coring continued through Core 138-848C-10H (81.5–91.0 mbsf), with orientation beginning at Core 138-848C-4H.

The drilling crew used the XCB-coring system to cut Core 138-848C-11X because basement was approximately 3 m below the base of Core 138-848C-10H. After the barrel rotated approximately 45 min with a carbide-enhanced bit and advanced only 3.2 m, it was retrieved. The barrel contained 3.02 m of sediment, but the contact with basement was not recovered. Four of the five tungsten-carbine inserts on the bit were found to be missing and the cutting shoe surface had been severely worn.

At this point, the coring program was stopped in this hole, and pipe was pulled up to the mud line. The bit cleared the mud line at 0240L June 6, ending Hole 848C.

Hole 848D

The *JOIDES Resolution* was offset 20 m east, and the bit was lowered to 3865 m. Core 138-848D-1H was brought on deck at 0355L 6 June, and from it 8.44 m of sediment was recovered, establishing the mud line at 3866.1 mbrf. APC-coring continued routinely through Core 138-848D-7H (55.9–65.4 mbsf), with orientation beginning in

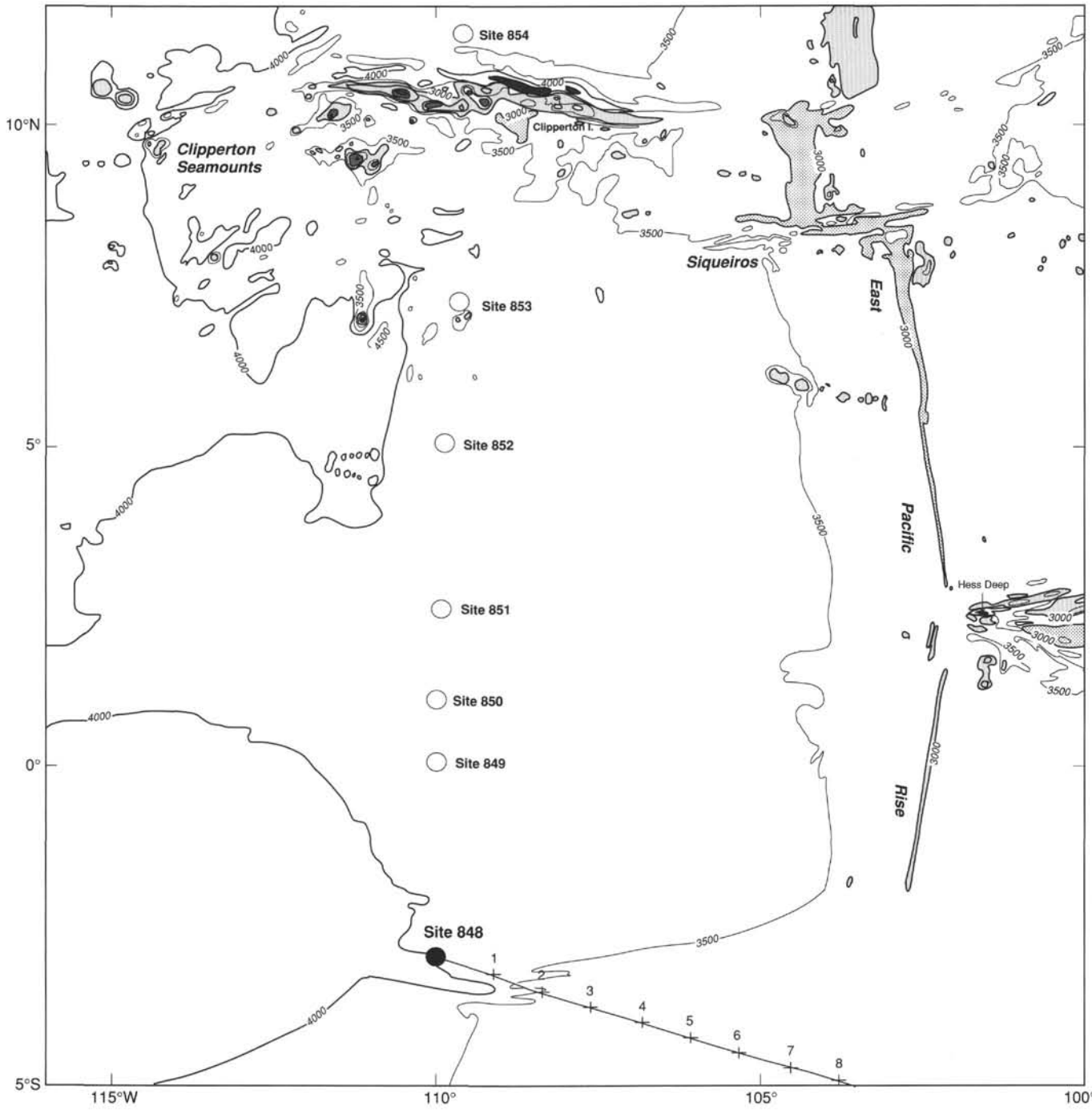

Figure 2. Generalized bathymetric map showing location of Site 848 and other Leg 138 sites drilled along the 110°W transect (from Mammerickx, 1989). Backtracked path of Site 848 shown in 1 m.y. increments for past 9 m.y.

Core 138-848D-4H. After Core 136-848D-7H was retrieved, the forward core line parted at the rope socket. The aft core line was then connected to the R/S overshot and run in the hole. The core barrel was retrieved successfully during the first fishing attempt.

The remaining three APC cores were obtained routinely to a depth of 93.9 mbsf. As the depth objective for this hole had been reached at this point, pipe was pulled out of the hole; the bit was on deck by 2217L 6 June. The rig floor was secured for the transit and hydrophones and thrusters were retracted; the vessel was under way to the next location by 2300L 6 June.

LITHOSTRATIGRAPHY

Introduction

A 94.2-m-thick section of Pleistocene to middle Miocene sediment was recovered at Site 848 in four holes. Hole 848A consists of one core, which was used to define the mud line. Coring intervals for Holes 848B, 848C, and 848D were slightly offset from each other to ensure complete recovery of the sedimentary sequence (Fig. 5). High-resolution lithologic parameters, such as GRAPE bulk density,

Table 1. Summary of coring operations at Site 848.

Core no.	Date (June 1991)	Time (UTC)	Depth (mbsf)	Length cored (m)	Length recovered (m)	Recovery (%)
138-848A-1H	04	2355	0–9.4	9.4	9.54	101.5
Coring totals				9.4	9.54	101.5
138-848B-1H	05	0100	0.0–2.2	2.2	2.23	101.0
2H	05	0205	2.2–11.7	9.5	10.07	106.0
3H	05	0300	11.7–21.2	9.5	10.03	105.6
4H	05	0405	21.2–30.7	9.5	9.97	105.0
5H	05	0500	30.7–40.2	9.5	9.83	103.0
6H	05	0600	40.2–49.7	9.5	9.97	105.0
7H	05	0710	49.7–59.2	9.5	10.07	106.0
8H	05	0815	59.2–68.7	9.5	10.12	106.5
9H	05	0915	68.7–78.2	9.5	9.88	104.0
10H	05	1015	78.2–87.7	9.5	9.96	105.0
11H	05	1115	87.7–93.3	5.6	5.62	100.0
12X	05	1300	93.3–93.8	0.5	0.00	0.0
Coring totals				93.8	97.75	104.2
138-848C-1H	05	2125	0.0–5.5	5.5	5.47	99.4
2H	05	2230	5.5–15.0	9.5	9.95	105.0
3H	05	2330	15.0–24.5	9.5	10.06	105.9
4H	06	0025	24.5–34.0	9.5	10.07	106.0
5H	06	0130	34.0–43.5	9.5	9.40	98.9
6H	06	0235	43.5–53.0	9.5	10.03	105.6
7H	06	0335	53.0–62.5	9.5	10.06	105.9
8H	06	0445	62.5–72.0	9.5	9.81	103.0
9H	06	0615	72.0–81.5	9.5	10.00	105.2
10H	06	0715	81.5–91.0	9.5	9.87	104.0
11X	06	0905	91.0–94.2	3.2	3.02	94.4
Coring totals				94.2	97.74	103.8
138-848D-1H	06	1055	0.0–8.4	8.4	8.44	100.0
2H	06	1155	8.4–17.9	9.5	9.88	104.0
3H	06	1245	17.9–27.4	9.5	9.91	104.0
4H	06	1350	27.4–36.9	9.5	9.76	103.0
5H	06	1445	36.9–46.4	9.5	9.85	103.0
6H	06	1540	46.4–55.9	9.5	10.00	105.2
7H	06	1820	55.9–65.4	9.5	9.17	96.5
8H	06	2010	65.4–74.9	9.5	10.02	105.5
9H	06	2110	74.9–84.4	9.5	9.88	104.0
10H	06	2225	84.4–93.9	9.5	9.97	105.0
Coring totals				93.9	96.88	103.2

magnetic susceptibility, and color reflectance data, enabled us to use fine-scale correlation among holes (see "Sedimentation Rates" section, this chapter) and were used to develop a composite lithologic section for the entire site (Fig. 6).

The sediments at Site 848 are described as one unit because the entire sequence is dominated by nannofossil ooze, with only minor intervals of diatom nannofossil ooze, metalliferous nannofossil ooze, and metalliferous clay. Abundances of trace fossils vary considerably through the sequence. Burrowing appears to be minor for most of the cored interval, and is more obvious in the diatom- and radiolarian-rich interbeds, but this may be an artifact of the stronger color contrast within these beds. Color typically varies from white (N8) to very pale brown (10YR 8/3) to dark brown (10YR 3/6) and generally reflects the oxide content of these sediments. More subtle color variations occur that are related to variations of biogenic components.

Description of Units

Lithologic Unit I

Intervals:
Core 138-848A-1H,
Cores 138-848B-1H through -12X,
Cores 138-848C-1H through -11X,
Cores 138-848D-1H through -10H
Age: Pleistocene to Miocene
Depth: 0–9.4 mbsf, Hole 848A; 0–93.8 mbsf, Hole 848B; 0–94.2 mbsf, Hole 848C; 0–93.9 mbsf, Hole 848D

The sedimentary sequence at Site 848 is dominated by calcareous material, with carbonate percentages generally greater than 60% of the total sediment (see "Organic Geochemistry" section, this chapter). Slightly more siliceous nannofossil oozes, which form thin gradational layers interbedded throughout much of the section, are a minor lithology. In the lower portion of the sequence, metalliferous sediments that contain up to 50% reddish-brown, semi-opaque oxides become a significant sedimentary component.

The uppermost portion of the sequence (0–2.5 mbsf, Hole 848A; 2.2 mbsf, Hole 848B; 2.78 mbsf, Hole 848C; and 2.67 mbsf, Hole 848D) is a very pale brown (10YR 7/3) to light yellowish-brown (10YR 6/4) clayey nannofossil foraminifer ooze. A large, centric diatom species (*Azpeitia nodulifer*), generally associated with interglacial episodes (Burckle and McLaughlin, 1977), was found near the base of this interval in Section 138-848C-2H-1 at 10 to 25 cm. Below this clay-rich interval to about 75 mbsf, sediments are predominantly white (N9) to light greenish-gray (5Y 7/1) to very pale brown (10YR 8/3) foraminifer nannofossil ooze. The relative abundance of

Figure 3. Hand-contoured SeaBeam map from navigation-adjusted SeaBeam contour maps collected from the *Thomas Washington* during Venture 1 cruise, September 1989. Proposed Site WEQ-5 is shown.

foraminifers decreases from about 35% to less than 10% between 0 and 40 mbsf (Fig. 7). Foraminifers are a minor fraction of the sediments below about 40 mbsf, but increase to about 15% near the base of the section. Nannofossil content increases with depth from about 40% to 80% in the top 40 m of the section and remains consistently high throughout most of the lower section. The color changes from white (N9 to 5Y 7/1) to yellowish-brown (10YR 6/3 to 10YR 5/4) at 75.0 mbsf in Hole 848B (74.1 mbsf, Hole 848C; 75.8 mbsf, Hole 848D). This change may reflect an increase in the concentration of oxides below this level.

Siliceous microfossils are present in only minor amounts throughout the entire sequence, except for thin (15–30 cm) interbeds of diatom nannofossil ooze with radiolarians (containing up to 30% diatoms and increased radiolarian and clay percentages). These more siliceous layers have more burrows and are darker than the surrounding sediments (Fig. 8). Relative to the surrounding nannofossil ooze, these intervals are characterized by lower GRAPE bulk densities and higher magnetic susceptibilities (Fig. 9). An interval of prominent interbedding occurs from about 26.5 to 34.9 mbsf in Hole 848B, from 26.8 to 36.2 mbsf in Hole 848C, and from 27.7 to 37.0 in Hole 848D.

Near the bottom of the sequence, sediments are characterized by an increase in Fe-oxide content. Sediments from 82.6 to 91.6 mbsf in Hole 848B, from 83.2 to 89.2 in Hole 848C, and from 84.4 to 90.5 in Hole 848D consist primarily of dark yellowish-brown (10YR 4/4 to 10YR 3/6) metalliferous nannofossil ooze that contains 5% to 6% Fe-oxides and trace amounts of volcanic glass and clay. Fe-oxides compose 35 to 45 wt% of the carbonate and opal-free fractions. Only trace amounts of siliceous microfossils were found below about 83 mbsf. A distinctive lighter yellowish-brown (10YR 5/4) interval (83.85–84.03 mbsf in Hole 848B, 83.45–83.75 mbsf in Hole 848C, and 84.73–84.95 mbsf in Hole 848D) has extremely low carbonate contents (see "Organic Geochemistry" section, this chapter) and anomalously high water content, coincident with high grain density (see "Physical Properties" section, this chapter). Smear slides and physical properties measurements suggest that this interval consists

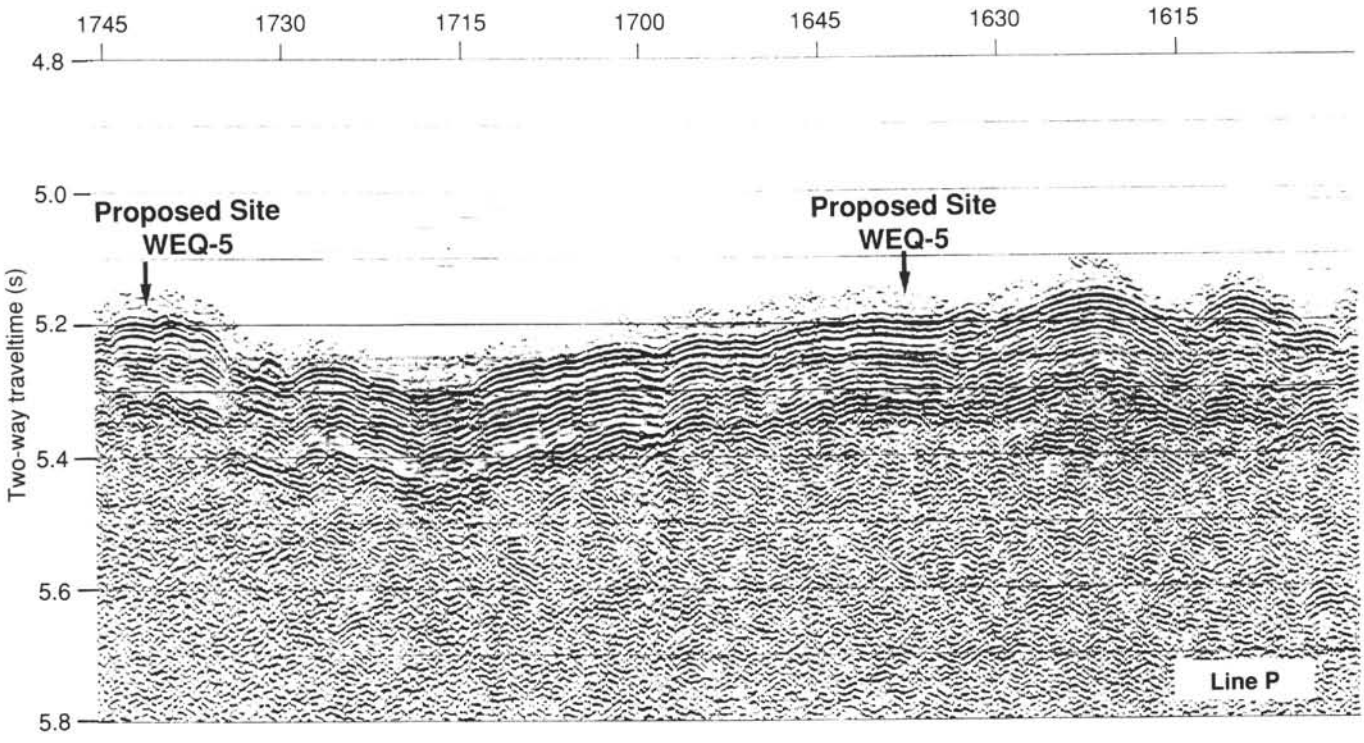

Figure 4. Seismic Line P. 80-in.^{3} water-gun record collected from *Thomas Washington* during the Venture 1 cruise. Proposed Site WEQ-5 is shown.

Table 2. Summary of logging operations at Site 848.

Date (June 1991)	Time (L)	Cumulative hours	Base of string (mbsf)	Remarks
5	0600	0.0		Last core on deck.
5	0730	1.5		Start rig up.
5	0820	2.3		RIH w/geochem. string (NGT/ACT/GST/TLT).
5	0930	3.5	0.0	Pause at mud line.
5	0935	3.6	94.5	At TD; heave comp. left off; calibrate while moving up slowly.
5	0943	3.7	73.8	GST calibrated; go back to TD.
5	0945	3.8	93.9	Start main log w/geochem. String from TD; no heave compensator.
5	1017	4.3	0.0	Stop main log; POOH.
5	1125	5.4		Geochem. string at wellhead.
5	1225	6.4		Rigged down from logging.

mainly of hydrous clays, with minor amounts of nannofossils. Mechanical difficulties with the shipboard X-ray diffractometer precluded a more specific mineralogical analysis.

The lowermost portion of the section (91.6–93.3 mbsf, Hole 848B; 92.9–94.2 mbsf, Hole 848C; and 90.5–93.9 mbsf, Hole 848D) is a very pale brown (10YR 7/3) foraminifer nannofossil ooze. The average oxide content of the carbonate and opal-free fractions remains relatively high (35%–45%) within this interval, suggesting that the lighter color may be related to dilution by the carbonate component.

Color Reflectance Spectroscopy

Color reflectance in Hole 848B is summarized in Figure 10. On the scale of the entire hole, the dominant color signal is the variation from relatively high reflectance (40%–100% in the visible bands) nannofossil and foraminifer oozes from about 0 to 75 mbsf to low reflectance (10%–60% in the visible bands) dark brown metalliferous nannofossil ooze in the interval from about 75 to 92 mbsf. On a large scale, intervals where the near-infrared (850–900 nm) and red (650–700 nm) bands are much more reflective than the blue (450–500 nm) band coincide with zones of high magnetic susceptibility and low sedimentation rates. This suggests that the major color signal on this scale at Site 848 is the mineralogy and concentration of oxides.

Surface sediments have been oxidized and have high reflectance in the near-infrared and red bands. In the interval from about 5 to 35 mbsf, the color reflectance signal records strong variance on a scale of decimeters to meters. The interval from 20 to 30 mbsf is illustrated in Figure 11. High reflectance values generally correspond to high GRAPE densities (indicating high percentages of $CaCO_3$) and low magnetic susceptibilities. This interval of highly calcareous sediments is most reflective in the visible bands having maximum reflectance near 550 nm and least reflective in the near-infrared bands. This pattern is similar to nannofossil ooze color spectra in other sites. Typical reflectance values for the palest bands are 50% to 70%.

Nannofossil ooze is interbedded with diatom nannofossil ooze, while diatom concentrations of up to 30% were observed in smear slides and slightly lower carbonate percentages prevail. These sediments are darker than the interbedded nannofossil ooze and yield an average reflectance of 30% to 40%. In spite of the lower average reflectance, the shape of the reflectance spectrum for this lithology (Fig. 10A) parallels that of the calcite-rich bands (not shown). The lithologic variation of calcium carbonate and opaline silica also has

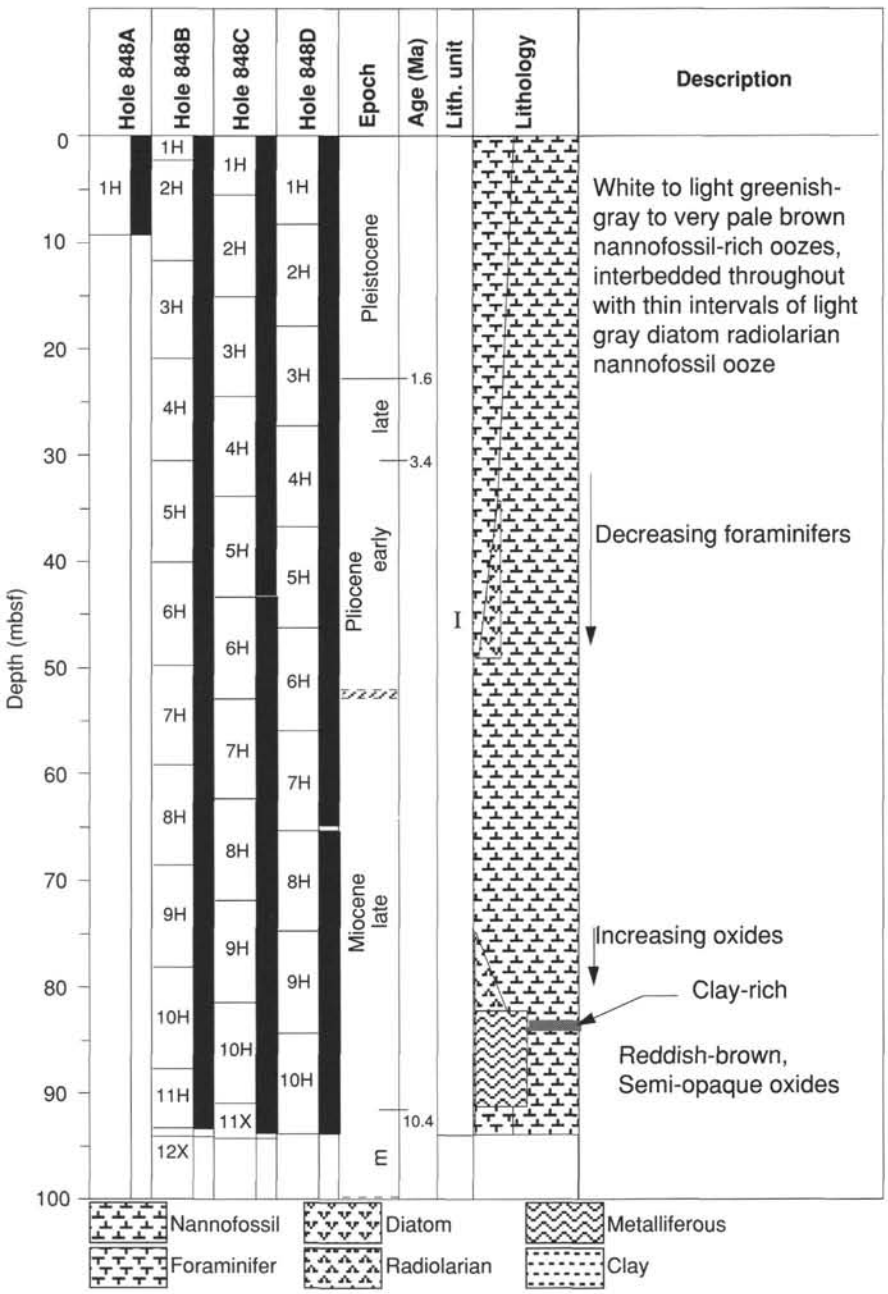

Figure 5. Lithologic summary for Site 848.

been superimposed with purplish-gray diagenetic banding. Where relatively intense, this banding reduces reflectance in some carbonate-rich intervals to values lower than those in the adjacent siliceous bands.

The interval from about 55 to 75 mbsf at Site 848 contains very pale brown to white (10YR 8/3 to N9) nannofossil ooze. Although the major lithology is similar to that observed in the upper interval of Site 848, the reflectance spectrum is different. The brown color may be related to the presence of oxides. Reflectance is highest in the near-infrared bands. An unusual zone of relatively constant reflectance occurs from about 550 to 650 nm (Fig. 10B).

The interval of white nannofossil ooze is highly reflective in all bands and, in some cases, exceeds 100% reflection. These samples may have been influenced by specular reflection (a "mirror effect"), because they were wet and smooth when measured. In spite of this problem in a few samples, the small variations in reflectance near (but below) 100% were verified by careful visual observation of subtle changes in color, from stark white (N9) to very pale brown (10YR 8/3), and were correlatable among holes. Although these sediments are dominated by calcium carbonate, the shape of the color spectra, with highest reflectance in the near infrared bands, again suggests the presence of oxides. This contrasts with color spectra from nannofossil oozes in other intervals of this site and at Sites 844 through 847, in which purplish-gray sulfides contributed to lower reflectance in near-infrared rather than in the visible bands.

Below about 75 mbsf, the sediment changes to darker brown colors (10YR 6/4 to 10YR 3/6). The reflectance spectrum of the darkest sample (from Section 138-848B-10H-5 at 130 cm, 85.50 mbsf) is illustrated in Figure 10D. This sample contains nannofossil ooze but is relatively rich in oxide minerals, probably related to hydrothermal influx. Below about 75 mbsf, the sedimentation rate is

low, which might also enhance oxidizing conditions within the sediment. Reflectance patterns in this interval are similar to, but darker than, oxidized material near the sediment/water interface.

In Site 848, color reflectance patterns of both oxidized and reduced sediments were demonstrated. On a larger scale (tens of meters), the accumulation of more oxidized (redder) sediments can be associated with low sedimentation rates and higher magnetic susceptibilities, and may also have been influenced by influxes from hydrothermal and terrigenous sources. On a finer scale (decimeters to meters), color reflectance in these sediments demonstrates extensive interbedding related to alternations of silica content within highly calcareous sediments. Diagenetic alteration also may have had important effects for color spectra measured on finer scales.

Trace Fossils

Considerable variety exists in the extent of apparent bioturbation at Site 848. However, this apparent intensity of burrowing depends on the color contrast within the sediment. Strong burrowing usually is seen where beds of strongly contrasting color are present (Figs. 8 and 12). Elsewhere, similar burrows may be present, even though they were not observed easily.

In the foraminifer nannofossil ooze (0–40 mbsf), variable light to strong bioturbation was observed. Burrows are most evident in the diatom- or radiolarian-rich interbeds. *Planolites* and solid burrows are abundant, and vertical *Skolithos* burrows are common (Figs. 12 and 13). *Zoophycos* is less common and was observed mainly in the darker, more diatom-rich interbeds between 15 and 20 mbsf.

Little or no burrowing was seen in the nannofossil ooze between 40 and 72 mbsf. Substantial bioturbation appears within the radiolarian nannofossil ooze and metalliferous sediments from 72 to 91 mbsf (Figs. 12, 14, and 15). Solid burrows and *Planolites* are common and rind burrows are abundant in the brown radiolarian nannofossil ooze between 77 and 90 mbsf (Fig. 14). *Zoophycos* and *Skolithos* are scattered within beds of diatom radiolarian nannofossil ooze between 71 and 77 mbsf. *Chondrites* was observed only once, in Section 138-848B-10H-4.

Summary of Lithology

Sediments recovered from Site 848 are predominantly nannofossil ooze interbedded with siliceous nannofossil ooze. At the base of the sequence, nearly 10 m of dark brown oxide-rich nannofossil ooze is present. First-order color variations may be related to oxide content. This finding is suggested by reflectance data, which clearly distinguish intervals containing metalliferous oxides (Figs. 6 and 10). Lower sedimentation rates (see "Sedimentation Rates" section, this chapter) may be partly responsible for the high concentration of oxides in this interval; however, the presence of reddish-brown, semi-opaque oxides within this basal interval suggests a hydrothermal origin for these sediments.

Sediments from the upper portion of this unit contain only trace oxides and generally are much lighter colored than sediments from the lower section. Percentages of carbonates are high throughout most of the sequence. A slightly darker, more siliceous component is interbedded throughout. GRAPE bulk density measurements provide a first-order estimate of carbonate content (lower GRAPE density = lower $\%CaCO_3$ and clearly distinguish the siliceous nannofossil ooze layers from the dominant nannofossil foraminifer ooze. A slight increase in clay content within these interbeds also is apparent from the magnetic susceptibility record (Fig. 9). Although detailed microfossil and time series analyses will be needed to evaluate these variations better, these data do suggest that carbonate dissolution may be responsible for concentrating noncarbonate components.

BIOSTRATIGRAPHY

A continuous sedimentary record for the upper Pleistocene through the uppermost middle Miocene was recovered from the four holes cored at Site 848. A well-constrained stratigraphy for this sequence has been provided by calcareous nannofossils, radiolarians, and diatoms (Fig. 16). The following paragraphs describe biostratigraphic results from Holes 848B, 848C, and 848D because only one core was recovered from Hole 848A.

Abundance and preservation of the microfossil groups vary throughout the section. Planktonic foraminifers are abundant and moderately well preserved in the uppermost interval of Site 848 (Cores 138-848B-1H and -2H) and are rare or absent in the interval below (Cores 138-848B-3H through -11H). Calcareous nannofossils are abundant throughout the section and provide a good stratigraphy for the entire sequence. Radiolarians and diatoms show generally good preservation within the Pleistocene–Pliocene and upper Miocene sections; preservation rapidly declines near the bottom of the recovered section (Cores 138-848B-9H and -10H). The lowermost core (138-848B-11H) is barren of siliceous microfossils.

A good magnetic stratigraphy was obtained in the Pleistocene–Pliocene and lower upper Miocene sections at this site. This stratigraphy provided us the means to calibrate selected nannofossil, radiolarian, and diatom datums and provided new biochronological data that could be compared with other data sets from low- and mid-latitude ocean basins.

The microfossil events recognized at Site 848 are reported in Tables 3 through 5, together with intervals of occurrence and subbottom depths.

In Figure 16, epoch boundaries have been placed as follows:

Boundary	Hole	Depth (mbsf)	Depth (mcd)	Event
Pleistocene/Pliocene	848C	23.20	26.20	top Olduvai
late/early Pliocene	848D	34.10	36.70	Gauss/Gilbert
Pliocene/Miocene	848D	53.15	38.15	B. *Discoaster quinqueramus*
late/middle Miocene	848B	90.45	102.80	CN5 chron (o)

(o) = onset.

Calcareous Nannofossils

Calcareous nannofossils recovered at Site 848 represent a stratigraphic succession from the upper Pleistocene (Zones CN14b from Okada and Bukry, 1980, and NN20 from Martini, 1971) through the uppermost middle Miocene (Zones CN6 and NN8). Nannofossils are common to abundant throughout the section. Owing to the relatively low sedimentation rate at Site 848, the identification of biostratigraphic events (Table 3) was based on closely spaced samples (10–60 cm).

Calcareous nannofossils generally are well preserved in the Pleistocene interval (Sections 138-848B-1H-CC through -3H-CC, 138-848C-1H-CC through -3H-5, and 138-848D-1H-CC through -3H-4). The assemblage is characterized by *Pseudoemiliania lacunosa, Calcidiscus* spp., different morphotypes of *Gephyrocapsa* spp., helicoliths, and ceratolithids. The first occurrence of *Gephyrocapsa oceanica* s.l., which approximates the Pleistocene/Pliocene boundary, was placed between Samples 138-848B-3H-6, 80 cm, and -3H-7, 17 cm, and Samples 138-848C-3H-5, 40 cm, and -3H-5, 50 cm (Table 3).

The Pliocene nannofossil assemblage is characterized by different morphotypes of *Reticulofenestra* spp., discoasterids, helicoliths, ceratoliths, and sphenoliths in the lower Pliocene interval. Preservation of calcareous nannofossils is generally good in this interval, and only slight etching of some placoliths and overgrowth of ceratolithids were observed. The discoasterids are common throughout the interval, and

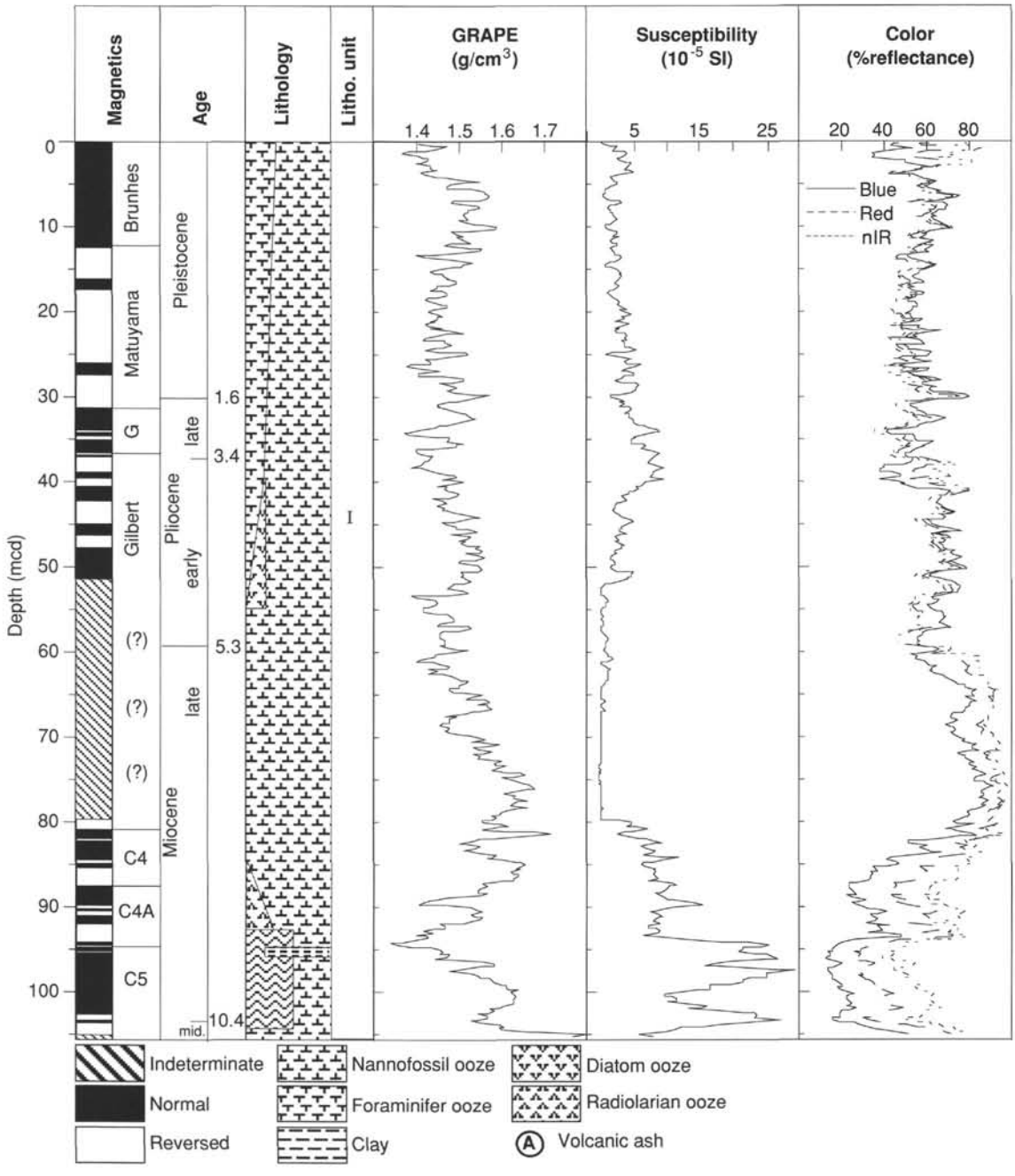

Figure 6. Composite summary of magnetics, age, graphic lithology, GRAPE magnetic susceptibility, and color reflectance for Site 848. These composite data consist of sections spliced together from the multiple holes drilled at the site. Data are shown plotted vs. meters composite depth (mcd), the new depth scale used when composite sections were constructed. GRAPE, susceptibility, and color reflectance data have been smoothed using a 20-point Gaussian filter.

most of the discoasterid events, useful for biostratigraphic division of the upper Pliocene, were recognized (Table 3).

The last occurrence of *Reticulofenestra pseudoumbilicus* (base of Zones CN12a and NN16), which approximates the upper/lower Pliocene boundary, was recorded between Samples 138-848B-5H-1, 95 cm, and -5H-2, 50 cm.

In the lower Pliocene interval (Cores 138-848B-5H and -6H),ceratolithid species *Amaurolithus primus, Amaurolithus delicatus, Amaurolithus tricorniculatus, Ceratolithus acutus, Ceratolithus armatus,* and *Ceratolithus rugosus* are common and were found throughout the interval. Intergrading morphotypes between the various species of common ceratolithids were observed. The unusually consistent occurrence of ceratolithids at Site 848 allowed us to define the complete lower Pliocene sequence of events within this group (Table 3).

In the upper Miocene and in the upper middle Miocene (Cores 138-848B-7H through -11H, -848C-6H through -11H, and -848D-6H through -10H), the nannofossil assemblage is characterized by *Reticulofenestra* spp., *Coccolithus* spp., *Calcidiscus* spp., discoasterids, ceratolithids, helicoliths, and sphenoliths. Preservation is moderate to good throughout the interval; however, a marked decline in the preservation of the nannofossil assemblage occurs in Cores 138-848B-8H through -11H, with the discoasterids showing increasingly strong overgrowth. The as-

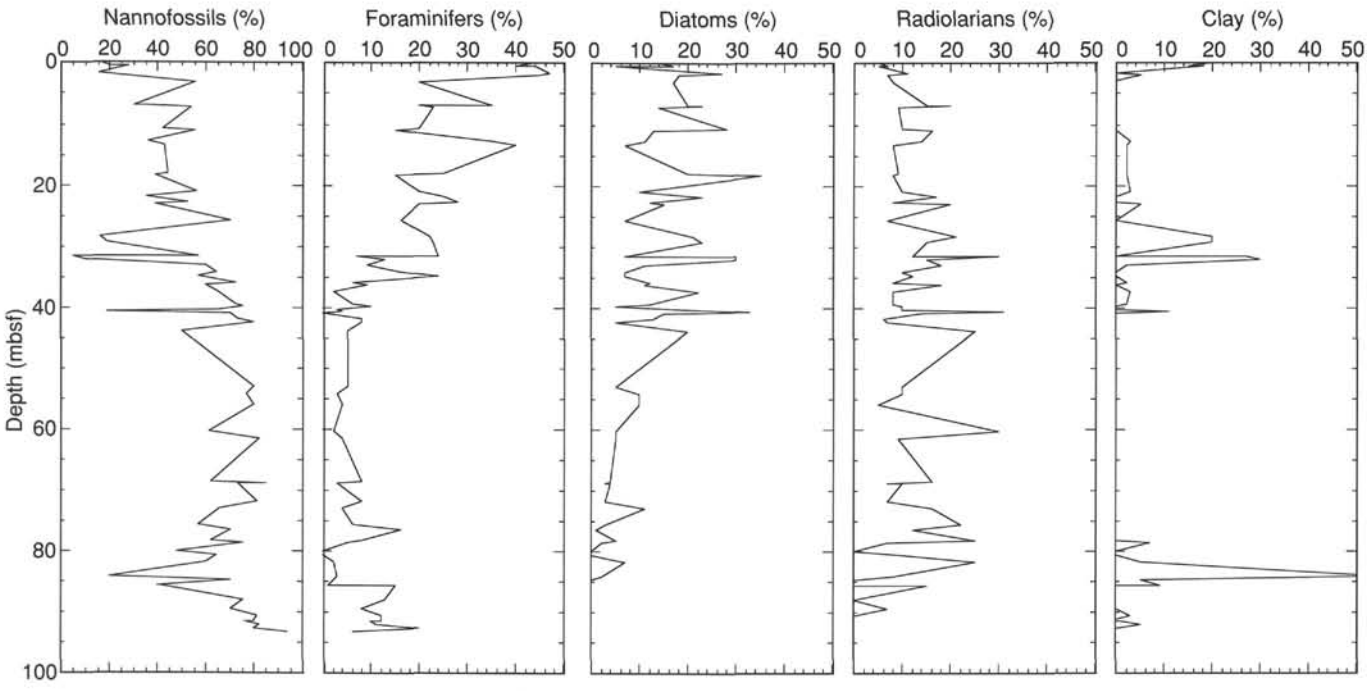

Figure 7. Summary of major-component smear slide data from Site 848. Note the different scale for calcareous nannofossils.

semblage in the lower portion of Cores 138-848B-9H through -11H, shows sign of dissolution, with etching of most of the placolith species and an increase in abundance of strongly overgrown discoasterids.

The last occurrence of *Discoaster quinqueramus* (top of Zones CN9b and NN11), which approximates the Pliocene/Miocene boundary, occurs in Samples 138-848B-7H-1, 95 cm, -848C-6H-CC, and -848D-6H-5, 100 cm. Below this event, in the interval corresponding to Zone CN9b/NN11, we found abundant specimens of *Amaurolithus primus* and *A. delicatus*. The Subzone CN9a/Zone CN8 (Zone NN11/Zone NN10) boundary, which corresponds to the first occurrence of *Discoaster berggreni,* was placed between Samples 138-848B-9H-3, 100 cm, and -9H-4, 40 cm. This marker species is very rare in the lower part of its stratigraphic range, suggesting only tentative placement of this event. This species, as well as the other discoasterids, shows particularly low abundances in the interval between 65 and 75 mbsf (Sections 138-848B-8H-6 through -9H-3).

The total range of *Discoaster hamatus,* which encompasses Zone CN7 (NN9), ranges from Sample 138-848B-10H-4, 40 cm, through -848B-11H-1, 90 cm. Just above the first occurrence of this species, the last occurrence of *Coccolithus miopelagicus* was recorded between Samples 848B-10H-CC and -11H-1, 20 cm. Precise biostratigraphic assignment of the lowermost part of the sedimentary sequence (Core 848-11H-2 through -11H-CC) is difficult owing to the poor preservation of discoasterids and to the absence of the biozonal marker *Catinaster coalitus*. The assemblage observed, however, places some constraints on the age of the oldest part of the sequence. The presence of *C. miopelagicus,* the absence of five-rayed discoasterids belonging to the *Discoaster hamatus–Discoaster bellus* Group, and *Reticulofenestra pseudoumbilicus,* and the absence of specimens of six-rayed discoasterids with a broad central area (*Discoaster kugleri–Discoaster musicus* Group, characteristic of the middle Miocene interval) suggest that the basal part of the sequence is equivalent to the uppermost middle Miocene Zone CN6 (NN8).

Planktonic Foraminifers

Planktonic foraminifers are abundant, and preservation is moderate to poor in Cores 138-848B-1H and -2H. Throughout the remainder of the sedimentary sequence, preservation is poor and assemblages often exhibit a high degree of fragmentation. Planktonic foraminifers are rare in Core 138-848B-3H, few to common in Cores 138-848B-4H through -6H, rare in Cores 138-848B-7H through -9H, virtually absent in Core 138-848B-10H (in which only a few specimens were found), and abundant in Sample 138-848B-11H-CC.

Throughout the entire sequence, radiolarians dominate the coarse fraction residues. Other major coarse-fraction components present throughout most of the sequence are rare-to-few echinoid spines and sponge spicules. Fish teeth are scattered. Manganese micronodules are common in Sections 138-848B-8H-CC and -10H-5 at 150 cm. Volcanic glass is rare in Cores 138-848B-8H and -9H, but common in Sample 138-848B-11H-CC.

We tentatively established a zonation on the basis of the same marker species as at other eastern equatorial Pacific Ocean sites. The base of Zone N22 was equated to the last occurrence of *Globorotalia limbata* in Sample 138-848B-4H-CC, and the base of Zone N21 was defined by the last occurrence of *Sphaeroidinellopsis* spp. in Sample 138-848B-5H-CC. However, from a comparison to biostratigraphic assignments from other microfossil data (Fig. 16), one may hypothesize that dissolution significantly curtails the range of these species and that the base of these two zones is here stratigraphically too low. Core 138-846B-6H was assigned to the Pliocene interval N19-N18, based on the presence of *Globorotalia tumida*. The interval from Cores 138-848B-7H through -10H has been left unzoned because it yielded dissolved, nondiagnostic assemblages that included rare *Globoquadrina venezuelana, Dentoglobigerina altispira,* and *Sphaeroidinellopsis* spp. Sample 138-848B-11-CC contains abundant, poorly preserved planktonic foraminifers, together with common volcanic glass. The originally dissolved assemblage may have been partly recrystallized; it is dominated by *Globorotalia siakensis,* indicating an age older than the top of Zone N14. Other species include few *Globoquadrina venezuelana, Globoquadrina dehiscens, Sphaeroidinellopsis* spp., *Orbulina universa, Globigerinoides sacculifer, Globigerinoides obliquus,* and rare globorotaliids attributable to *Globorotalia praemenardii.* The latter species is generally reported as stratigraphically ranging from Zones N10 through N12.

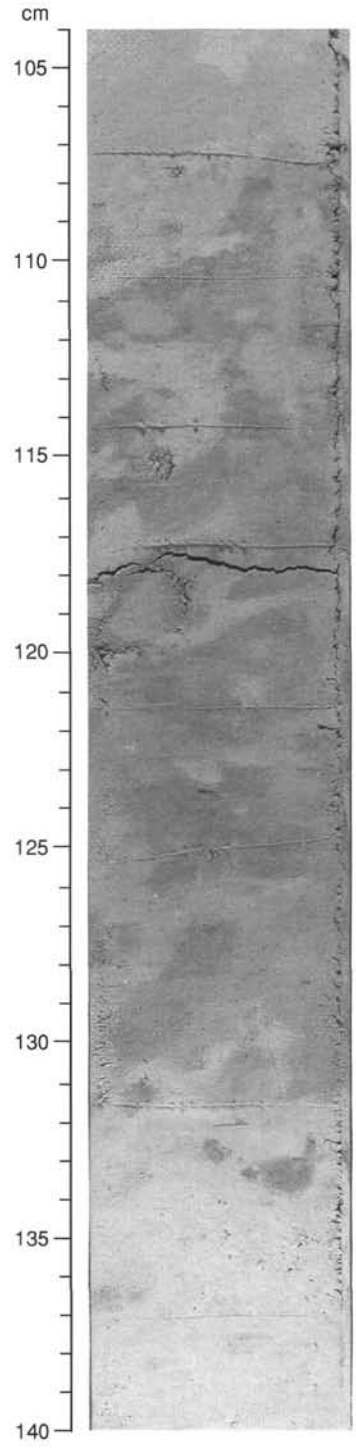

Figure 8. A darker bed of more radiolarian- and diatom-rich nannofossil ooze reveals strong bioturbation, including solid burrows, *Planolites,* and *Skolithos* in Section 138-848D-4H-3 at 104–140 cm.

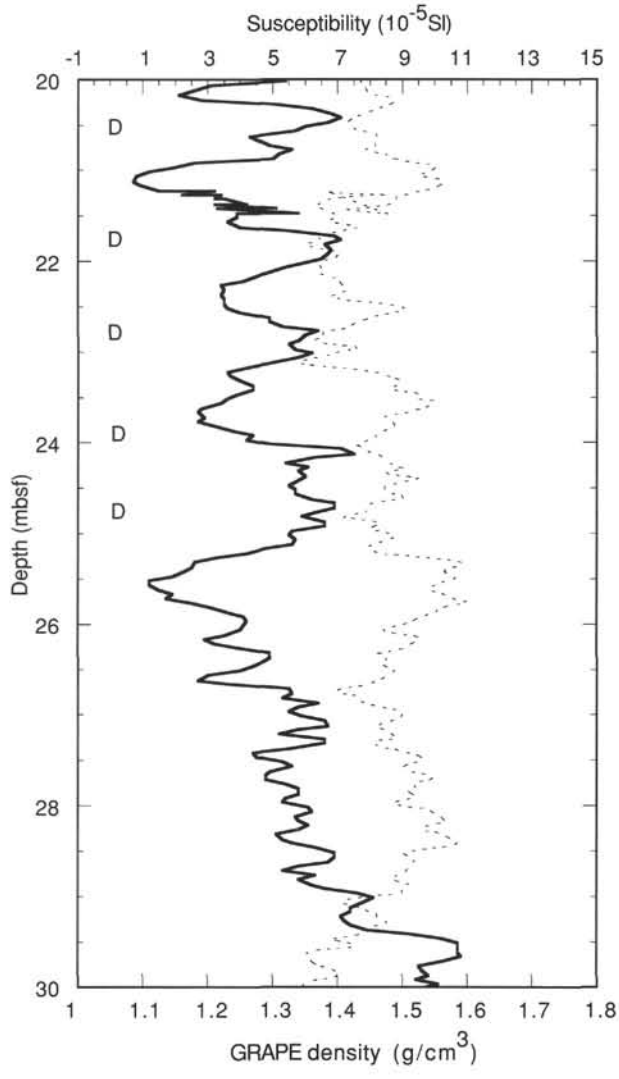

Figure 9. GRAPE bulk density (dashed line) and magnetic susceptibility (solid line) data from Hole 848B (20–30 mbsf) showing cyclic interbedding of

Radiolarians

Radiolarians sampled at Site 848 range in age from the Quaternary (*Collosphaera tuberosa* Zone) to the late Miocene (*Diartus pettersoni* Zone). The most recent radiolarian zone (*Buccinosphaera invaginata*) was not identified. The oldest material recovered, which could be identified to the zonal level (*D. pettersoni* Zone), is from Sample 138-848B-10H-4 (150 cm). Below this level, all samples were barren of siliceous microfossils.

Preservation and abundances of radiolarians was generally good within the Pleistocene–Pliocene section. No clear indication of reworking of older radiolarians into the younger part of the section was observed. The Pleistocene–Pliocene section is fairly complete, and nearly all radiolarian zones and datums were identified (Table 4). Because of the relatively low accumulation rate at this site, the zones are compressed. Both the *Pterocanium prismatium* and *Anthocyrtidium jenghisi* zones were represented by single samples in Hole 849B, and the *Phormostichoartus fistula* Zone was not distinguished in the detailed sampling conducted in Core 138-848C-4H (Table 4). As at Site 846, specimens of *P. fistula* are very rare, and we considered their last detected occurrence to be an unreliable datum in this section. A few specimens of *Spongaster pentas, Spongaster berminghami,* and *Acrobotrys tritubus* were found; however, their occurrences are scattered and we do not consider their first and last appearances to be reliable datums.

Radiolarians were common to abundant throughout the upper Miocene part of the section, and preservation was good, except near the bottom of the recovered section (some individual samples within Cores

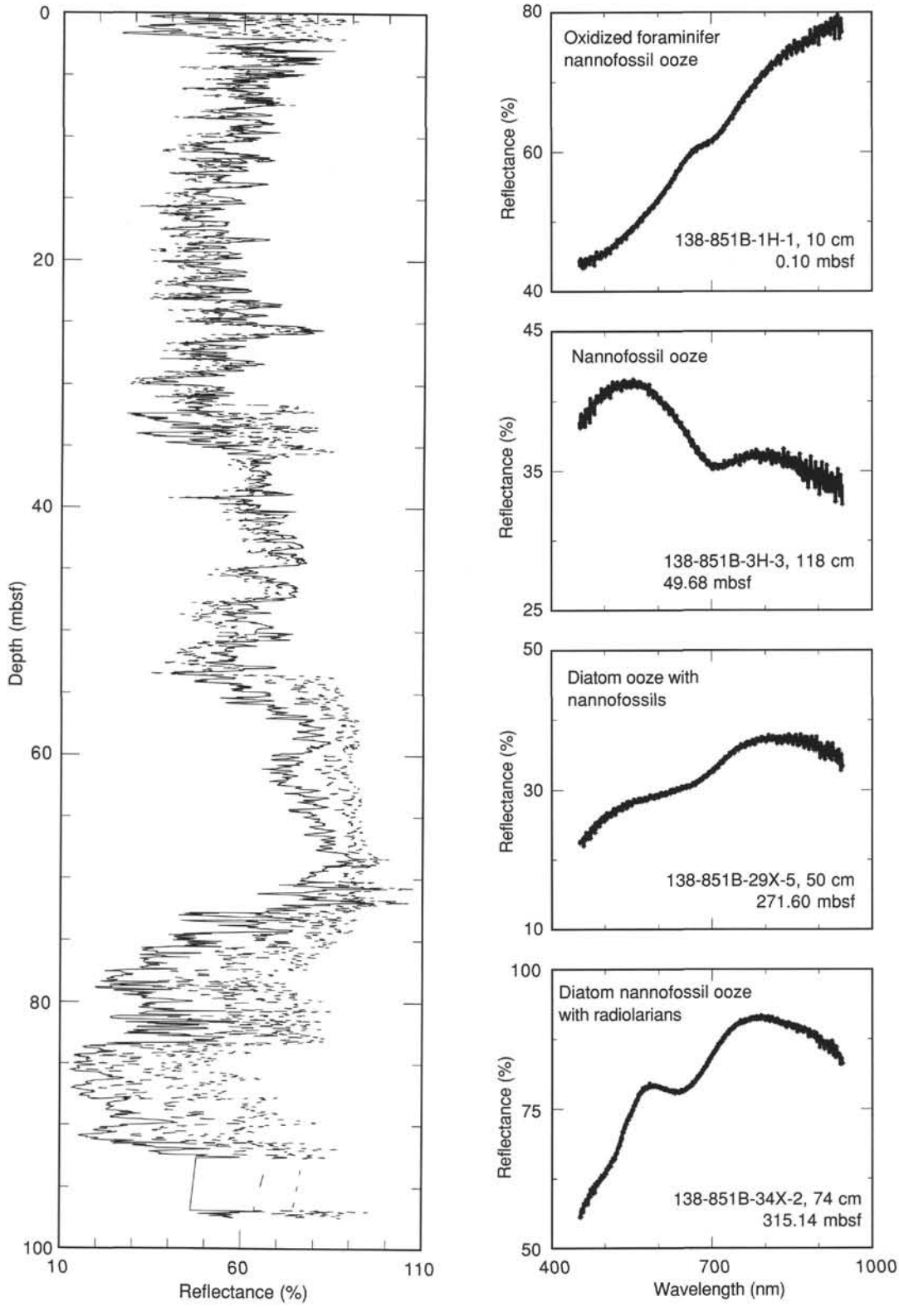

Figure 10. Color reflectance data for Hole 848B (left; solid line = blue, 450–500 nm; dashed line = red, 650–700 nm; dotted line = near-infrared, 850–900 nm) and examples of color spectra for specific lithologies within the core (right).

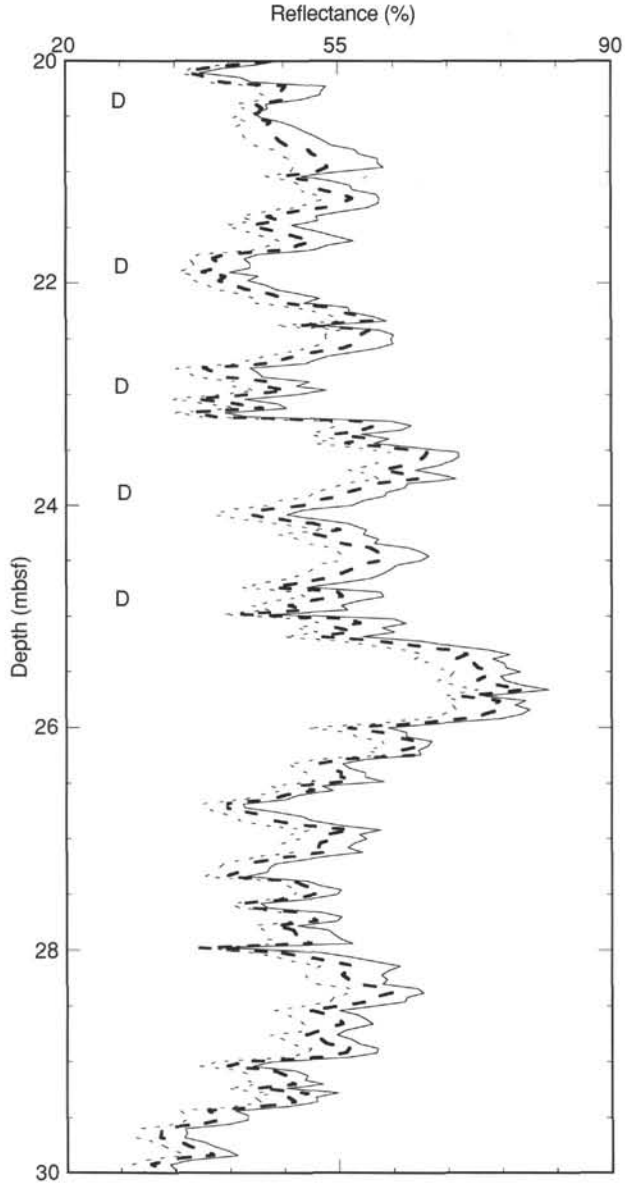

Figure 11. Color reflectance data from 20 to 30 mbsf in Hole 848B (solid line = blue, 450–500 nm; dashed line = red, 650–700 nm; dotted line = near-infrared, 850–900 nm). Intervals of higher reflectance correspond to higher GRAPE density (higher $\%CaCO_3$) values shown in Figure 9. "D" marks location of darker interbeds.

138-848B-9H and -10H and all of Core 138-848B-11H). The stratigraphically deepest reliable datum (Table 4) was the evolutionary transition between *Diartus pettersoni* and *Diartus hughesi* (between Samples 138-848B-9H-CC and -10H-1 at 150 cm). The middle part of Core 138-848B-10H may contain the latter part of the transition between *Lithopera neotera* and *Lithopera bacca.* Good specimens of both *L. neotera* and *L. bacca* were found down to the lowermost reasonably well-preserved sample (138-848B-10H-3, 110–111 cm). In Sample 138-848H-10H-4, 150 cm, preservation was poor to moderate, and no specimens of *L. bacca* or *L. neotera* were found.

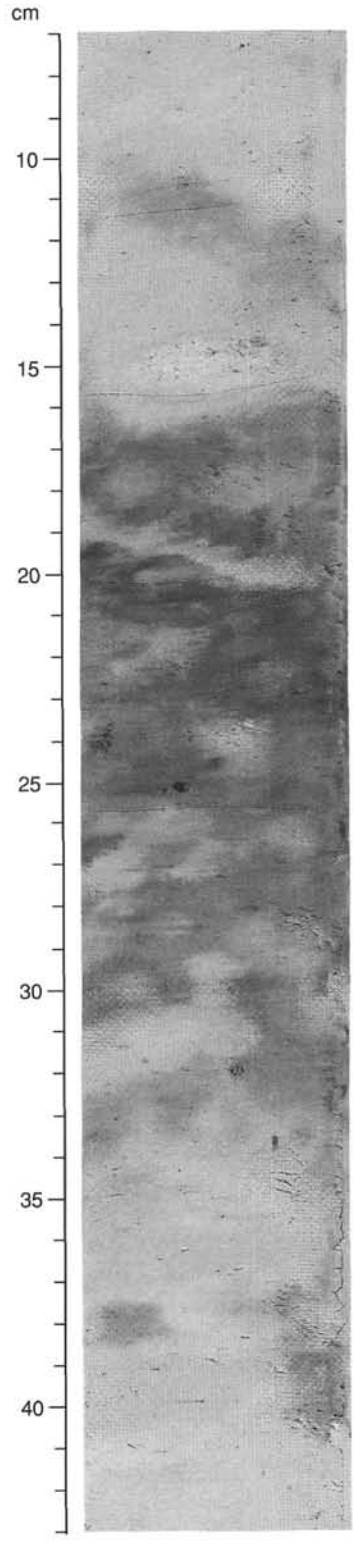

Figure 12. A typical darker bed of diatom radiolarian nannofossil ooze, within nannofossil ooze in Section 138-848B-9H-4 at 7–43 cm.

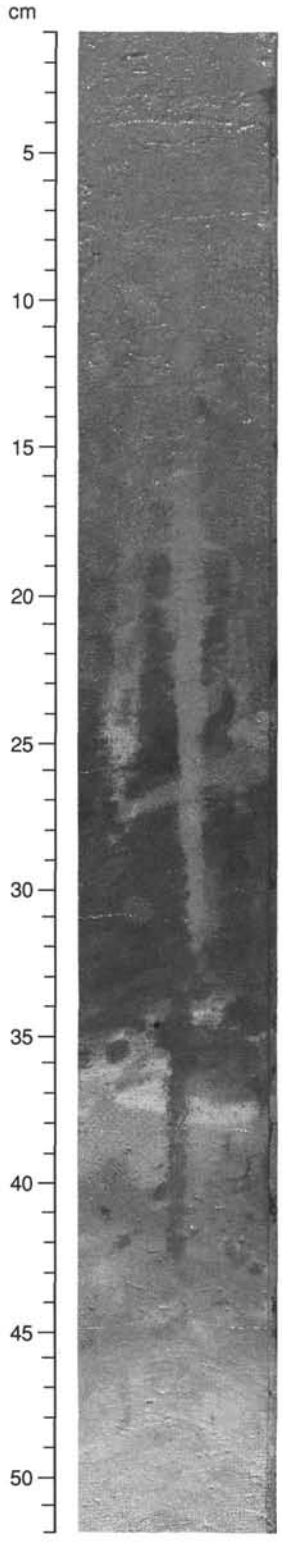

Figure 13. Surface 0.5 m at Site 848, showing a dark bed of foraminifer ooze cut by vertical *Skolithos* burrows in Section 138-848A-1H-1 at 1–52 cm.

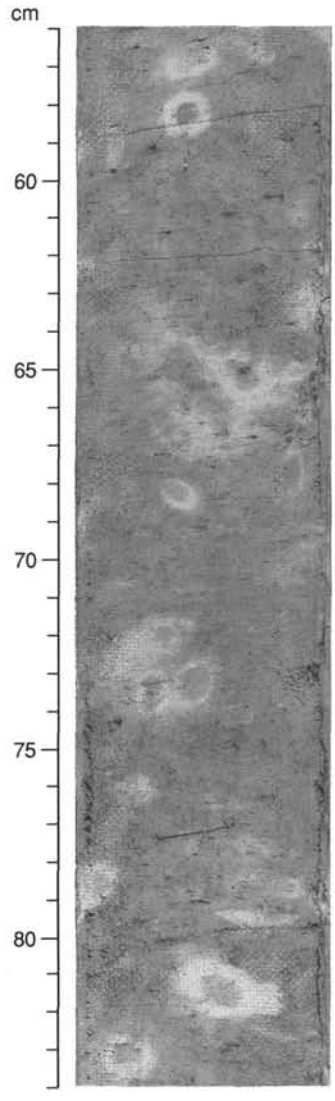

Figure 14. Common rind burrows within brown radiolarian nannofossil ooze in Section 138-848B-9H-5 at 56–84 cm.

Diatoms

Diatoms generally are common to abundant in the Quaternary (*Pseudoeunotia doliolus* Zone) through upper Miocene *(Nitzschia porteri* Zone) sequence recovered from Holes 848A through 848D. The exception is the interval from Samples 138-848B-11H-4, 34–35 cm, through -11H-CC, which does not contain diatoms. Preservation of diatoms varies from sample to sample, ranging from poor to good. The interval from Samples 138-846B-9H through -10H is characterized by poor-to-moderate preservation as a result of an increase in both dissolution and fragmentation of the frustules.

The diatom flora is characterized as *Actinocyclus ellipticus, Azpeitia nodulifer, A. africana, Ethmodiscus rex, Hemidiscus cuneiformis, Nitzschia fossilis, Nitzschia jouseae, Nitzschia marina, Nitzschia reinholdii, Pseudoeunotia doliolus, Rhizosolenia bergonii, Rhizosolenia*

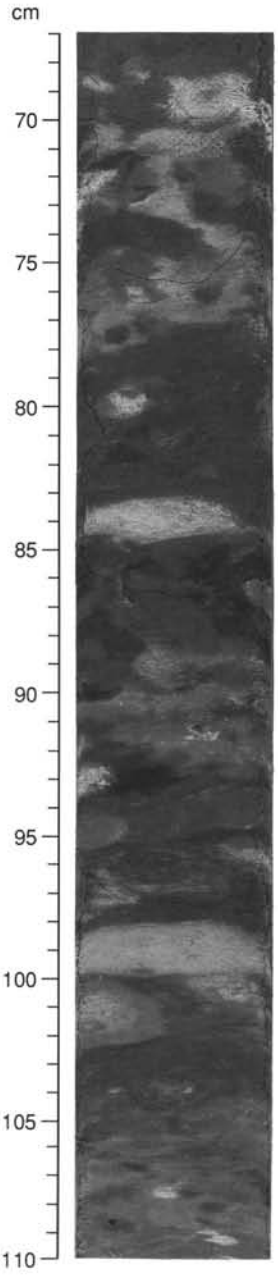

Figure 15. Strong bioturbation in dark brown, oxide-rich radiolarian nannofossil ooze in Section 138-848B-10H-4 at 67–110 cm.

praebergonii, Roperia tessellata, Thalassionema nitzschioides, Thalassionema nitzschioides var. *parva, Thalassiosira convexa, Thalassiosira oestrupii, Thalassiosira eccentrica,* and *Thalassiothrix longissima.*

Stratigraphic constraint of zonal assignments was based on examination of two to three smear slides per core (9.5 m) and several acid-processed slides per section (1.5 m). Cores 138-848B-1H and -848D-1H were assigned to the *P. doliolus* Zone on the basis of the occurrence of *P. doliolus* without *N. reinholdii.* Samples 138-848A-1H-CC, -848B-2H-CC through -3H-6, 120–121 cm, -848C-1H-CC through -2H-CC, and -848D-2H-CC were assigned to Subzone B of the *N. reinholdii* Zone. This zonal assignment was based on the co-occurrence of *P. doliolus, N. reinholdii,* and *N. fossilis* stratigraphically above the last occurrence of *R. praebergonii.* The last occurrence of *R. praebergonii* was placed between Samples 138-848B-3H-6, 120–121 cm, and -3H-CC, and Samples 138-848C-2H-CC and -3H-CC, which allowed us to assign these samples to Subzone A of the *N. reinholdii* Zone.

Samples 138-848B-4H-2, 120–121 cm, through -4H-6, 120–121 cm, -848C-4H-1, 40 cm, through -4H-4, 40 cm, and -848D-4H-7, 40 cm, were assigned to the *R. praebergonii* Zone. Samples 138-848B-4H-2, 120–121 cm, -4H-3, 120–121 cm, and -848C-4H-1, 40 cm, are equivalent to Subzone C, based on the occurrence of *R. praebergonii* stratigraphically below the first occurrence of *P. doliolus* and stratigraphically above the last occurrence of *T. convexa* var. *convexa,* Samples 138-848B-4H-4, 120–121 cm, and -848C-4H-2, 40 cm, were assigned to Subzone B of this zone, based on the co-occurrence of *T. convexa* var. *convexa* and *R. praebergonii* without *N. jouseae.* Samples 138-848B-4H-5, 120–121 cm, and -4H-6, 120–121 cm, and -848C-4H-4, 40 cm, were assigned to Subzone A on the basis of the co-occurrence of *N. jouseae, T. convexa* var. *convexa* and *R. praebergonii.*

Samples 138-848B-4H-7, 9–10 cm, through -6H-2, 120–121 cm, -848C-4H-CC through -5H-CC, and -848D-4H-CC were assigned to the *N. jouseae* Zone, based on the occurrence of this species stratigraphically below the first occurrence of *R. praebergonii.*

Samples 138-848B-6H-4, 120–121 cm, through -8H-3, 120–121 cm, -848C-6H-CC and -7H-CC, and Sample 138-848D-4H-CC were placed in the *T. convexa* Zone. This interval was subdivided into three subzones: Samples 138-848B-6H-4, 120–121 cm, and -6H-CC were assigned to Subzone C; Sample 138-848B-7H-2, 120–121 cm, was assigned to Subzone B; Samples 138-848B-7H-CC through -8H-3, 120–121 cm, and -848D-7H-CC were assigned to Subzone A.

Samples 138-848B-8H4, 70 cm through -9H-2, 36–37 cm, and -848D-8H-CC were placed in the *N. miocenica* Zone, based on the occurrence of *N. miocenica* without *T. convexa* var. *aspinosa.* The first occurrence of *N. miocenica* was placed in Sample 138-848B-9H-2, 36–37 cm, which indicates that Samples 138-848B-9H-2, 95–96 cm, and -9H-3, 119–120 cm are equivalent to the *N. porteri* Zone. Preservation of diatoms is poor to moderate in the interval equivalent to, and stratigraphically below, the *N. porteri* Zone (Cores 138-848B-10H through -11H, -848C-8H through -9H, and -848D-10H). We did not observe diatoms in Sample 138-848B-11H-CC.

PALEOMAGNETISM

Laboratory Procedures

Studies of paleomagnetism at Site 848 followed the experimental procedures outlined in the "Explanatory Notes" chapter (this volume). Early in the measurement sequence (Hole 848B), we experimented with several peak alternating fields (5, 8, 10, and 15 mT) to select a blanket peak alternating field (AF) for subsequent demagnetizations. We chose to apply AF treatment at 15 mT, because it more thoroughly removed the secondary overprints. Thus, all sections from every core at Site 848 were demagnetized in a 15-mT peak AF in the pass-through cryogenic magnetometer. For Hole 848B, we also measured the natural remanent magnetization (NRM) of each section from all 11 APC cores; for Holes 848C (10 APC cores) and 848A (1 APC core), we measured NRM of at least two sections from each core (usually Sections 2 and 5). No NRM was measured for Hole 848D (11 APC cores). The magnetostratigraphy was determined from the 15-mT demagnetized remanence.

Only seven discrete samples were processed for Site 848. In the upper 47 m, magnetostratigraphy was unambiguous; therefore, few discrete samples were needed to verify the results from the pass-through magnetometer. Below 47 mbsf, the weak magnetization intensity precluded our measuring the demagnetized remanence with the shipboard spinner magnetometer.

As at other Leg 138 sites, magnetic susceptibilities at Site 848 were used successfully for high-resolution, between-hole correlations to establish the site's composite depth scale (see "Sedimentation Rates" section, this chapter). Thus, susceptibilities were measured for all Site 848 sediments at 5-cm intervals.

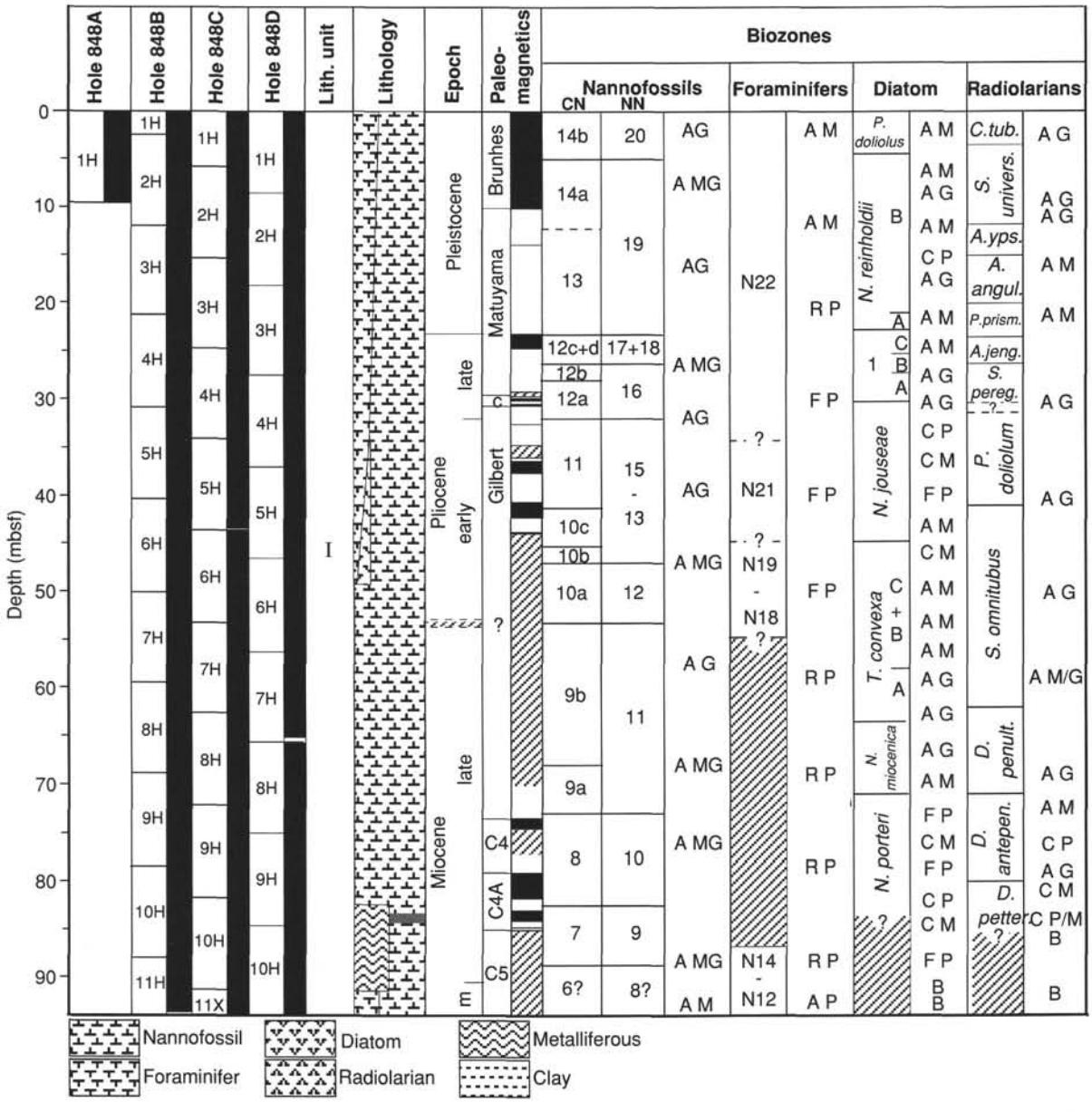

Figure 16. Stratigraphic summary for Site 848. Depth is in meters below seafloor (mbsf). Diatom zones: 1 = *Rhizosoleuis*(?) *Praedoysonii*(?). Microfossil abundances are recorded as A = abundant; C = common; F = few; R = rare; B = barren. Microfossil preservation is recorded as G = good; M = moderate; P = poor. The letter "r" indicates the presence of older, reworked microfossils. This figure is a general overview of the stratigraphic results at Site 848. Placement of specific stratigraphic boundaries may differ slightly among Holes 848A, 848B, and 848D. Data presented here are based on results from Holes 848A, 848B, and 848D.

Results

Depth profiles of magnetization intensity and susceptibility at Site 848 (Fig. 17) show that the section consists of three distinct zones. From 0 to 47 mbsf and below 72 mbsf, susceptibility and remanence intensity (after 15 mT AF demagnetization) are higher than in the intermediate zone between 47 and 72 mbsf. In this intermediate zone, remanence intensity (after 15 mT demagnetization) is typically 0.1 mA/m, on the order of the signal of an empty plastic liner; thus, no magnetic polarity stratigraphy could be recovered over this 25-m interval.

As at previous Leg 138 sites, the NRM at Site 848 is dominated by a steep upward (negative inclination) overprint, which we think may have been produced during coring. All seven discrete samples that were measured exhibited a steep negative inclination component that seemed to have been removed with 5 mT AF demagnetization. One reverse polarity sample (Fig. 18, bottom) shows removal of a second overprint between 5 and 20 mT, essentially parallel to the present normal field and antipodal to the characteristic reversed direction, which decays to the origin for AF demagnetization above 20 mT. In the upper 47-m zone at Site 848, AF demagnetization to 15 mT removed most of the secondary overprint, and the "cleaned" inclinations are broadly consistent with expected geocentric axial dipole values of about ±6° for this latitude (Figs. 19, 20, and 21). Inclinations from Hole 848C are slightly steeper, as will be discussed below. In the zone between 47 and 72 mbsf, steep negative inclinations remain after demagnetization; these are accompanied by highly scattered declinations. Shipboard measurements did not allow us to determine magnetic polarity zonation. From 72 mbsf to basement, the

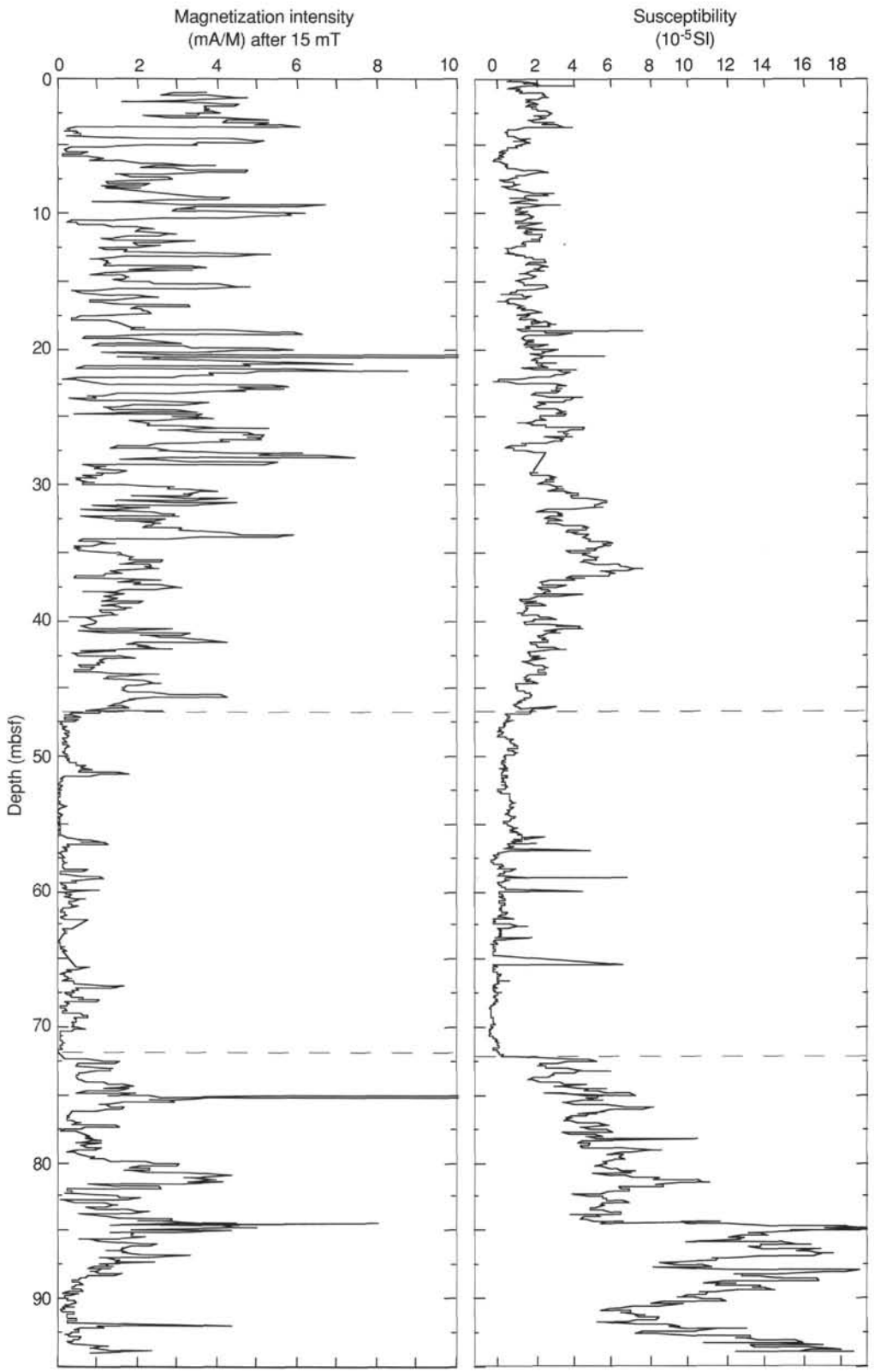

Figure 17. Profiles down the core of magnetization intensity, AF demagnetized at 15 mT, and magnetic susceptibility for Hole 848D, showing three zones that occur at all three holes at Site 848.

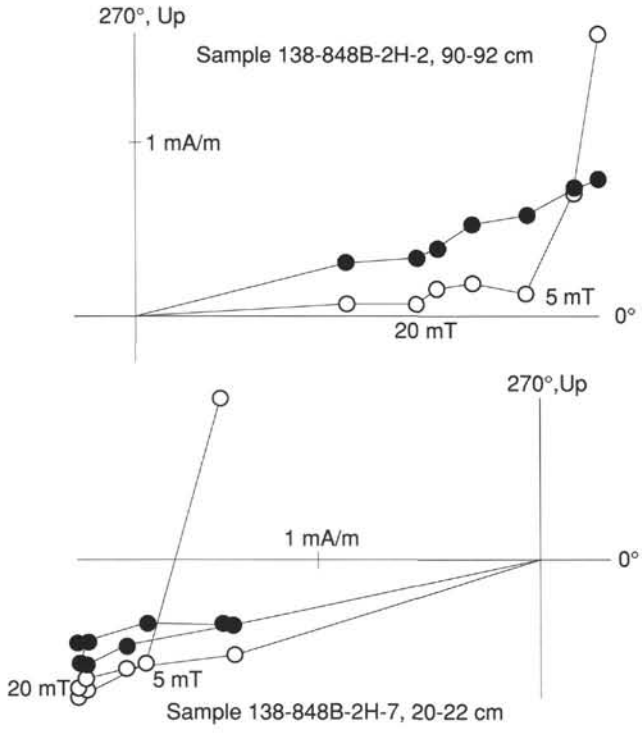

Figure 18. Diagrams of vector projection demagnetization of two discrete samples at Site 848, showing the ubiquitous vertical upward overprint, which for these samples has been removed with 5-mT AF demagnetization. The reverse sample (bottom) also exhibits a Brunhes-age viscous overprint. Solid (open) circles denote projection onto horizontal (vertical) plane. Azimuthal orientation is with respect to the double fiducial line.

demagnetized remanence was sufficiently clean to resolve polarity intervals; however, some of the overprint remains, as indicated by the steeper than expected negative inclinations. The persistence of the secondary overprint at Site 848 probably is the reason that these inclinations are skewed to negative values for all three holes (848B, 848C, and 848D; Fig. 22).

At these low latitudes, polarity reversals primarily are identified by declination patterns. The magnetostratigraphy at Site 848 benefited significantly from multishot orientation (Table 6). In the upper zone (0–47 mbsf), magnetic polarity chronozones were readily identified and correlated to the magnetic polarity time scale. In this zone, the demagnetized remanence was largely free from the drilling overprint, and the polarity sense often could be determined from the inclination profile. This was particularly true for Hole 848C, where the stable inclination values had somewhat higher absolute values. Indeed, multishot results for the drift of the hole indicated that the higher-than-expected inclination values resulted from nonvertical penetration, which averaged about 8° drift to the south (Table 6). The drift of Holes 848B and 848D was more typical, between 1° and 2° away from the vertical.

The locations of all identified reversal boundaries agree well among the three holes when adjusted to a composite depth scale (Fig. 23). The upper 47 m of the composite magnetostratigraphy contains every major polarity chronozone and subchronozone between the Brunhes and the Thvera in the Gilbert to about 4.7 Ma. In the lowest 20 to 25 m of the section, where the residual overprint was more pervasive, we had more difficulty identifying magnetic chronozones and correlating them unambiguously with the magnetic polarity time scale. Nevertheless, the polarity zonation in the bottom 20 to 25 m of the section correlates with late Miocene Chrons C4-n1 to C5-n2, which span ages from about 6.8 to 10.5 Ma. These correlations (Fig. 23 and Table 7) represent our best effort to achieve consistency among the magnetic polarity time scale (MPTS), available biostratigraphy, and the presumed smooth variations of sediment accumulation rates.

Although we had difficulty resolving narrow polarity zones with the pass-through magnetometer, two short normal intervals found at this site may indicate short-duration geomagnetic events. One feature is just below the Gauss/Gilbert boundary. The second normal feature appears between what we have interpreted as C4A-n1 and C4A-n2. Both of these normal events are found in both Holes 848C and 848D. In addition, in all three holes at Site 848 we recorded a thin reversed zone near the top of C5-n1, probably the uppermost of the four documented reversed intervals within C5-n1 (Mcdougall et al., 1976).

SEDIMENTATION RATES

A sedimentary section almost 100 m thick that spanned the time interval from the late Pleistocene to the base of the late Miocene was recovered at Site 848. Excellent magnetostratigraphy was available in the upper 46 m and in the 20 m above basement. Biostratigraphic age control was provided by all four of the chief planktonic microfossil groups. Magnetostratigraphy was especially important in that it documented, with elegant detail, the history of changes in sedimentation rate over the past 5 m.y. Control on changes in sedimentation rates after an interval of slow sedimentation rate at about 10 m.y. ago was equally good, although identification of the magnetochrons was less certain, as was their absolute chronology.

The composite depth section for Site 848 is given in Table 8. This composite was formed by comparing shipboard measurements of GRAPE, magnetic susceptibility, and percentage of reflectance (from the automated color analyzer) at adjacent holes. These comparisons then were integrated to form a single composite depth section for that site (a detailed discussion about the construction of composite sections during Leg 138 can be found in Hagelberg et al., this volume). For the holes and cores listed in Column 1 of Table 8, Column 2 gives the ODP sub-bottom depth of the core. The depth given in Column 2 corresponds to the depth of the bottom of the recovered core. This depth places the core catchers in their correct position in the composite depth section and is not the same as the standard ODP core-catcher depth. Column 3 shows the length of core recovered. Column 4 gives the composite depth of the core. Column 5 indicates the amount of offset between the ODP depth and the composite depth. Conversion from ODP sub-bottom depths to composite depths was done by adding the offset listed in Column 5 for a given core.

Both GRAPE density and percentage of reflectance data produced records having high amplitudes and variability through much of the section in Holes 848A (1 core), 848B, 848C, and 848D at Site 848 (Fig. 24, back-pocket). Although the percentage of reflectance record showed very low amplitude variability from 60 to 80 mcd, the transitions to and from this region of very high reflectance served as excellent correlation points. Magnetic susceptibility data produced records having low amplitudes from about 50 to 80 mcd, but increasing amplitudes from 80 to 105 mcd (coincident with the appearance of metalliferous sediments).

Analysis of the composite section indicates that overlapping of adjacent holes was maintained down through the bottom of the sedimentary record at Site 848. However, a detailed examination indicates that the problem of distortion within cores was more acute at this site than at previous Leg 138 sites (Sites 844 through 847). Perhaps this is because of the reduced sedimentation rates in much of the Site 848 record relative to previous sites (see below), which reduced the scale of the main features we were correlating. An accurate composite section will require stretching and compressing features within a core relative to the corresponding features in adjacent holes. Despite this distortion, the composite section for Site 848 remains satisfactory for documenting the recovery of a continuous record and providing the basis for planning a high-resolution sampling strategy.

For most of the record, sedimentation rates were derived from the high-resolution paleomagnetic record. Only in the interval between

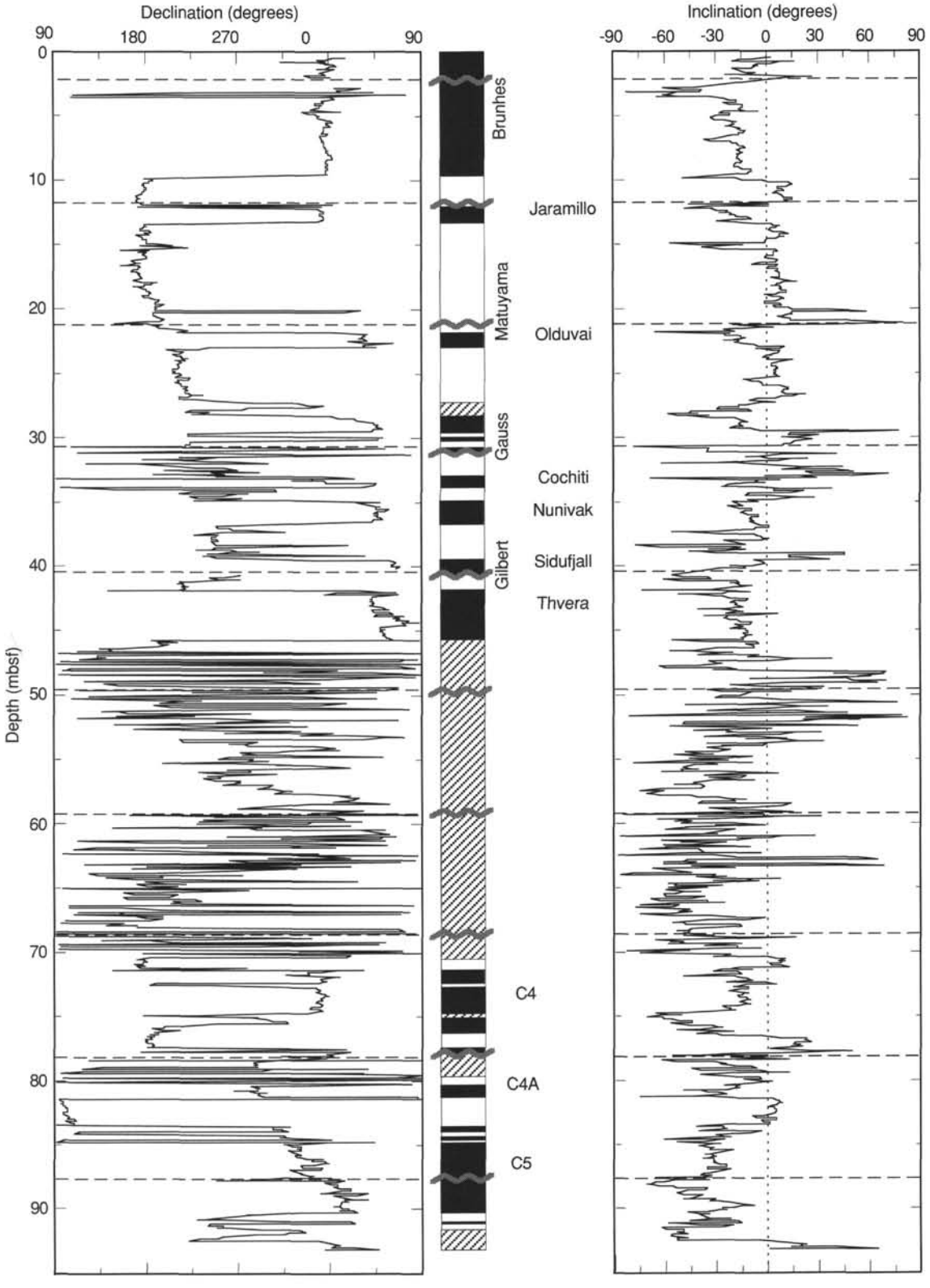

Figure 19. Declination and inclination profiles from the pass-through magnetometer, demagnetized at 15 mT, and identification of polarity chronozones in Hole 848B. Black = normal, white = reverse, hatched lines = no data or no interpretation. Dashed lines indicate core boundaries. Declinations have been rotated as described in Table 6.

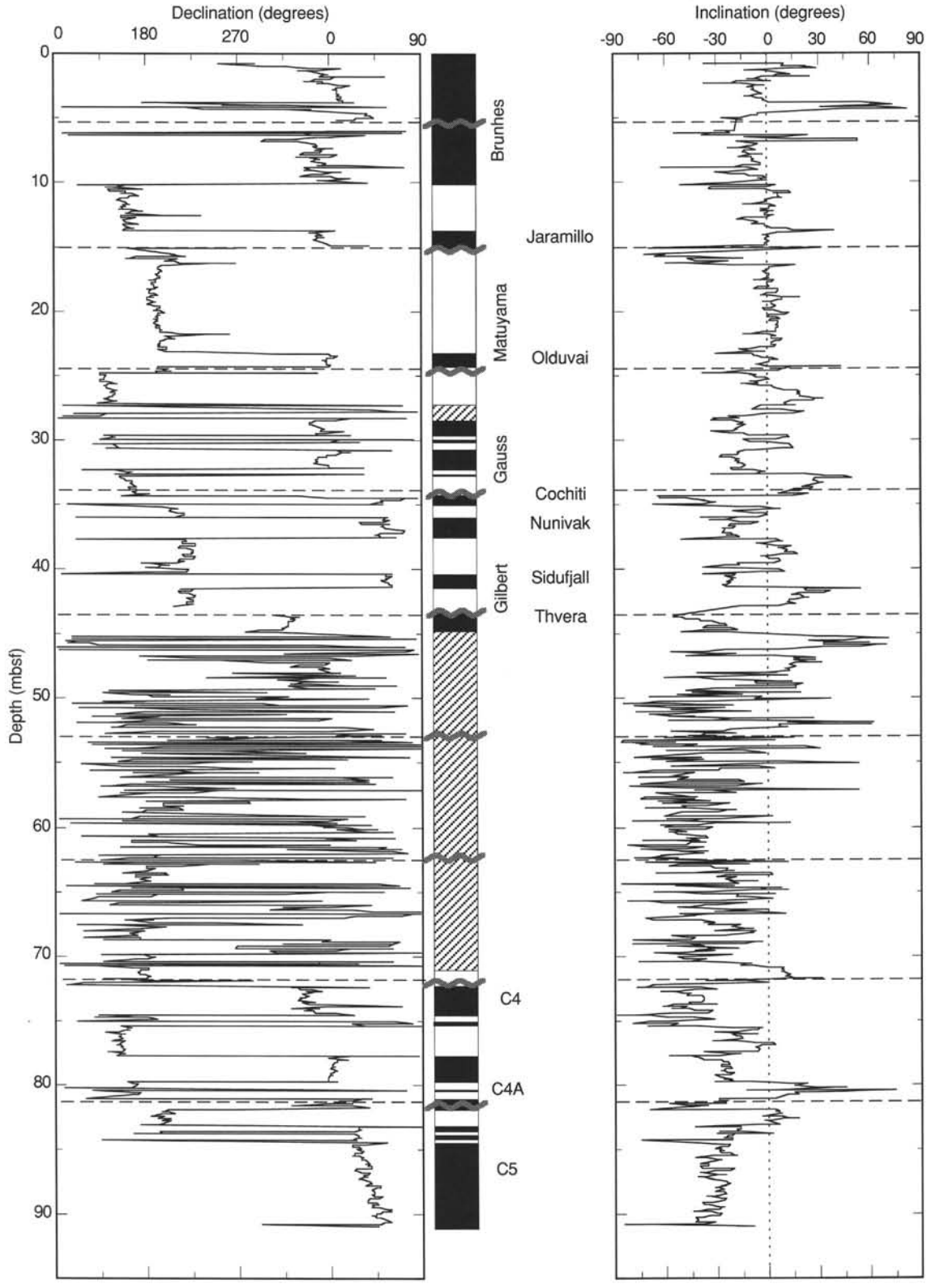

Figure 20. Declination and inclination profiles from the pass-through magnetometer, demagnetized at 15 mT, and identification of polarity chronozones in Hole 848C. Black = normal, white = reverse, hatched lines = uninterpreted. Dashed lines indicate core boundaries. Declinations have been rotated as described in Table 6.

Table 3. Sample and depth constraints of calcareous nannofossil events for Site 848.

Event	Hole 848B			Hole 848C		
	Interval (cm)	Depth (mbsf)	Depth (mcd)	Interval (cm)	Depth (mbsf)	Depth (mcd)
T *Pseudoemiliania lacunosa*	1H-4, 60–1H-5, 60	4.10–5.60	4.30–5.80	1H-CC–2H-CC	5.47–15.45	5.47–17.70
B *Gephyrocapsa* sp. 3	3H-1, 60–3H-1, 70	12.30–12.40	16.25–16.35			
T *Calcidiscus macintyrei*	3H-6, 80–3H-7, 17	20.20–20.87	24.15–24.82	2H-CC–3H-CC	15.45–25.06	17.70–28.06
B *Gephyrocapsa oceanica* s.l.	3H-6, 80–3H-7, 17	20.20–20.87	24.15–24.82	3H-5, 40–3H-5, 50	21.40–21.50	24.40–24.50
T *Discoaster brouweri*	4H-1, 140–4H-2, 47	22.60–23.17	27.01–27.52	3H-7, 30–3H-7, 40	24.30–24.40	27.30–27.40
AO *Discoaster triradiatus*				4H-1, 25–4H-1, 35	24.55–24.65	28.75–28.90
T *Discoaster pentaradiatus*	4H-4, 40–4H-4, 80	26.10–26.50	30.45–30.85	3H-CC–4H-CC	25.06–34.57	28.06–38.82
T *Discoaster surculus*	4H-4, 40–4H-4, 80	26.10–26.50	30.45–30.85	3H-CC–4H-CC	25.06–34.57	28.06–38.82
T *Discoaster tamalis*	4H-5, 23–4H-5, 85	27.43–28.05	31.78–32.40			
T *Sphenolithus* spp.	4H-CC–5H-1, 42	31.17–31.12	35.52–36.77	3H-CC–4H-CC	25.06–34.57	28.06–38.82
T *Reticulofenestra pseudoumbilicus*	5H-1, 95–5H-2, 50	31.65–32.70	37.30–38.35	3H-CC–4H-CC	25.06–34.57	28.06–38.82
T *Amaurolithus primus*	5H-2, 127–5H-3, 62	33.47–34.32	39.12–39.97	4H-CC–5H-CC	34.57–43.40	38.82–47.95
T *Ceratolithus acutus*	6H-1, 75–6H-2, 35	40.95–42.05	46.65–47.75	4H-CC–5H-CC	34.57–43.40	38.82–47.95
B *Ceratolithus rugosus*	6H-4, 35–6H-4, 75	45.05–45.45	50.75–51.15			
B *Ceratolithus acutus*	6H-5, 36–6H-5, 75	46.55–46.95	52.90–53.30			
T *Discoaster quinqueramus*	7H-1, 50–7H-1, 95	50.20–50.65	56.90–57.25	6H-7, 8–6H-CC	52.58–53.53	58.93–59.88
B *Amaurolithus primus*	8H-6, 85–8H-7, 20	67.55–68.40	75.00–75.85	8H-4, 40–8H-4, 60	67.40–67.60	76.50–76.70
B *Discoaster berggreni*	9H-3, 100–9H-4, 40	72.50–73.60	82.10–83.20	8H-CC–9H-CC	72.31–82.00	81.41–91.80
T *Discoaster hamatus*	10H-3, 108–10H-4, 10	81.28–82.80	91.88–95.15			
T *Coccolithus miopelagicus*	10H-CC–11H-1, 20	88.16–87.90	98.76–100.25	9H-CC–10H-CC	82.00–91.37	91.80–102.12
B *Discoaster hamatus*	11H-1, 50–11H-1, 90	88.50–88.90	100.85–101.25			

T = top occurrence; B = bottom occurrence.

50 (in the Thvera subchron) and 80 mcd (above the top of C4-n1) was magnetic control absent. Because magnetostratigraphy was available for Holes 848B, 848C, and 848D, we converted the depth of each reversal to composite depth for each hole and then averaged the values so as to improve the resolution in the age vs. depth plots shown in Figure 25. Plots of sedimentation rates vs. age and vs. depth are shown in Figures 26 and 27. The rate is about 17 m/m.y. over the past million years, 13 m/m.y. in the lower Pleistocene, and only about 6 m/m.y. over most of the Pliocene. Between 6.7 and 4.5 Ma, the sedimentation rate averaged 15 m/m.y.; the decrease to Pliocene values took place over the interval 4.3 to 3.9 Ma. Between 6.7 and 10.5 Ma (the bottom of the sedimentary sequence), the rate was about 5 m/m.y. and again, the timing of the increase in sedimentation rate at the end of this interval is well constrained at about 6.7 Ma.

No magnetostratigraphy is available for the interval between 4.5 and 6.7 Ma. However, biostratigraphy suggests that the sedimentation rate must have been fairly constant through that interval. In particular, the diatom datums shown in Figure 25B suggest that the sedimentation rate must have been constant over the interval without paleomagnetic control. In Table 9, we present the control points selected to generate the plots of age vs. depth shown in Figure 25A through Figure 25D. In these figures, the limits within which biostratigraphic datums were determined (see "Biostratigraphy" section, this chapter) were plotted with the published age estimates.

INORGANIC GEOCHEMISTRY

We collected 10 interstitial water samples at Site 848, three from Hole 848A at depths ranging from 1.5 to 7.5 mbsf and seven from Hole 848B from 20.7 to 92.2 mbsf (Table 10). These 10 samples span the entire sediment column at this location. The results from the two holes are considered to constitute a single depth profile for this section.

Three interstitial water samples were selected from the solitary core that makes up Hole 848A. Sediments in this core grade from a pale brown diatom nannofossil foraminifer ooze with radiolarians in the first section, to a yellowish-brown clayey diatom nannofossil foraminifer ooze with radiolarians in the second section (see "Lithostratigraphy" section, this chapter). Below Section 138-848A-1H-2, sediments alternate between white to light gray diatom nannofossil foraminifer ooze and radiolarian diatom foraminifer nannofossil ooze.

Interstitial-water sampling in Hole 848B began with a sample from the bottom of the last complete section of the third core (Section 138-848B-3H-6). The sediments in this core consist of interbedded, very gray foraminifer nannofossil ooze with radiolarians and diatoms and light greenish-gray diatom radiolarian foraminifer nannofossil ooze. The next interstitial sample (138-848B-6H-6) was taken from the very pale gray diatom nannofossil ooze with radiolarians that constitutes the last section of this core. One interstitial water sample was taken from every core below Core 138-848B-6H through the deepest core recovered from this hole, Core 138-848B-11H. Cores 138-848B-6H through -9H consist mainly of radiolarian nannofossil ooze. A color change to dark yellowish brown sediment occurs in Section 138-848B-10H-3 that marks a transition to metalliferous nannofossil ooze, characterized by oxide contents up to 20% (see "Lithostratigraphy" section, this chapter). The interstitial-water sample from this core was taken within a zone of metalliferous sediment.

Sediment recovered from the last core shifts away from a distinct metalliferous sediment back to mainly foraminifer nannofossil ooze with interbedded light/dark intervals, with the darker bands containing up to 5% oxides. Core 138-848B-11H also contains minor amounts of clay and volcanic glass. The interstitial-water sample from this core (138-848B-11H-3) was taken in one of the darker (most hydrothermally affected) bands.

Above 80 mbsf, chemical gradients of most parameters at Site 848 are subtle (Table 10). While distinct kinks exist in some of these interstitial-water profiles at the bottom of the hole, many do not seem to show a discernable change above this point. This observation is quantified in Table 11, which examines the overall changes in concentration down the core relative to our ability to measure these parameters on board the ship. This table sorts the dissolved chemical parameters measured during this leg into four categories: diagenesis, crystallization, alteration, and advection. These broad categories encompass the various geochemical processes that can influence interstitial-water chemistry in this study area.

The only diagenetic indicator to show a measurable change above 80 mbsf was alkalinity (Fig. 28C). Alkalinity was highest in the shallowest sample (2.941 mM at 1.5 mbsf) and decreased gradually down the core (2.817 mM at 77.7 mbsf). The shape of this profile and the fact that the overall change is small indicate that the sediments here are oxidizing, and that active diagenesis has been restricted to the sediment/water interface. This scenario is consistent with the

Table 3 (continued).

Event	Hole 848D Interval (cm)	Depth (mbsf)	Depth (mcd)
T *Pseudoemiliania lacunosa*	1H-CC	0–8.44	0.20–8.64
B *Gephyrocapsa* sp. 3			
T *Calcidiscus macintyrei*	2H-CC–3H-CC	18.28–27.81	20.23–30.51
B *Gephyrocapsa oceanica* s.l.			
T *Discoaster brouweri*	2H-CC–3H-CC	18.28–27.81	20.23–30.51
AO *Discoaster triradiatus*			
T *Discoaster pentaradiatus*			
T *Discoaster surculus*			
T *Discoaster tamalis*			
T *Sphenolithus* spp.	3H-CC–4H-CC	27.81–37.16	30.51–39.76
T *Reticulofenestra pseudoumbilicus*	3H-CC–4H-CC	27.81–37.16	30.51–39.76
T *Amaurolithus primus*			
T *Ceratolithus acutus*	3H-CC–4H-CC	27.81–37.16	30.51–39.76
B *Ceratolithus rugosus*	4H-CC–5H-CC	37.16–46.75	39.76–50.75
B *Ceratolithus acutus*	6H-1, 50–6H-1, 100	46.90–47.40	51.90–52.40
T *Discoaster quinqueramus*	6H-5, 50–6H-5, 100	52.90–53.40	57.90–58.40
B *Amaurolithus primus*	6H-CC–7H-CC	56.40–65.07	61.40–71.87
B *Discoaster berggreni*	8H-CC–9H-CC	75.42–84.78	82.92–92.98
T *Discoaster hamatus*			
T *Coccolithus miopelagicus*	9H-CC–10H-CC	84.78–94.37	92.98–103.67
B *Discoaster hamatus*			

relatively low, recent sedimentation rate at this location (see "Sedimentation Rates" section, this chapter). In other words, material deposited at this site has a long residence time at the sediment/water interface before burial. A slow burial rate implies three main ramifications:

1. Most organic carbon is broken down near the interface by bottom-water oxygen, which explains why little organic carbon is being buried at this site (see "Organic Geochemistry" section, this chapter).
2. The breakdown of organic matter near the interface imparts a corrosive character to interfacial pore and bottom waters, which is consistent with the poor preservation of fossils recorded at this site (see "Biostratigraphy" section, this chapter).
3. Because most labile organic matter is broken down near the interface, nothing fuels diagenesis deeper in the sediment column, which is consistent with the decreasing trend of alkalinity down the core and with the absence of detectable sulfate reduction and ammonia (Table 11), as well as the vanishingly small amounts of methane detected at this site (see "Organic Geochemistry" section, this chapter).

In the absence of late diagenesis, crystallization is the only process active within the mid-sediment column at Site 848 (Table 11). Calcium (Fig. 29B) and silica (Fig. 29D) display only subtle, semi-linear changes down the core, which can be explained as diffusional trends between basement and the sediment/water interface. On the other hand, strontium (Fig. 30B) and lithium (Fig. 30A) display a distinct, broad mid-profile maximum and minimum, respectively. Concentrations of interstitial strontium are known to increase during the recrystallization of calcite (Elderfield and Gieskes, 1982; Gieskes et al., 1986). It is likely that the profiles of interstitial strontium at this site (Fig. 30B) have been affected by this process. By analogy, the lithium profile is consistent with removal during this process. One should note, however, that the mid-sediment column anomalies in lithium and strontium that we observed at this site are small when compared to those found at other sites drilled during Leg 138.

Several of the interstitial-water profiles at this site show distinct anomalies near the bottom of the hole. The decreases in sodium (Fig. 28A), chloride (Fig. 28B) and magnesium (Fig. 29A) are consistent with diffusive exchange through the sediment column that is driven by uptake during low-temperature alteration of basalt (McDuff, 1981; Gieskes and Lawrence, 1981). Sodium and chloride are taken up during hydration reactions and the albitization of plagioclase. Weathering of basalt consumes magnesium during the production of Mg-smectites and Mg-hydroxysilicates. Alkalinity (Fig. 28C) also decreases near the basement, which can be accounted for by veins of calcite found in several fragments of altered basalt.

In summary, active diagenesis at Site 848 has been restricted to the top of the sediment column by the low sedimentation rate. Calcium (Fig. 29B), silica (Fig. 29D), strontium (Fig. 30B) and lithium (Fig. 30A) indicate that some recrystallization is going on within the sediment column, but that this process is less effective than at most other sites drilled during this leg. Alteration of basement rocks is influencing the profiles of sodium, chloride, alkalinity, magnesium, potassium, and silica to varying degrees, but these effects are small and restricted to the bottom of the hole.

Sediment Chemistry

Several sediment samples that represent whole sections of core were analyzed by x-ray fluorescence spectroscopy (Table 12). To eliminate the possibility that the minor surface irregularities caused by splitting the core with a wire had introduced noise in the color reflectance records, we scraped the cores cross-wise with glass microscope slides before scanning them. This process removed about 10 cm^3 of sediment from each section. This sediment represents an integrated sample of the entire section. We analyzed the sediment scraped from the first section of cores from Site 848 to provide an average record of the sediment chemistry that had not been aliased by the extensive variability in lithology in single sections. To treat all parts of the core similarly, we scraped each entire section regardless of whether individual portions of the section were smooth after being split. Each scrape overlapped the previous one very little. The sediments were analyzed by x-ray fluorescence spectroscopy for major elements using the methods described in the "Explanatory Notes" chapter (this volume).

Concentrations of calcium carbonate are high in most sediments. The shipboard algorithm used to calculate composition from the x-ray fluorescence intensity data was optimized for igneous rocks; we encountered several problems when interpreting the composition data. For example, the concentrations indicated for MgO are negative because of the overlapping of the Ca and Mg fluorescence wavelengths used for the analysis and because we used corrections for this overlapping that have been based on an igneous rock matrix. The high concentrations of Ca in the sample also interfered with our analyses of K_2O and Na_2O. Concentrations of TiO_2 were positive, but very

Table 4. Sample and depth constraints of radiolarian events for Site 848.

Event	Hole 848B			Hole 848C		
	Interval	Depth (mbsf)	Depth (mcd)	Interval	Depth (mbsf)	Depth (mcd)
T *Stylatractus universus*	1H-CC–2H-3	2.23–6.30	5.47–9.10	1H-CC–2H-CC	5.47–15.45	5.47–17.70
B *Collosphaera tuberosa*	2H-3–2H-5	6.30–9.30	9.10–12.30			
T *Lamprocyrtis neoheteroporus*	2H-CC–3H-3	12.27–15.82	15.45–19.75	2H-CC–3H-CC	15.45–25.06	17.70–28.06
T *Anthocyrtidium angulare*	2H-CC–3H-3	12.27–15.82	17.70–19.75	2H-CC–3H-CC	15.45–25.06	17.70–28.06
T *Theocorythium vetulum*	2H-CC–3H-3	12.27–15.82	17.70–20.23	2H-CC–3H-CC	15.45–25.06	
B *Lamprocyrtis nigriniae*	3H-3–3H-5	15.82–18.82	20.23–22.75			
B *Theocorythium trachelium*	3H-5–3H-CC	18.82–21.73	22.75–25.68			
B *Pterocorys minithorax*	3H-CC–4H-3	21.73–25.30	25.68–28.06	2H-CC–3H-CC	15.45–25.06	17.70–28.06
B *Anthocyrtidium angulare*	3H-CC–4H-3	21.73–25.30	25.68–28.06			
T *Pterocanium prismatium*	3H-5–3H-CC	18.82–21.73	22.75–25.68			
T *Lamprocyrtis heteroporus*	3H-5–3H-CC	18.82–21.73	22.75–25.68			
T *Anthocyrtidium jenghisi*	3H-CC–4H-3	21.73–25.30	25.68–28.06			
B *Theocalyptra davisiana*	4H-3–4H-5	25.30–28.30	30.85–32.35	4H-2–4H-3	26.60–28.10	30.85–32.35
T *Stichocorys peregrina*	4H-3–4H-5	25.30–28.30	30.85–32.35	4H-2–4H-3	26.60–28.10	30.85–32.35
T *Anthocyrtidium pliocenica*	4HCC–5H-3	31.17–34.80	36.85–38.82	4H-6–4H-CC	32.60–34.57	36.85–38.82
B *Lamprocyrtis neoheteroporus*	4H-5–4H-CC	28.30–31.17	32.35–32.65	4H-2–4H-3	26.60–28.10	30.85–32.35
B *Lamprocyrtis heteroporus*	4H-5–4H-CC	28.30–31.17	33.85–35.35	4H-4–4H-5	29.60–31.10	33.85–35.35
T *Phormostichoartus fistula*	4H-CC–5H-3	31.17–34.80	35.52–36.85	4H-5–4H-6	31.10–32.60	35.35–36.85
T *Lychnodictyum audax*	5H-5–5H-CC	37.80–40.53	43.45–46.18			
T *Phormostichoartus doliolum*	4H-CC–5H-3	31.17–34.80	35.52–36.85	4H-5–4H-6	31.10–32.60	35.35–36.85
B *Amphirhopalum ypsilon*	4H-CC–5H-3	31.17–34.80	35.52–38.82	4H-6–4H-CC	32.60–34.57	36.85–38.82
B *Spongaster tetras*	5H-5–5H-CC	37.80–40.53	43.45–46.18			
T *Didymocyrtis penultima*	4H-CC–5H-3	31.17–34.80	36.85–38.82	4H-6–4H-CC	32.60–34.57	36.85–38.82
B *Pterocanium prismatium*	5H-CC–6H-3	40.53–44.30	46.18–47.95	4H-CC–5H-CC	34.57–43.40	38.82–47.95
T *Solenosphaera omnitubus*	5H-CC–6H-3	40.53–44.30	46.18–50.00			
T *Siphostichartus corona*	6H-5–6H-CC	47.30–50.17	53.00–55.87			
T *Acrobotrys tritubus*	8H-3–8H-5	63.30–66.30	70.75–71.87			
T *Stichocorys johnsoni*	7H-CC–8H-3	59.77–63.30	67.90–69.40	7H-5–7H-6	61.10–62.60	68.85–70.35
Stichocorys delmontensis > *S. peregrina*	8H-3–8H-CC	63.30–69.32	70.75–70.81	7H-6–7H-CC	62.60–63.06	70.35–70.81
T *Calocycletta caepa*	7H-CC–8H-3	59.77–63.30	67.90–69.40	7H-5–7H-6	61.10–62.60	68.85–70.35
B *Solenosphaera omnitubus*	8H-5–8H-CC	66.30–69.32	73.75–76.77			
T *Diartus hughesi*	8H-CC–9H-3	69.32–72.80	81.41–82.40	8H-CC–9H-CC	72.31–82.00	81.41–91.80
B *Acrobotrys tritubus*	8H-CC–9H-3	69.32–72.80	76.77–81.41	8H-CC–9H-CC	72.31–82.00	81.41–91.80
T *Stichocorys wolffii*	9H-CC–10H-1	78.58–79.70	88.18–90.30			
T *Botryostrobus miralestensis*	9H-3–9H-5	72.80–75.80	82.92–85.40			
T *Diartus pettersoni*	9H-5–9H-CC	75.80–78.58	85.40–88.18			

T = top; B = bottom; > = evolutionary transition.

small. Nonetheless, the sum of the major oxides accounted for by the analysis, after taking into account loss on ignition (Table 12), suggests that the data for Al_2O_3, SiO_2, CaO, Fe_2O_3, MnO_2, and P_2O_5 are very good. The high values for loss on ignition are typical of sediment samples that are rich in $CaCO_3$.

We compared several sets of sediment chemistry data with other data sets to determine whether the chemistry was reliable. Because virtually all of the CaO in the samples is from $CaCO_3$, we estimated the percentage of $CaCO_3$ from CaO (assuming that most of the loss on ignition was CO_2 driven off the carbonate) and compared these data to independent coulometric $CaCO_3$ measurements of the same samples (Table 13; Fig. 31) to verify the CaO analyses. These data suggest that the CaO measurements are about 5 wt% too high, but that the difference between the two values is linear. These data give credence to the other elemental data, but indicate that the analytical data should be recalculated to account for the relationship of loss on ignition to carbonate content.

Biogenic Silica

When recalculated on a carbonate-free basis (Table 14), the chemical analyses indicate that the sediments are very rich in silica (Fig. 32). The element suite allowed us to make a rough estimate of the biogenic silica content of the sediments. The crustal ratio of SiO_2/Al_2O_3 is roughly 3.0. Measurements of this ratio in Cenozoic equatorial Pacific Ocean sediments (Leinen, 1979) indicate that this value is reasonable for our samples. Therefore, an estimate of the biogenic silica content of the sediments (Fig. 32) can be obtained from the following:

$$SiO_{2\,(biogenic)} = SiO_{2\,(total)} - (3 \times Al_2O_3).$$

The error using this estimate is less than ±5 wt% biogenic silica (Leinen, 1977). Our estimate for biogenic silica suggests that the sediment contains about 5% to 20% biogenic silica (~40%–70% on a carbonate-free basis) and confirms the importance of siliceous sediment in the intervals between 40 and 60 mbsf. Below 70 mbsf, carbonate-free biogenic silica contents decrease by roughly 20%.

Elements from Terrigenous and Hydrothermal Sources

Concentrations of aluminum in the samples are greatest at the top of the interval of analyzed samples (30–35 mbsf) and near the base of the sediment column. As an additional check on the reasonability of our chemical data, we calculated the weight percent of aluminum on a carbonate- and biogenic silica-free basis (Fig. 33). Values average 6% to 7%, near the average crustal value, confirming that our data for aluminum are reasonable in spite of the high carbonate contents and problems with analyses for Mg, Na, and K.

The Fe content of the sediment increases dramatically below 80 mbsf (Fig. 33). When calculated on a carbonate- and biogenic silica-free basis, this increase is even sharper; elemental Fe accounts for nearly 30% of the sediment. The Mn content is also large and increases sharply below 80 mbsf. The large Fe/Al ratio (up to 7) indicates that most of this Fe is not terrigenous (Fig. 34). Heath and Dymond (1977) calculated the hydrothermal Fe concentration of equatorial Pacific Ocean sediments assuming that the only significant sources of Fe were terrigenous sediment and hydrothermal phases and that the

Table 4 (continued).

Event	Hole 848D Interval	Depth (mbsf)	Depth (mcd)
T *Stylatractus universus*	1H-1–1H-CC	8.44	0–8.64
B *Collosphaera tuberosa*			
T *Lamprocyrtis neoheteroporus*			
T *Anthocyrtidium angulare*			
T *Theocorythium vetulum*	2H-CC–3H-CC	18.28–27.81	20.23–30.51
B *Lamprocyrtis nigriniae*	1H-CC–2H-CC	8.44–18.28	8.64–20.23
B *Theocorythium trachelium*			
B *Pterocorys minithorax*			
B *Anthocyrtidium angulare*			
T *Pterocanium prismatium*			
T *Lamprocyrtis heteroporus*			
T *Anthocyrtidium jenghisi*			
B *Theocalyptra davisiana*			
T *Stichocorys peregrina*			
T *Anthocyrtidium pliocenica*			
B *Lamprocyrtis neoheteroporus*			
B *Lamprocyrtis heteroporus*			
T *Phormostichoartus fistula*			
T *Lychnodictyum audax*			
T *Phormostichoartus doliolum*			
B *Amphirhopalum ypsilon*			
B *Spongaster tetras*			
T *Didymocyrtis penultima*			
B *Pterocanium prismatium*			
T *Solenosphaera omnitubus*			
T *Siphostichartus corona*			61.40–71.87
T *Acrobotrys tritubus*	6H-CC–7H-CC	56.40–65.07	
T *Stichocorys johnsoni*			
Stichocorys delmontensis > *S. peregrina*			
T *Calocycletta caepa*			
B *Solenosphaera omnitubus*	7H-CC–8H-CC	65.07–75.42	71.87–92.92
T *Diartus hughesi*			
B *Acrobotrys tritubus*			
T *Stichocorys wolffii*			
T *Botryostrobus miralestensis*	8H-CC–9H-CC	75.42–84.78	82.92–92.98
T *Diartus pettersoni*			

terrigenous contribution of Fe to the sediments was proportional to the Fe/Al crustal ratio, 0.6, as follows:

$$\text{wt\% hydrothermal Fe} = \text{wt\% Fe} - (0.6 \times \text{\%Al})$$

The hydrothermal Fe content of the basal sediments calculated in this manner (Fig. 34) is about 25% of the nonbiogenic sediment (2%–3% of the total sediment).

The chemistry of Site 848 sediments also shows this characteristic pattern of Fe/Mn with distance from the ridge crest (Fig. 34). The Fe/Mn ratio is near 3 in the lowermost sediments at the site. This ratio increases in younger (shallower) sediments that were deposited as the site migrated away from the ridge crest. The ratio reaches a maximum of 15 in sediments between 50 and 65 mbsf that were deposited about 6 m.y. after the site left the ridge crest. The ratio has decreased since that time.

Lyle (1986) showed that the Fe/Mn ratio of sediments in subtropical South Pacific Ocean DSDP Sites 597 through 599 changed with paleodistance from the ridge crest. The Fe/Mn ratio of sediments deposited at the ridge crest was roughly 3, near the average ratio in present-day hydrothermal sediments (Heath and Dymond, 1977). As the Leg 138 sites moved away from the ridge crest as a result of seafloor spreading, this ratio first increased, then decreased. The increase began after the sites were approximately 200 to 250 km away from the ridge crest. Lyle postulated that this systematic change in Fe/Mn ratio resulted from the fractionation of Fe and Mn during transport of the extremely fine-grained hydrothermal oxides away from the ridge crest. The Fe/Mn ratio of Site 848 sediments begins to increase at 85 mbsf in sediments deposited 7.4 Ma (see "Sedimentation Rates" section, this chapter). These sediments were deposited about 270 km from the ridge crest.

Accumulation Rates

The mass accumulation rate (g/cm^2/k.y.) of estimated biogenic SiO_2 (opal; Fig. 35, Table 15) was calculated for the intervals represented by the XRF samples, using the mass accumulation rates (MAR) from Table 16. Although few biogenic SiO_2 accumulation rate data are evident, the integrated samples ensure that these data were not aliased by the decimeter-scale variability in sedimentation. Opal accumulation rates for samples older than 4 Ma are greatest between 4.5 and 5.5 Ma (~0.2 g/cm^2/k.y.) and about 8.5 Ma; the temporal pattern is most like that of organic carbon (e.g., see Fig. 39; "Organic Geochemistry" section, this chapter). The older opal accumulation rate maximum corresponds to the upper part of the radiolarian-rich zone at 82 to 92 mbsf (Hole 848B; see Fig. 7 in "Lithostratigraphy" section, this chapter). The younger opal accumulation rate maximum corresponds to radiolarian- and diatom-rich sediments between 41.5 and 54.5 mbsf.

The MAR of Al (Fig. 35, Table 15) is a good indicator of the influence of terrigenous sediment at Site 848. As the crustal abundance of Al is about 7%, the accumulation rate of all terrigenous material should be roughly an order of magnitude greater than that of Al, or about 1 to 4 mg/cm^2/k.y. The Al accumulation rate is greatest between 4.5 and 5.5 Ma and coincides with the opal accumulation rate maximum. A second interval of high accumulation rates occurred about 9 Ma, just before the older interval of high opal accumulation rates. Although a third accumulation rate peak occurred about 10.5 Ma, this was represented by the basal sediment sequence at the site. Sedimentological evidence exists that the deposition immediately after the site formed at the ridge crest was influenced by bottom

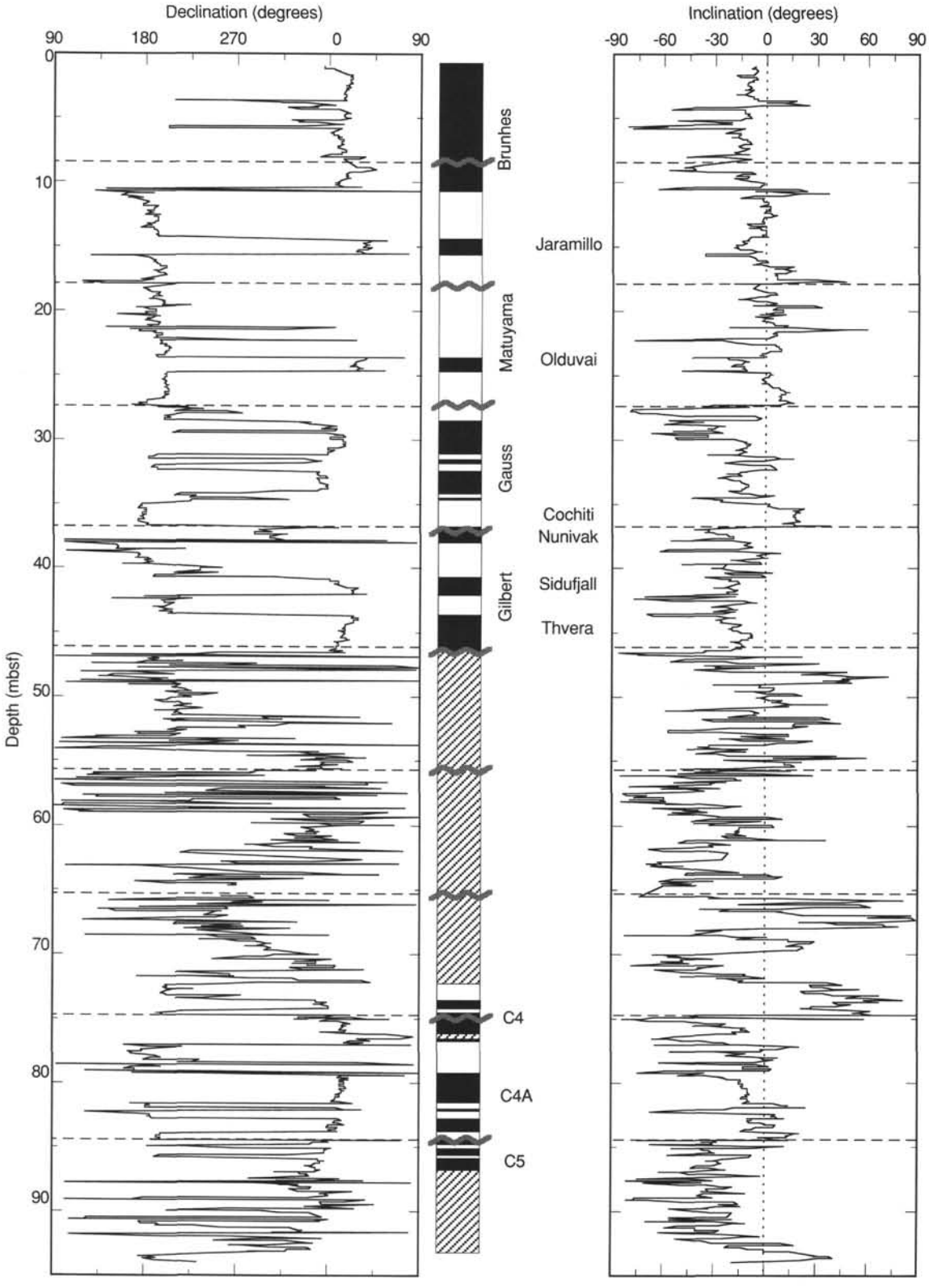

Figure 21. Declination and inclination profiles from the pass-through magnetometer, demagnetized at 15 mT, and identification of polarity chronozones in Hole 848D. Black = normal, white = reverse, hatched lines = no data or no interpretation. Dashed lines indicate core boundaries. Declinations have been rotated as described in Table 6.

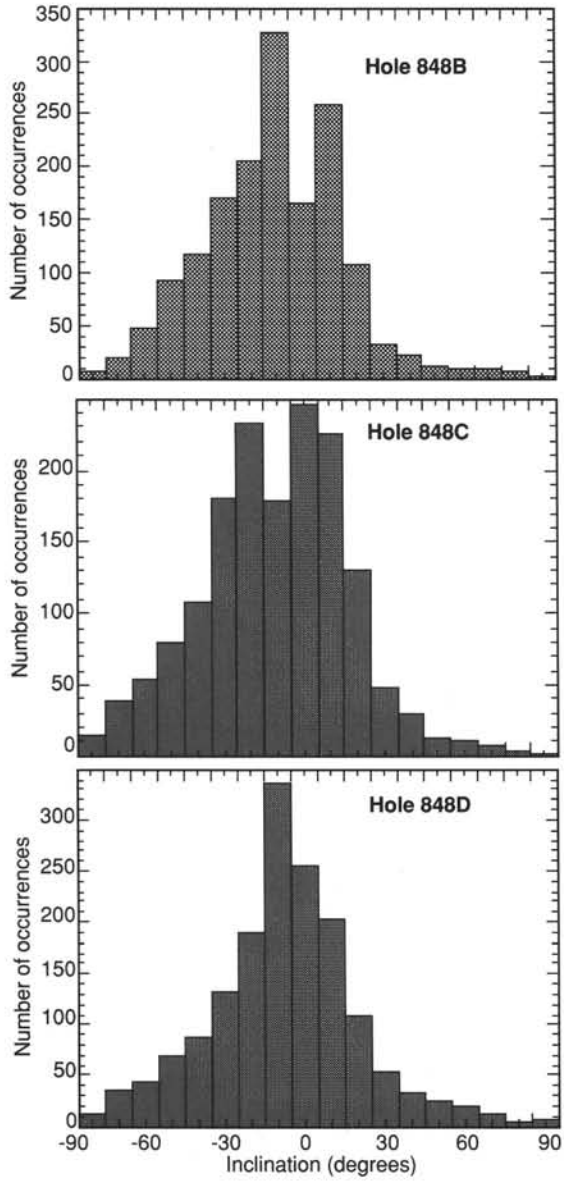

Figure 22. Histograms of inclinations measured using the pass-through magnetometer for Holes 848B, 848C, and 848D, after AF demagnetization to 15 mT. Distributions are skewed to negative inclinations, showing residual upward-directed (negative inclination) drilling overprint.

current reworking; thus, the sedimentation and accumulation rates in this interval are suspect.

The accumulation rate of Fe and Mn have been influenced by both terrigenous and hydrothermal sources. An accumulation rate for the hydrothermal component of Fe (Fig. 35, Table 15) was based on the assumptions discussed above. The hydrothermal Fe accumulation rate was greatest about 9 Ma, about 1.5 m.y. after the site had formed at the ridge crest. Hydrothermal accumulation is generally greatest very close to the ridge crest, but bottom current reworking and erosion around the rough ridge crest topography may have modified the accumulation of sediments very close to the ridge crest.

It is unusual for sediment deriving from very different sources to have coincident accumulation maxima, such as those for opal, Al, and hydrothermal Fe at about 4.5 to 5.5 Ma. However, the stratigraphy of this interval is well constrained by magnetic reversals. One hypothesis to explain a similar biogenic and terrigenous accumulation rate pattern is that the terrigenous material was transported to the site by the wind and that atmospheric circulation and upwelling were coupled. Such reasoning, however, does not explain an increase in hydrothermally derived elements like Fe and Mn. One possibility is that our analyses of Fe and Mn, the concentrations of which are very low in those sediments corresponding to the accumulation rate maximum, are within the limits of error for these high-carbonate sediments, or perhaps matrix effects result from the high carbonate concentrations.

ORGANIC GEOCHEMISTRY

Carbonate and Organic Carbon

Concentrations of inorganic and organic carbon were measured at Site 848 following the methods outlined in the "Explanatory Notes" chapter (this volume). The percentage of inorganic carbon was measured in physical property samples at a frequency of one to two samples per section. From the inorganic carbon data, we calculated the weight percent of calcium carbonate (%$CaCO_3$). The percentage of organic carbon (%C_{org}) was determined in approximately two samples per core in Hole 848B, using samples taken for headspace gas analysis and physical property samples. The percentage of C_{org} was measured as the total carbon in the dried residues from coulometric analysis (see "Explanatory Notes" chapter, this volume). This method was used in place of that used previously, which calculated the C_{org} as the difference between the carbon and the total inorganic carbon, because the percentage of C_{org} is low (usually less than 0.2%) throughout the entire sequence recovered at Site 848. The analytical results are listed in Table 17 (CD ROM, back pocket) with respect to both ODP depth (mbsf) and to composite depth (mcd; see "Sedimentation Rates" section, this chapter). If a duplicate analysis was performed on a given sample, the mean value of the original analysis and the duplicate is listed in Table 17 (CD ROM). Duplicate analyses of percentage of $CaCO_3$ analyses are listed in Table 18. The results indicate a reproducibility of 0.9%. In Figure 36, we show percentages of $CaCO_3$ and C_{org} in Hole 848B vs. ODP depth.

In Figure 37, one can see percentages of $CaCO_3$ and C_{org} vs. composite depth and age, based on 34 magnetochronostratigraphic levels (see "Sedimentation Rates" and "Paleomagnetism" sections, this chapter). The most striking feature in the Site 848 record is its low-percentage $CaCO_3$ interval in Core 138-848B-10H. This feature was interpreted as a severe carbonate dissolution event, based on the poor preservation of calcareous nannofossils (see "Biostratigraphy" section, this chapter). This event occurred near 9 Ma and is similar to the severe $CaCO_3$ dissolution events observed at approximately the same time in Sites 844, 845, and 846.

Accumulation Rates

Following the methodology outlined in the "Explanatory Notes" chapter (this volume), we calculated the average values of several sedimentary parameters in time intervals delimited by the chronostratigraphic levels discussed in the "Sedimentation Rates" section (this chapter). The average values of %$CaCO_3$ and %C_{org}, linear sedimentation rate (LSR), dry-bulk density (DBD), bulk-sediment MAR, $CaCO_3$ MAR, and C_{org} MAR for 34 time intervals since 11 Ma are listed in Table 16. The mean values are presented vs. composite depth in Figure 38 and vs. age in Figure 39. Superimposed on the mean values are estimates of the instantaneous MAR calculated for each sample. The accumulation rates of all sedimentary components are low at Site 848, rarely exceeding 1.5 g/cm^2/k.y. These rates are significantly lower than those encountered at Sites 846 and 847. Although the overall rates are lower, the pattern of sediment accumulation at Site 848 is similar to that observed at Sites 846 and 847. From 12 to 7 Ma, MARs were low at both Sites 846 and 848. Mass accumulation rates increased near 7 Ma at all three sites and remained high until 4 Ma. At this time, rates decreased by a factor of 2 at Site 848 and decreased by at least this much at Sites 846 and 847. The Pleistocene record at Site 848 differs from that at Sites 846 and 847 in that accumulation rates at Site 848 double from late Pliocene

Table 5. Sample and depth constraints of diatom events for Site 848.

Event	Hole 848 B			Hole 848C		
	Interval	Depth (mbsf)	Depth (mcd)	Interval	Depth (mbsf)	Depth (mcd)
T *N. reinholdii*	1H-CC–2H-CC	2.23–12.27	2.43–15.07	0–1H-CC	0–5.47	0–5.47
T *N. fossilis*	1H-CC–2H-CC	2.23–12.27	2.43–15.07	1H-CC–2H-CC	5.47–15.4	55.47–17.7
T *R. praebergonii*	3H-6–3H-CC	20.5–21.73	24.45–25.68	2H-CC–3H-CC	15.45–25.06	17.7–28.06
B *P. doliolus*	4H-1–4H-2	22.53–24.03	26.88–28.38	3H-CC–4H-1	25.06–24.9	28.06–28.46
T *T. convexa*	4H-3–4H-4	25.53–27.03	29.88–31.38	4H-1–4H-2	24.9–25.9	28.46–30.16
T *N. jouseae*	4H-4–4H-5	27.03–28.83	31.38–32.88	4H-2–4H-4	25.9–27.9	30.16–33.65
B *R. praebergonii*	4H-6–4H-7	30.03–30.42	34.38–34.77	4H-4–4H-CC	27.9–34.57	33.65–38.82
F *T. convexa s. ampl.*	5H-1–5H-2	31.9–33.4	37.55–39.05			
B *A. elegans*	4H-CC–5H-4	31.17–36.42	35.52–42.05			
T *N. cylindrica*	5H-4–5H-CC	36.42–40.53	42.05–46.18			
B *N. jouseae*	6H-2–6H-4	43.1–46.1	58.57–61.57			
T *N. miocenia*	7H-2–7H-CC	52.4–59.77	59.1–66.47	6H-CC–7H-CC	53.0–63.06	59.88–70.81
T *N. miocenica* var.	7H-5–8H-2	56.9–61.9	63.6–69.35			
T *T. praeconvexa*	7H-5–8H-2	56.9–61.9	63.6–69.35			
T *R. praepaleacea*	8H-2–8H-3	61.9–63.4	69.35–70.85			
B *T. miocenica*	8H-3–8H-4	63.4–64.4	70.85–71.85			
B *T. convexa* var. *aspinosa*	8H-3–8H-4	63.4–64.4	70.85–71.85			
B *B. praeconvexa*	8H-4–8H-5	65.0–66.5	72.35–73.85			
B *N. miocenica*	9H-2–9H-2	70.56–71.15	80.16–80.75			
T *R. paleacea*	9H-2–9H-2	70.56–71.15	80.16–80.75	7H-CC–8H-CC	63.06–72.31	70.81–81.41

T = top occurrence; B = bottom occurrence.

values, whereas little change was observed across the late Pliocene and Pleistocene in the eastern two sites.

Gas Geochemistry

We took samples for gas analysis from each core of Hole 848B. Gas was released from a sediment sample (about 5 cm^3) by thermal desorption (i.e., the headspace technique, see "Explanatory Notes" chapter, this volume) and the measured concentrations of hydrocarbons in the headspace volume (in ppm) were converted to µL/L of sediment and are reported in Table 19. Methane concentrations do not exceed 5 µL/L sediment; ethane and higher hydrocarbon gases are below detection limits.

PHYSICAL PROPERTIES

Introduction

Physical properties measured routinely on whole-round sections at Site 848 include GRAPE density, compressional-wave velocity (using the MST), and thermal conductivity. For split-cores, index properties, such as wet-bulk density, dry-bulk density, water content, porosity, and void ratio, were measured on discrete samples. Compressional-wave velocity (determined using the digital sonic velocimeter [DSV]) and vane shear strength also were measured on split cores. Our methods of analysis are described in the "Explanatory Notes" chapter (this volume).

Two discrete physical property determinations were performed for each split section of the cores from Hole 848B. Cores from Hole 848C were sampled once per section. No shear tests or thermal conductivity determinations were performed on sections from Hole 848C. Index property samples were always taken at the same depth interval as DSV velocity measurements. Here, we describe the downhole distribution of the physical properties from Hole 848B, because each section of the cores from this hole was measured twice, providing the highest resolution profiles of any hole.

Index Properties

Wet-bulk densities range from 1.23 to 1.63 g/cm^3 and generally increase down the core (Fig. 40; Table 20, CD ROM, back pocket). Water content, expressed relative to dry weight (Fig. 41; Table 20, CD ROM, back pocket), varies between 304% and 67% and generally decreases down through the section. Porosity, the volumetric expression of water content, ranges from 64% to 89% (Fig. 42; Table 20, CD ROM, back pocket) and has a downhole profile similar to that of water content. Anomalously low bulk density values (and high water content and porosity values), compared to normal compaction trends, occur in the interval between 20 and 40 mbsf and about 85 mbsf. Grain density (Fig. 43; Table 20, CD ROM, back pocket) is relatively constant down the hole, with a mean value of 2.60 g/cm^3 (range 2.29 to 2.79 g/cm^3), but its variability is greater in the interval between 20 and 40 mbsf and about 85 mbsf.

Compressional-Wave Velocity

Compressional-wave velocities were measured perpendicular to bedding on split cores from Holes 848B and 848C. Compressional-wave velocity values range between 1491 and 1558 m/s and generally increase with depth (Fig. 44; Table 21, CD ROM, back pocket). An offset in velocity of about 30 to 40 m/s occurs at about 50 mbsf.

Shear strength

Shear strength values range between 21 and 294 kPa and increase with depth below seafloor (Fig. 45; Table 22, CD ROM, back pocket). Anomalously low values occur in the upper 10 m and between 20 and 40 mbsf. Very high shear strength values were seen between 85 and 90 mbsf.

Thermal Conductivity

Thermal conductivities were determined routinely for four sections (Sections 1, 3, 5, and 7) from each core to a depth of 93 mbsf. Thermal conductivity values vary between 0.86 and 1.40 W/(m • K), with a mean value of 1.05 W/(m • K) (Fig. 46; Table 23, CD ROM, back pocket). Profiles for thermal conductivity generally mirror those for wet-bulk densities and are inversely related to water content and porosity.

Relationships of Physical Properties to Lithology

The downhole distribution of physical property data at Site 848 is controlled by two factors: gravitational compaction and lithologic variation. Gravitational compaction from increasing overburden

Table 5 (continued).

Event	Hole 848D Interval	Depth (mbsf)	Depth (mcd)
T *N. reinholdii*	1H-CC–2H-CC	8.44–18.28	8.64–20.23
T *N. fossilis*	1H-CC–2H-CC	8.44–18.28	8.64–20.23
T *R. Praebergonii*	2H-CC–3H-CC	18.28–27.81	20.23–30.51
B *P. doliolus*	4H–2–4H-CC	29.9–37.16	32.5–39.76
T *T. convexa*	2H-CC–3H-CC	18.28–27.81	20.23–30.51
T *N. jouseae*			
B *R. praebergonii*	4H-7–4H-CC	37.0–37.16	39.4–39.76
F *T. convexa s.* ampl.			
B *A. elegans*			
T *N. cylindrica*	4H-C–5H-CC	37.16–46.75	39.76–50.75
B *N. jouseae*	4H-CC–5H-CC	37.16–46.75	39.76–50.75
T *N. miocenia.*	6H-CC–7H-CC	56.4–65.07	61.4–71.87
T *N. miocenica* var	6H-CC–7H-CC	56.4–65.07	61.4–71.87
T *T. praeconvexa*			
T *R. praepaleacea*			
B *T. miocenica*			
B *T. convexa* var. *aspinosa*			
B *B. praeconvexa*			
B *N. miocenica*	7H-CC–8H-CC	65.07–75.42	71.87–82.92
T *R. paleacea*	7H-CC–8H-CC	65.07–75.42	71.87–82.92

T = top; B = bottom.

results in a reduction in water content and porosity with depth. Wet-bulk density, shear strength, and thermal conductivity all increase with depth as a result of consolidation. Superimposed on this variation down the hole are changes in lithology from calcareous-rich sediments to silica- or clay-rich sediments.

A comparison of physical properties with lithology reveals that the interval of low wet-bulk density and high water content and porosity between 20 and 40 mbsf consists of interbedded diatom ooze or siliceous-rich sediment. The increased variability noted in the profile of grain density reflects the interbedded nature of the sediments in this interval. Thermal conductivity, a function of porosity, also mirrors the changes in lithology from nannofossil ooze to diatom ooze. The interlocking nature of siliceous microfossil tests results in a more open sediment framework at depth. Thus, porosity tends to be higher (and bulk density lower) in these siliceous-rich sediments.

The highest values for water content and porosity and the lowest values for bulk density occur at a depth of 83.8 mbsf. However, the high values for grain density (2.58 g/cm^3) at this depth suggest that the high water content and low wet-bulk density are not the results of increased siliceous microfossil concentration within these sediments. The visual core descriptions indicated a clay-rich interval at this depth; thus, the high water contents and low wet-bulk densities are probably the result of an increased concentration of clay minerals within this sedimentary interval. High concentrations of clay minerals (especially the smectite group) within sediments result in higher water contents, porosities, and grain densities and lower wet-bulk densities (Holler, 1989). The clay-rich interval at the top of the core has a similar distribution of physical properties.

DOWNHOLE MEASUREMENTS

Because Hole 848B had a short sediment section, logging was limited to the geochemical tool string, mostly through the pipe. Because through-pipe logs need extensive reprocessing, our initial logs provided only limited information to the shipboard party. Elemental yields measured with the tool string through the pipe were altered from measurements in open hole by a variety of physical effects. A neutron emitted by the neutron generator on the GST tool must decrease its initial energy by about nine orders of magnitude, from about 14 MeV to about 0.02 eV, to

Table 6. Corrections of multishot orientations for Site 848 cores.

Core	Azimuthal orientation (0°–360°)	Direction (0°–360°)	Deviation from vertical (°)
[a]138-848B-1H	200		
[a]2H	000		
[a]3H	040		
4H	029	215	1.4
5H	221	230	1.3
6H	227	230	1.2
7H	152	233	1.3
8H	283	217	1.4
[a]9H	190		
10H	195	223	1.5
[a]11H	180		
[a]138-848C-1H	270		
2H	215		
3H	060		
4H	304	214	9.0
5H	298	215	8.4
6H	242	216	8.0
7H	297	217	8.4
8H	303	218	7.9
9H	253	220	7.3
10H	249	221	7.2
[a]138-848D-1H	075		
[a]2H	270		
[a]3H	045		
4H	186	184	1.3
5H	153	185	1.8
6H	120	189	2.0
7H	088	185	2.1
8H	200	176	1.9
9H	194	181	1.9
10H	048	180	2.0

[a]Secondary orientation (SOR) angle is the value used to adjust average measured declination to 0° to 180° for normal or reversed chronozones, respectively, when no multishot orientation was available. For multishot orientation, the measured declination was corrected by adding to it the multishot azimuthal orientation and the local geomagnetic deviation (9.3°).

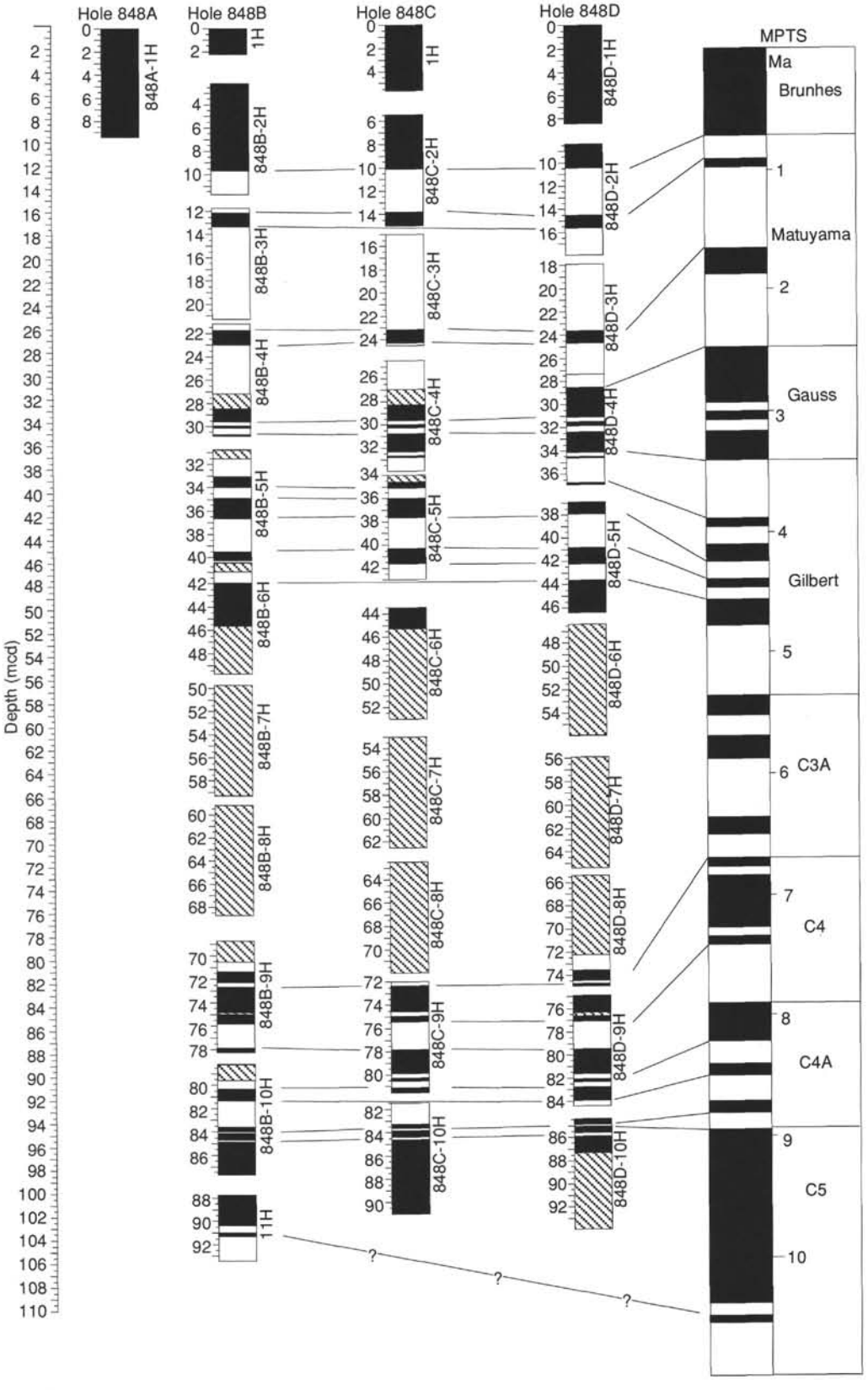

Figure 23. Magnetostratigraphic synthesis at Site 848. Depth marks for individual cores in meters below seafloor (mbsf). Cores are located at appropriate composite depth (mcd). Black zones indicate normal polarity; white zones indicate reverse polarity; hatched zones were not interpreted. MPTS = magnetic polarity time scale.

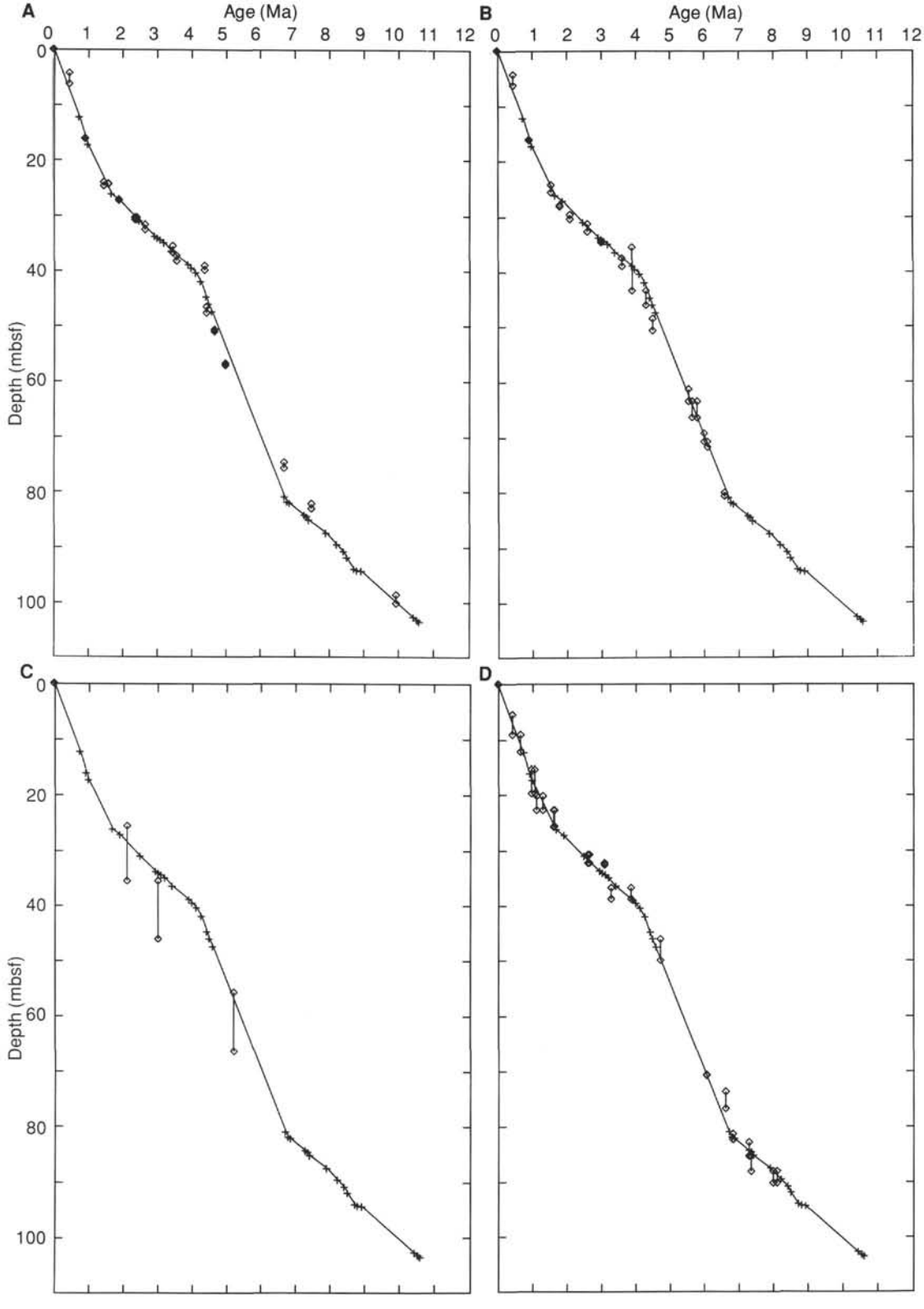

Figure 25. Plot of age vs. depth for Site 848, based on magnetostratigraphic calibration points in Table 9. The paleomagnetic control points are shown as crosses. **A.** Nannofossil datums. **B.** Diatom datums. **C.** Radiolarian datums. **D.** Foraminifer datums. For each datum, the upper and lower depth bounds within which the datum occurs have been joined by a line.

Table 7. Reversal boundary depths from Site 848.

Core, section, interval (cm)	Depth (mbsf)	Depth (mcd)	Interpretation	Age (Ma)	Comments
138-848B-2H-6, 4	9.74	12.54	Brunhes/Matuyama	0.73	Near section break
3H-1, 40	12.10	16.05	Jaramillo (t)	0.91	
3H-2, 15	13.35	17.30	Jaramillo (o)	0.98	
4H-1, 25	21.45	25.80	Olduvai (t)	1.66	Near core top (?)
4H-2, 30	23.00	27.35	Olduvai (o)	1.88	
4H-6, 90	29.60	33.95	Kaena (t)	2.92	
4H-6, 125	29.95	34.30	Kaena (o)	2.99	
4H-6, 145	30.15	34.50	Mammoth (t)	3.08	Near section break
4H-7, 55	30.75	35.10	Mammoth (o)	3.18	
5H-2, 85	33.05	38.70	Cochiti (t)	3.88	
5H-3, 25	33.95	39.60	Cochiti (o)	3.97	
5H-3, 120	34.90	40.55	Nunivak (t)	4.10	
5H-4, 145	36.65	42.30	Nunivak (o)	4.24	Near section break
5H-6, 130	39.50	45.15	Sidufjall (t)	4.40	
6H-2, 20	41.90	47.60	Thvera (t)	4.47	
9H-2, 125	71.45	81.05	C4-n1 (t)	6.70	
9H-3, 70	72.40	82.00	C4-n1 (o)	6.78	
9H-3, 95	72.65	82.25	C4-n2 (t)	6.85	
9H-3, 10	74.80	84.40	C4-n2 (o)(?)	7.28	
9H-3, 30	75.00	84.60	C4-n3 (t)(?)	7.35	
9H-5, 100	75.70	85.30	C4-n3 (o)	7.41	
9H-7, 15	77.85	87.45	C4A-n1 (t)	7.90	
10H-2, 65	80.35	90.95	C4A-n2 (t)	8.41	
10H-3, 15	81.35	91.95	C4A-n2 (o)	8.50	
10H-4, 90	83.60	94.20	C4A-n3 (t)	8.71	
10H-4, 130	84.00	94.60	C4A-n3 (o)	8.80	
10H-4, 145	84.15	94.75	C5-n1 (t)	8.92	Near section break
10H-5, 45	84.65	95.25	R -> N		
10H-5, 65	84.85	95.45	N -> R		
11H-2, 125	90.45	102.80	C5-n1 (o)(?)	10.42	Poorly defined
11H-3, 30	91.00	103.35	C5-n2 (t)(?)	10.54	Poorly defined
11H-3, 60	91.30	103.65	C5-n2 (o)(?)	10.59	Poorly defined
138-848C-2H-4, 10	10.10	12.35	Brunhes/Matuyama	0.73	Near section break
2H-6, 80	13.80	16.05	Jaramillo (t)	0.91	
3H-6, 70	23.20	26.20	Olduvai (t)	1.66	
3H-7, 30	24.30	27.30	Olduvai (o)	1.88	
4H-4, 65	29.65	33.90	Kaena (t)	2.92	
4H-4, 100	30.00	34.25	Kaena (o)	2.99	
4H-4, 125	30.25	34.50	Mammoth (t)	3.08	
4H-5, 30	30.80	35.05	Mammoth (o)	3.18	
4H-6, 30	32.30	36.55	Gauss/Gilbert	3.40	
4H-6, 70	32.70	36.95	N -> R		
4H-6, 80	32.80	37.05	R -> N		
5H-1, 110	35.10	39.65	Cochiti (o)	3.97	
5H-2, 50	36.00	40.55	Nunivak (t)	4.10	
5H-3, 65	37.65	42.20	Nunivak (o)	4.24	
5H-5, 35	40.35	44.90	Sidufjall (t)	4.40	
5H-6, 10	41.60	46.15	Sidufjall (t)	4.47	Near section break
9H-1, 35	72.35		C4-n2 (t)(?)	6.85	Near core top
9H-2, 105	74.55	84.35	C4-n2 (o)(?)	7.28	
9H-2, 150	75.00	84.80	C4-n3 (t)(?)	7.35	Near section break
9H-3, 45	75.45	85.25	C4-n3 (o)(?)	7.41	
9H-4, 130	77.80	87.60	C4A-n1 (t)	7.90	
9H-6, 35	79.85	89.65	C4A-n1 (o)	8.21	
9H-6, 85	80.35	90.15	N -> R		
9H-6, 105	80.55	90.35	R -> N		
9H-7, 10	81.10	90.90	C4A-n2 (t)	8.41	Near section break
10H-2, 30	83.30	94.05	C4A-n3 (t)	8.71	
10H-2, 65	83.65	94.40	C4A-n3 (o)	8.80	
10H-2, 85	83.85	94.60	C5-n1 (t)	8.92	
10H-2, 140	84.40	95.15	R -> N		
10H-3, 10	84.60	95.35	N -> R		Near section break
138-848D-2H-2, 55	10.45	12.40	Brunhes/Matuyama	0.73	
2H-5, 10	14.50	16.45	Jaramillo (t)	0.91	Near section break
2H-5, 120	15.60	17.55	Jaramillo (o)	0.98	
3H-4, 125	23.65	26.35	Olduvai (t)	1.66	
3H-5, 80	24.70	27.40	Olduvai (o)	1.88	
4H-1, 115	28.55	31.15	Matuyama/Gauss (?)	2.47	
4H-3, 75	31.15	33.75	Kaena (t)	2.92	
4H-3, 110	31.50	34.10	Kaena (o)	2.99	
4H-3, 145	31.85	34.45	Mammoth (t)	3.08	
4H-4, 50	32.40	35.00	Mammoth (o)	3.18	
4H-5, 70	34.10	36.70	Gauss/Gilbert	3.40	
4H-7, 35	36.74	39.34	Cochiti (t)	3.88	
5H-1, 100	37.90	41.90	Nunivak (o)	4.24	

Table 7 (continued).

Core, section, interval (cm)	Depth (mbsf)	Depth (mcd)	Interpretation	Age (Ma)	Comments
5H-3, 90	40.80	44.80	Sidufjall (t)	4.40	
5H-4, 80	42.20	46.20	Sidufjall (o)	4.47	
5H-5, 75	43.65	47.65	Thvera (t)	4.57	
8H-6, 65	73.55	81.05	C4-n1 (t)	6.70	
8H-7, 5	74.45	81.95	C4-n1 (o)	6.78	Near section break
8H-7, 35	74.75	82.25	C4-n2 (t)	6.85	
9H-2, 75	77.15	85.35	C4-n3 (o)(?)	7.41	
9H-4, 10	79.50	87.70	C4A-n1 (t)	7.90	Near section break
9H-5, 70	81.60	89.80	C4A-n1 (o)	8.21	
9H-5, 115	82.05	90.25	N -> R		
9H-5, 140	82.30	90.50	R -> N		Near section break
9H-6, 40	82.80	91.00	C4A-n2 (t)	8.41	
9H-7, 0	83.90	92.10	C4A-n2 (o)	8.50	Near section break
10H-1, 50	84.90	94.20	C4A-n3 (o)	8.80	
10H-1, 70	85.10	94.40	C5-n1 (t)	8.92	
10H-1, 125	85.65	94.95	R -> N		
10H-2, 0	85.90	95.20	N -> R		Near section break

t = top; o = onset.

be absorbed by an atom. Neutrons lose energy through inelastic collisions, and hydrogen, because of its size, is most effective for neutron energy loss. Water thus is a good neutron moderator. After a neutron has been absorbed by an atom, the new isotope emits a gamma ray to stabilize its energy. These characteristic gamma rays are measured by the geochemical spectral tool (GST). Replacing borehole water with an iron pipe removes part of the water's moderating effect and extends the mean distance that a neutron can travel before absorption. Gamma-ray count rates decrease by simple square law distance effects. The iron pipe also effectively scatters gamma rays, so that the gamma-ray signal coming back from the formation is attenuated by the pipe. This latter process affects all of the geochemical logs, including the aluminum clay tool (ACT) and the natural gamma-ray tool (NGT). The effects of the pipe are not all negative, however. Displacement of

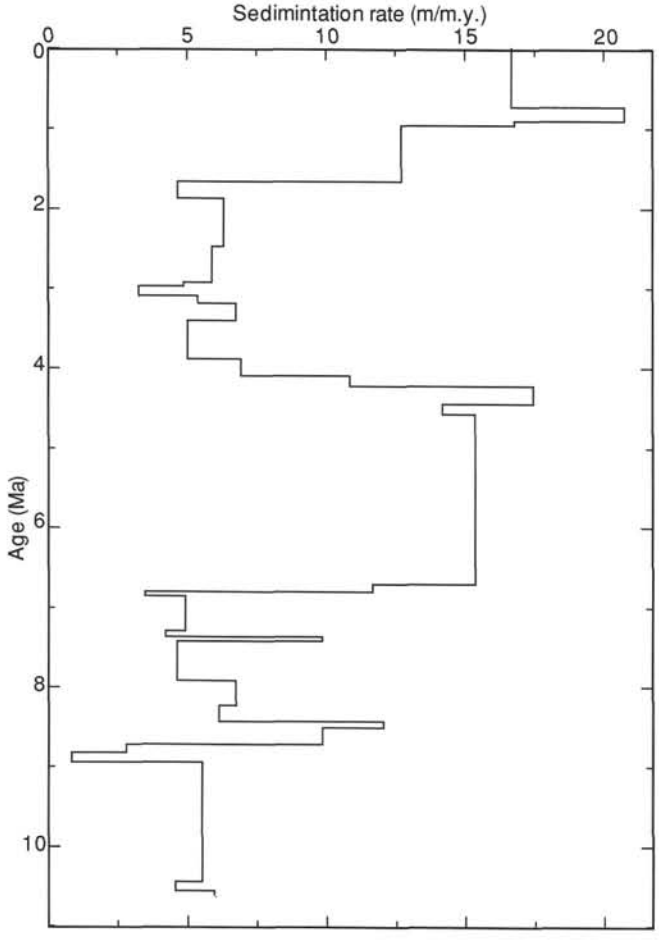

Figure 26. Linear sedimentation rate vs. age, based on data in Table 9.

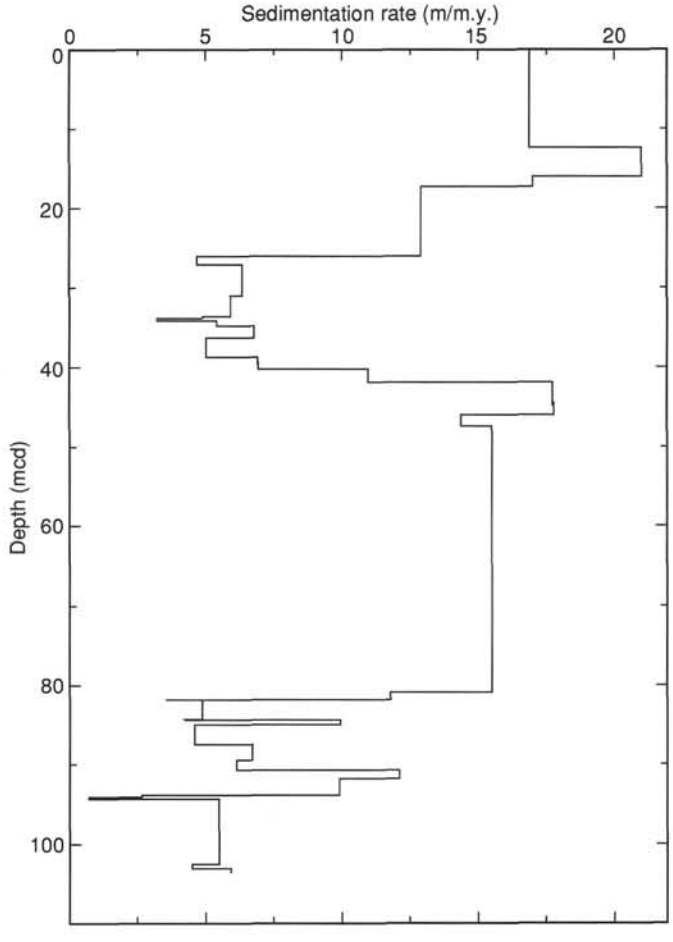

Figure 27. Linear sedimentation rate vs. composite depth, based on data in Table 9.

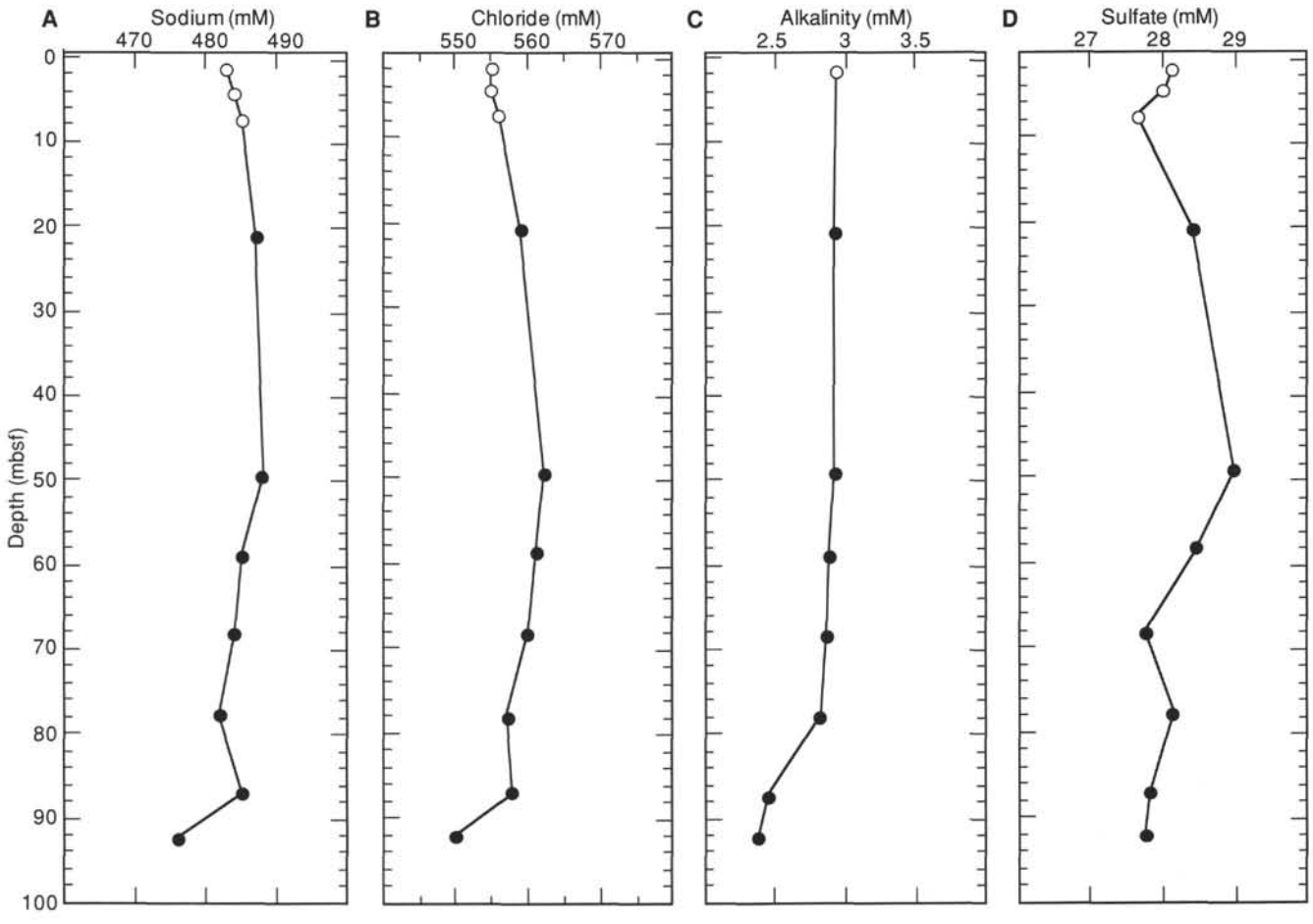

Figure 28. Interstitial-water geochemical data vs. depths (mbsf) for Holes 848A (open circles) and 848B (closed circles). **A.** Sodium. **B.** Chloride. **C.** Alkalinity. **D.** Sulfate.

water by the pipe can actually raise the relative elemental yields of some of the rock-forming elements, such as Si. When one inspects the data, one can see that the Ca-yield has been least affected by the pipe and may be the easiest data to reprocess.

Many features in the logs have been caused by changes in the bottomhole assembly (BHA) configuration. A good example of this is shown in the Fe logging data (Fig. 47). In this plot, the Fe-yield is shown for Site 848 and compared to the equivalent sections through the pipe in Sites 846 and 847. The Fe signal is dominated by the different thicknesses and material of the BHA, and the corrections that must be applied to obtain the sedimentary Fe values are large. Pipe effects are not limited to Fe alone, as explained above, and will affect yields for the other elements.

Reprocessing of through-pipe geochemical data is a formidable job, but with effort it can yield good continuous geochemical profiles. For example, ODP Site 765 through-pipe geochemical logs and independently measured sedimentary geochemical profiles compared well (Plank and Ludden, 1991). At the present time, no one has tried to compare Milankovitch-scale geochemical variations through-pipe logs with core data. The data sets we generated here and at earlier holes during this leg will allow us to evaluate whether these data retain this high-frequency information after reprocessing.

After initial examination, data from Hole 848B appears to retain similar periodic information as the cores. Shown in Figure 48 are the Ca-yield and a composite smoothed GRAPE density profile (see "Sedimentation Rates" section, this chapter), which varies with calcite content. Each curve has been plotted on its own respective depth scale and stretched so that the bottom of the hole is at the right end of the graph. Both curves have major variance at scales of 1.5- to 2-m periodicity, and the general shape of the curves agrees to about 60 mbsf. Below 60 mbsf, the two curves diverge. We assumed that this was a BHA effect on the raw data, but this conclusion will be evaluated during reprocessing.

Quality of Data

The GST calibration at the base of the hole has left artifacts in the natural gamma-ray activity and aluminum profiles. During GST calibration, the tool string was moved slowly up the hole. Normally, moving a tool string minimizes data artifacts in logging profiles. During calibration, the ^{252}Cf source in the ACT passed a section of hole from 83.2 to 63.2 mbsf. A slight pause occurred at 63.2 mbsf when the tool string was stopped and then lowered back to total depth. The ACT source was moving slowly enough to activate the formation during the calibration pass, especially since the formation was apparently high in Mn. Spikes appear in the natural gamma-ray and aluminum records at 63.2 mbsf, and a broad high in natural gamma-ray activity induced by the calibration between 70.5 and 73.5 mbsf was negatively correlated with aluminum contents (Fig. 49).

This negative correlation between natural gamma-ray activity and aluminum caused us to suspect that high Mn contents might be found in the interval between 70.5 and 73.5 mbsf. The activated Mn should increase the measured background natural gamma-ray activity and should lower net aluminum counts, because the net counts were obtained by subtracting the activity in this energy window before (measured in the NGT) from after when the ^{252}Cf source has passed (measured in the ACT).

Natural gamma-ray counts remained high from 70.5 mbsf to the deepest NGT recording, at 76.9 mbsf. We consider that this entire

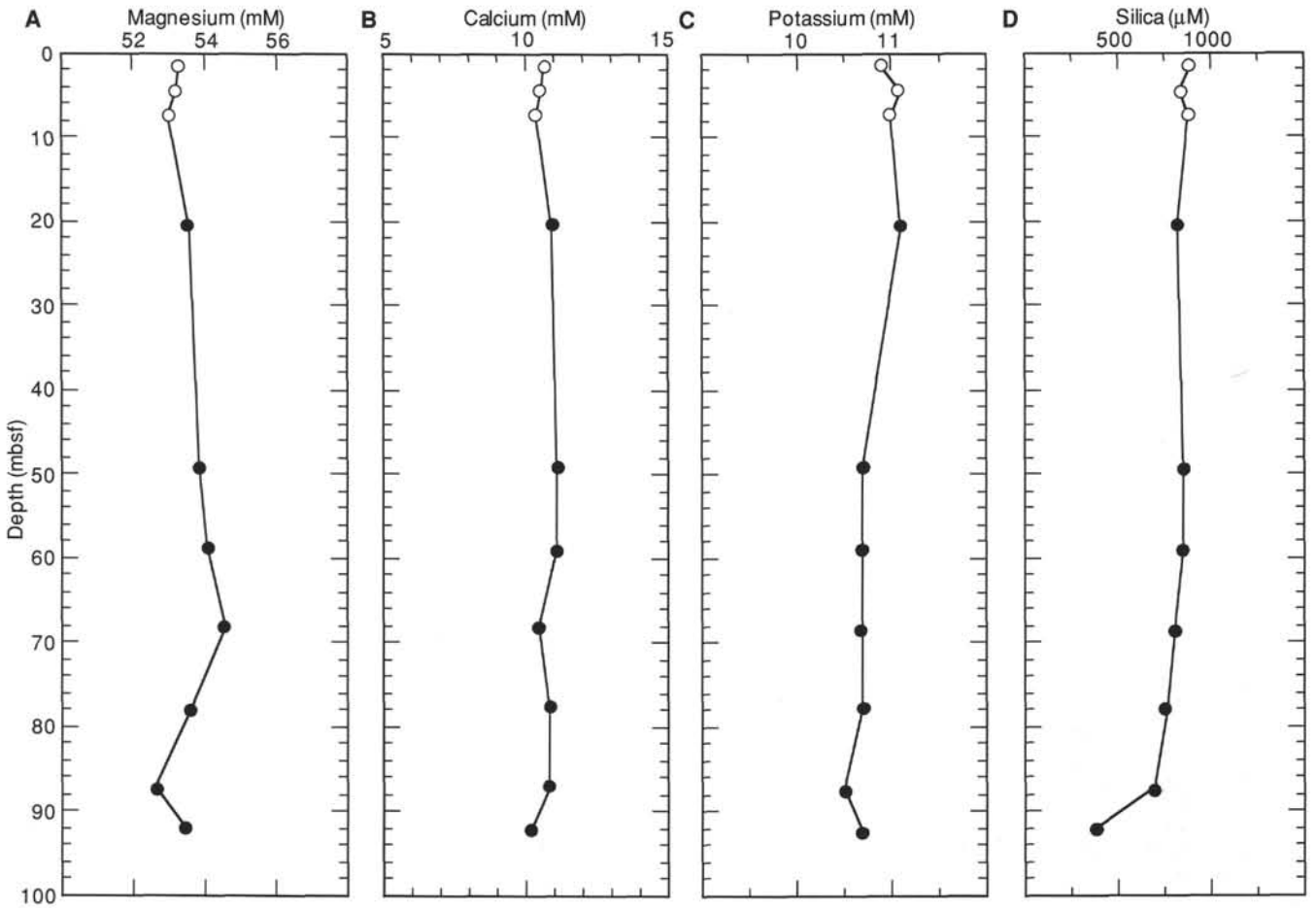

Figure 29. Interstitial-water geochemical data vs. depths (mbsf) for Holes 848A (open circles) and 848B (closed circles). **A.** Magnesium. **B.** Calcium. **C.** Potassium. **D.** Silica.

lower section contains high Mn contents. Some evidence for this can be seen in the correlation between the interval of high induced "natural" gamma-ray activity and high magnetic susceptibility measured in the hole (Fig. 50). High magnetic susceptibility marks the interval of Fe- and Mn-rich metalliferous sediments.

SEISMIC STRATIGRAPHY

Modeling Procedure

Synthetic seismograms were generated from velocity and density models for Site 848 to correlate reflectors in the seismic section to stratigraphic changes.

Because of the thin sediment cover at this site, no downhole density logging was conducted. A density model was created by using laboratory densities only. Over the interval from 0 to 87.1 mbsf, a 10-point boxcar filtered GRAPE density from Hole 848B was used, with bad data points (from core disturbance) in the intervals from 2.0 to 2.4 mbsf and 78.3 to 78.4 mbsf removed. Beyond 87.1 mbsf, laboratory wet-bulk densities were used.

A velocity model was created using only laboratory velocity that had been collected with the DSV. Velocity was corrected to *in-situ* conditions for changes of sound speed as a function of temperature and pressure, assuming a temperature gradient of 40.9°C/km and a bottom-water temperature of 1.56°C determined from the temperature log.

We evaluated the accuracy of our conversion of traveltime to depth by generating synthetic seismograms and subsequently comparing them with the seismic record collected over the site. Synthetic seismograms were generated using the above merged velocity and density data. These data were resampled at a 1-ms sample interval (approximately 60 cm) and then used to calculate acoustic impedance and reflection coefficients and, finally, a synthetic seismogram. Density and velocity values typical of basalt (2.5 g/cm^3 and 3000 m/s, respectively) were added at the basement depth (93.3 mbsf) to generate a basement reflector in our synthetic seismogram. The model we used to generate the synthetic seismogram has the same assumptions as before and is described in Mayer et al. (1985). A final synthetic seismogram was filtered from 70 to 250 Hz, the same filter parameters as the field record collected during the Site 848 site survey.

Results

A comparison of our synthetic seismogram with the seismic profile collected at Site 848 shows a very good match between the two (Fig. 51). A nearly one-to-one correspondence exists between reflectors, with an excellent match at the basement. This suggests that our traveltime-to-depth conversion was fairly accurate.

Given an acceptable velocity model, the origin of some of the reflectors at Site 844 can be analyzed. We emphasize that these are preliminary results that undoubtedly will be modified after more careful analysis. We identified 11 major reflectors or reflector packages. These reflectors were selected on the basis of amplitude and lateral coherency in the seismic record in the immediate area of Site 848. We measured two-way traveltime in the synthetic seismogram of the top and bottom of each reflector, and by using the assumed velocity model, we determined the depth range of each reflector.

With each major reflector, an associated change in acoustic impedance takes place. As at previous sites, we compared the velocity, density, and acoustic impedance models to depth ranges calculated

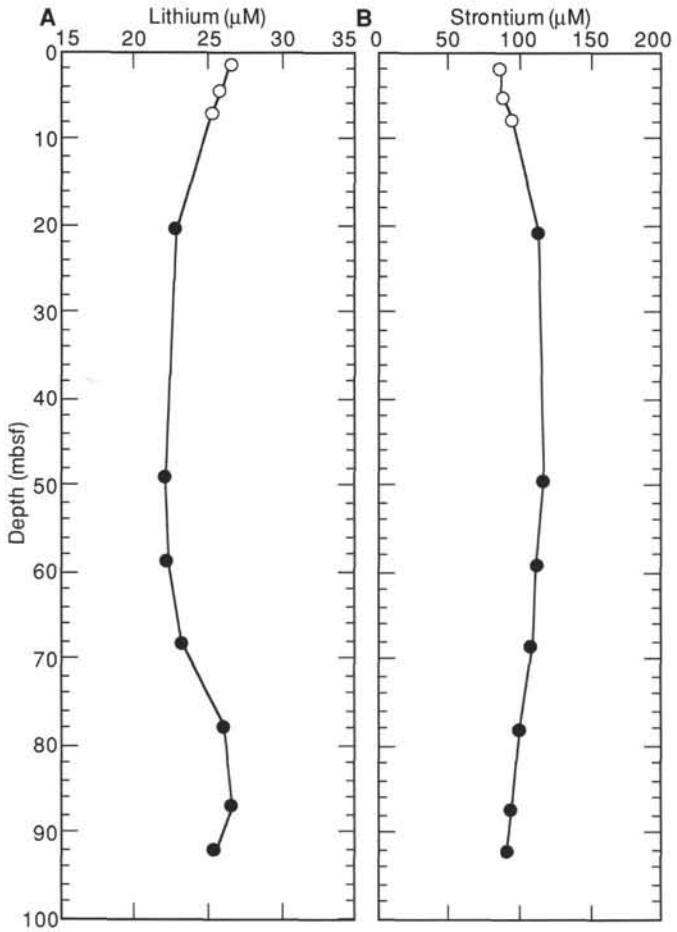

Figure 30. Interstitial-water geochemical data vs. depths (mbsf) for Holes 848A (open circles) and 848B (closed circles). **A.** Lithium. **B.** Strontium.

from the traveltime to determine any changes in physical properties causing the selected seismic reflectors.

In general, a large change in density can be directly associated with each reflector (Fig. 52), because little variation of velocity occurs with depth. The only exception, perhaps, is Reflector 7, where an increase in density occurs slightly deeper down the hole (less than 1 m) than the depth determined from the synthetic seismogram. The depths (synthetic, mbsf, and mcd) and ages (based on magnetostratigraphy and biostratigraphy of Site 848; see "Sedimentation Rates" section, this chapter) of these reflectors are presented in Table 24. A detailed understanding of the lithologic, biostratigraphic, and, ultimately, the paleoceanographic significance of these events must await shore-based studies at this time.

SUMMARY AND CONCLUSIONS

Site 848 is the southernmost site of the western transect of Leg 138. This transect, situated along 110°W, was designed to sample the various elements of the equatorial circulation system in an area far removed from the influence of the eastern boundary of the Pacific Ocean. The transect also serves as the eastern end-member of a series of studies (Legs 85 and 130) aimed at understanding the regional and global responses of the equatorial Pacific Ocean to changes in climate. The proximity of the site to the East Pacific Rise as well as its position south of the equator (it has

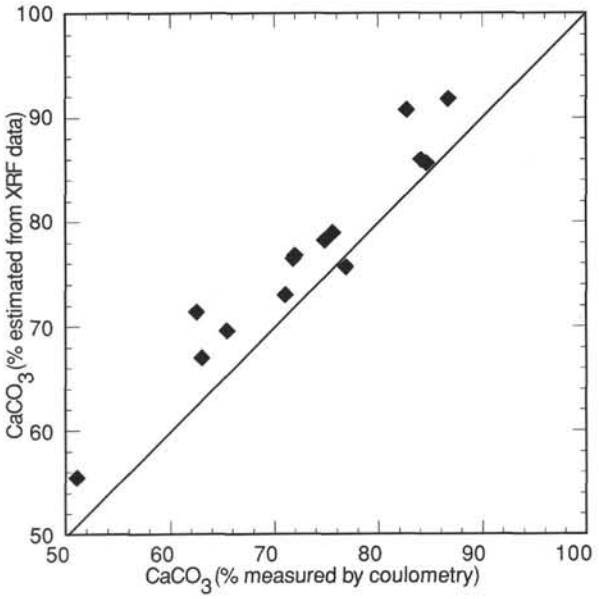

Figure 31. Concentrations of $CaCO_3$ estimated from XRF CaO concentrations vs. $CaCO_3$ measured by coulometry.

Table 8. Top and bottom depths of each core in Site 848 in the composite depth section.

Core no.	ODP depth (mbsf)	Core length (m)	Composite depth (mcd)	Δ (m)
138-848A-1H	0–9.54	9.54	0.20–9.74	0.20
-848B-1H	0–2.23	2.23	0.20–2.43	0.20
2H	2.20–12.27	10.07	5.00–15.07	2.80
3H	11.70–21.73	10.03	15.65–25.68	3.95
4H	21.20–31.17	9.97	25.55–35.52	4.35
5H	30.70–40.53	9.83	36.35–46.18	5.65
6H	40.20–50.17	9.97	45.90–55.87	5.70
7H	49.70–59.77	10.07	56.40–66.47	6.70
8H	59.20–69.32	10.12	66.65–76.77	7.45
9H	68.70–78.58	9.88	78.30–88.18	9.60
10H	78.20–88.16	9.96	88.80–98.76	10.60
11H	87.70–93.37	5.67	100.05–105.72	12.35
12X	93.30–93.30	0.00	105.65–105.65	12.35
-848C-1H	0–5.47	5.47	0–5.47	0.00
2H	5.50–15.45	9.95	7.75–17.70	2.25
3H	15.00–25.06	10.06	18.00–28.06	3.00
4H	24.50–34.57	10.07	28.75–38.82	4.25
5H	34.00–43.40	9.40	38.55–47.95	4.55
6H	43.50–53.53	10.03	49.85–59.88	6.35
7H	53.00–63.06	10.06	60.75–70.81	7.75
8H	62.50–72.31	9.81	71.60–81.41	9.10
9H	72.00–82.00	10.00	81.80–91.80	9.80
10H	81.50–91.37	9.87	92.25–102.12	10.75
11X	1.00–94.02	3.02	101.75–104.77	10.75
-848D-1H	0–8.44	8.44	0.20–8.64	0.20
2H	8.40–18.28	9.88	10.35–20.23	1.95
3H	17.90–27.81	9.91	20.60–30.51	2.70
4H	27.40–37.16	9.76	30.00–39.76	2.60
5H	36.90–46.75	9.85	40.90–50.75	4.00
6H	46.40–56.40	10.00	51.40–61.40	5.00
7H	55.90–65.07	9.17	62.70–71.87	6.80
8H	65.40–75.42	10.02	72.90–82.92	7.50
9H	74.90–84.78	9.88	83.10–92.98	8.20
10H	84.40–94.37	9.97	93.70–103.67	9.30

Note: See text for details.

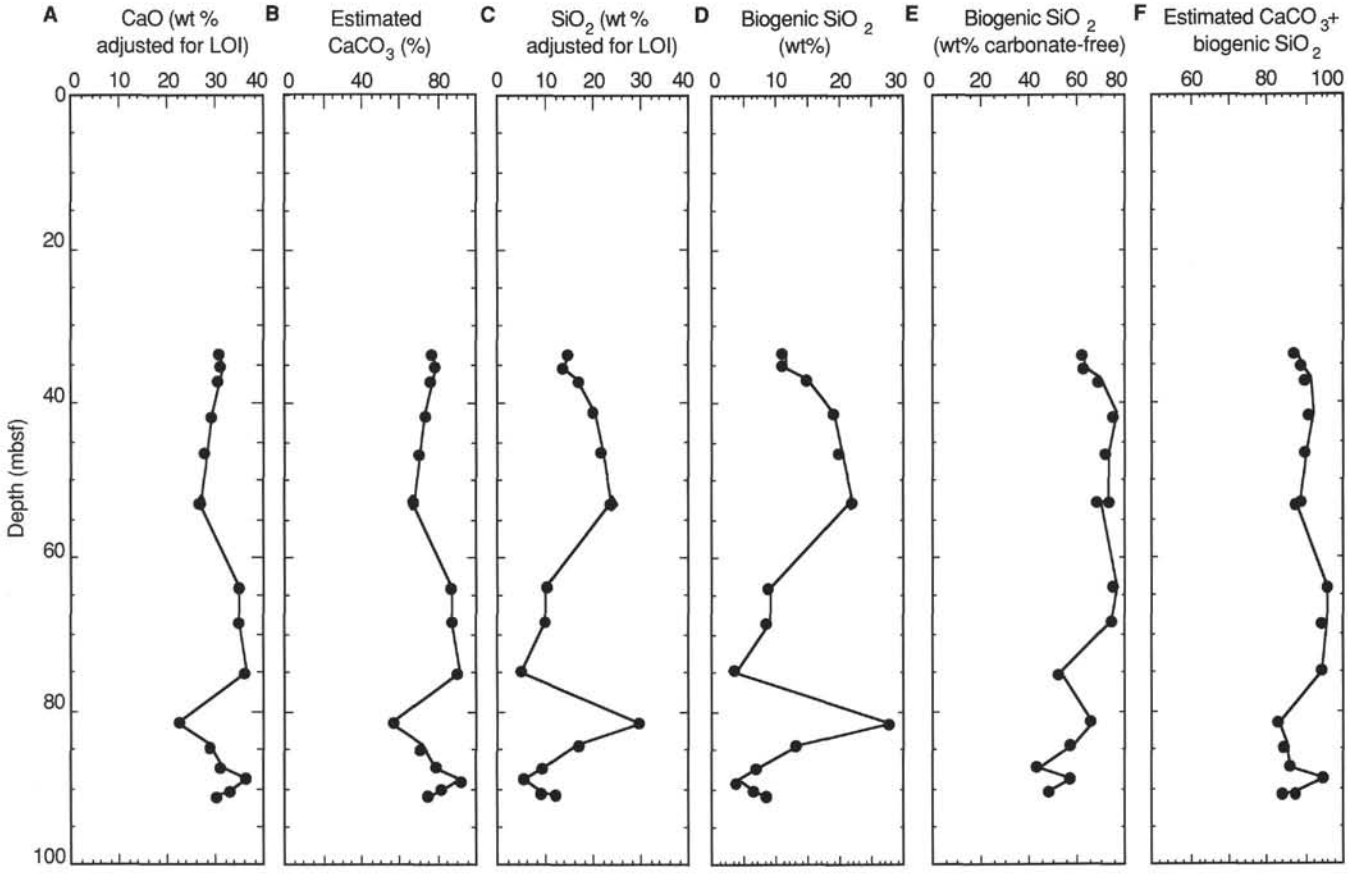

Figure 32. **A.** Weight percent CaO, adjusted for loss on ignition. **B.** Estimated concentration of $CaCO_3$ calculated from XRF data, assuming that loss on ignition was primarily the result of loss of CO_2 from $CaCO_3$. **C.** Weight percent SiO_2, adjusted for loss on ignition. **D.** Estimated concentration of biogenic SiO_2, assuming a terrigenous SiO_2/Al_2O_3 value of 3.0. **E.** Weight percent biogenic SiO_2, calculated on a calcium carbonate-free basis. **F.** Percentage of biogenic components (= estimated wt% $CaCO_3$ + estimated wt% biogenic SiO_2).

not yet crossed through the zone of highest equatorial productivity) have resulted in a relatively thin (94 m) sedimentary section. Nonetheless, continuous core logs (GRAPE, susceptibility, and color reflectance) and overlapping APC cores assured the complete recovery of an approximately 10.5-Ma depositional record.

Site 848 is located about 650 km west of the East Pacific Rise on crust generated about 10 to 11 Ma. The backtracked path (Table 25) of the site is straightforward and constrained by the movement of the Pacific Plate, which can be reconstructed from the numerous hot-spot traces of the Pacific Ocean and from sediment distribution in the equatorial region (van Andel et al., 1975; see Fig. 2 in "Background and Scientific Objectives" section, this chapter). From an original ridge-crest depth of approximately 2700 m, the site has subsided to its present depth of 3866 m and in doing so has intercepted a regionally and temporally variable CCD and lysocline.

The paleomagnetic results from Site 848 represent a significant addition to the stratigraphic framework required for any high-resolution paleoceanographic studies planned from Leg 138 drill sites. Although the paleomagnetic signal at Site 848 was variable; polarity reversals are resolvable in the upper 47 mbsf (0–4.7 Ma) and in the interval from 72 mbsf to the basement (6.8–10.5 Ma). The upper zone contains every major polarity chronozone and subchronozone between the Brunhes and the Thvera. At these low latitudes, polarity reversals were primarily identified by declination patterns. The success of the multishot tool for providing core orientation is directly responsible for producing this extremely rare, deep-ocean, equatorial Pacific Ocean magnetic reversal record. The magnetic susceptibility record once again proved to be valuable as an interhole correlation tool. The strength of both the magnetic susceptibility and remanence intensity may be inversely correlated to both sedimentation rate and carbonate content, suggesting that the recovery of the paleomagnetic record may be the result of increased carbonate dissolution that has concentrated clay minerals.

The high quality of our magnetic data provided excellent resolution of changes in sedimentation rate at this site, which will greatly help in resolving the sedimentation history of this region. We use these data to present a summary of the long-term changes in sediments recorded at Site 848.

The first sediment to accumulate above the newly formed Site 848 was a nannofossil ooze that contained a substantial component of iron-oxides and clays. Sedimentation rates during this time (10.6–8.9 Ma) were very low (4–6 m/m.y., Fig. 53A), and, in general, both susceptibility and density values were high (Figs. 53B and 53C). The presence of oxides was clearly and quantitatively indicated by distinctive peaks in the percentage of red reflectance curves produced by the color scanner. While the presence of metalliferous sediments is related to ridge-crest hydrothermal activity, the relative percentage of the metalliferous component is variable; the sediment immediately overlying basement has a smaller percentage of metalliferous sediment than that above it. These variations may be related to dilution by carbonate and, thus, the section in the interval from 10.6 to approximately 8.8 Ma presents a record of increasing dissolution that is probably related to both the deepening of the site as it moved away from the ridge crest and the regional behavior of the CCD. At each of the Leg 138 sites, as well as at numerous other sites in the Pacific Ocean, this period of time may have been one of enhanced dissolution (Theyer et al., 1989). Carbonate deposition (Fig. 53D) and sedimentation rates (Fig. 53) reached a minimum at about 8.8

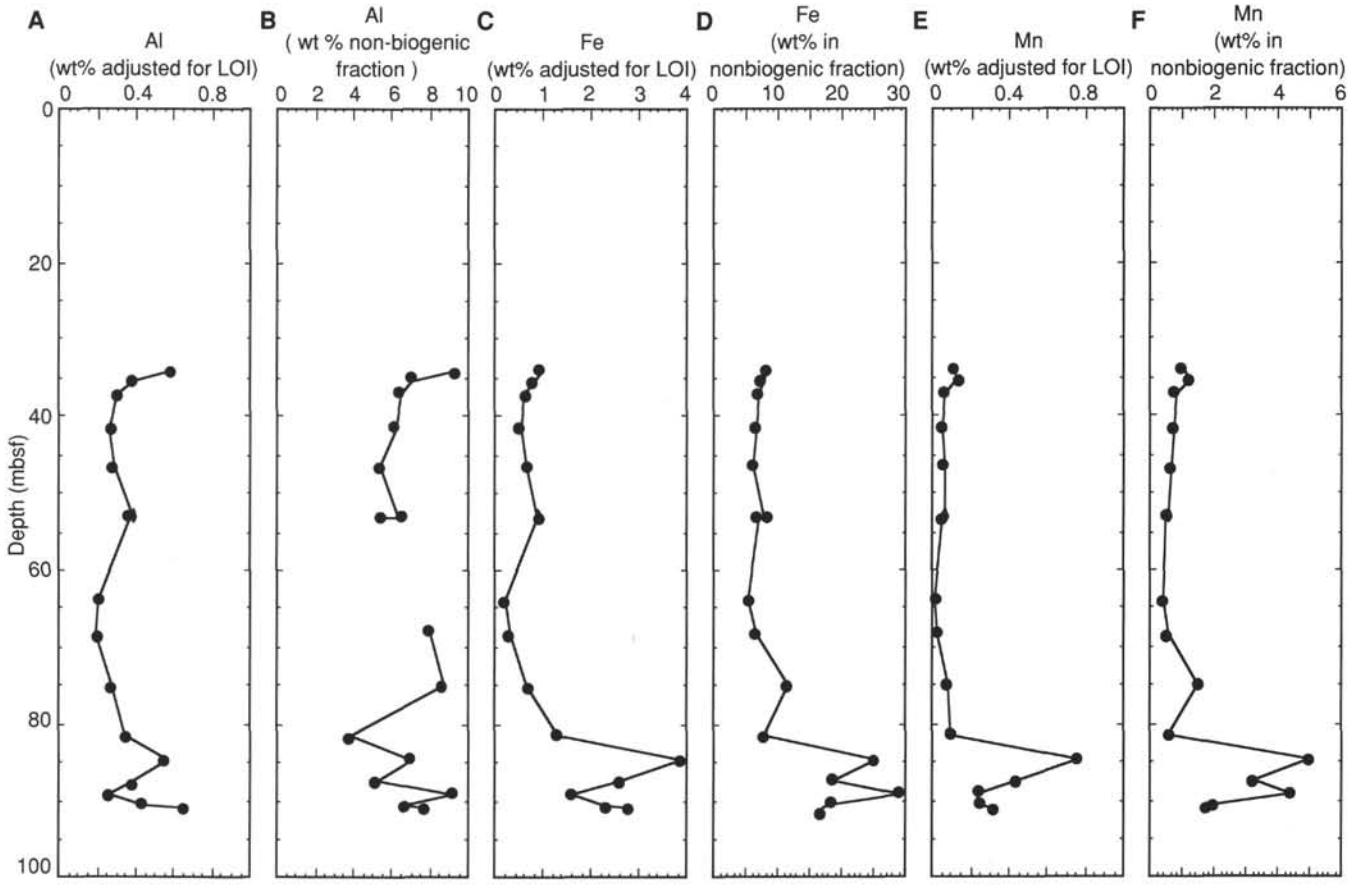

Figure 33. **A.** Weight percent Al, adjusted for loss on ignition. **B.** Weight percent Al in the nonbiogenic sediment fraction. **C.** Weight percent Fe, adjusted for loss on ignition. **D.** Weight percent Fe in the nonbiogenic sediment fraction. **E.** Weight percent Mn, adjusted for loss on ignition. **F.** Weight percent Mn in the nonbiogenic sediment fraction.

Ma, as did the accumulation rates of the noncarbonate components. This interval is represented in the sediment column as a small (less than 2 m thick) layer of hydrous clays. Interstitial-water profiles of sodium, chloride, alkalinity, magnesium, potassium, and silica in the oxide-rich interval show evidence for the effects of alteration of basalt.

The carbonate minimum at about 8.8 Ma was followed by a short (approximately 500 k.y.) interval of higher (10–12 m/m.y.) sedimentation and accumulation rates that produced high percentages of carbonate in nannofossil oozes (Fig. 53D). Following this brief increase was an extended period (8.3–6.8 Ma) of low sedimentation rates (4–6 m/m.y.) having reduced, but still high, carbonate contents (Fig. 53D). From 6.8 to 4 Ma, sedimentation rates increased (17 m/m.y.), as did accumulation rates of carbonates and noncarbonates. High-frequency variations in carbonate content dominate the record as the relative proportions of carbonate and silica vary in response to changes in both deep and surface oceanographic conditions. Sedimentation and accumulation rates once again decreased during the interval from 4 to 1.7 Ma; this decrease in accumulation rate was expressed as a slight decrease in carbonate content. The Pleistocene is characterized by the highest sedimentation rates of the section (as high as 20 m/m.y.) and a concomitant increase in carbonate content.

While sedimentation rates at Site 848 are low relative to other sites drilled along the 110°W transect, the detailed paleomagnetic record combined with high-resolution sediment properties will help to provide a magnetic benchmark for intersite correlation. Figure 54 illustrates the quality of these data. We plotted (vs. composite depth) a spliced GRAPE density record along with paleomagnetic stratigraphy. This spliced record was constructed by selecting from each of the four holes drilled the core that contained the most representative GRAPE record within any depth interval. In Figure 54 we show the smoothed GRAPE record (smoothing was done using a nine-point Gaussian filter); thus, we removed some of the higher-frequency variability. While this site has relatively low sedimentation rates, the section contains a large amount of signal at frequencies similar to that of orbital forcing. As demonstrated in Figure 24 (back-pocket figure), this signal is highly reproducible within the separate holes drilled at Site 848. The correlation of this signal with those of other sites along the rest of the 110°W transect will make Site 848 an invaluable "golden spike" for the stratigraphic framework of Leg 138.

REFERENCES

Burckle, L. M., and McLaughlin, R. B., 1977. Size changes in the marine diatom *Coscinodiscus nodulifer* A. Schmidt in the equatorial Pacific. *Micropaleontology,* 23:216–222.

Elderfield, H., and Gieskes, J. M., 1982. Sr isotopes in interstitial waters of marine sediments from Deep Sea Drilling Project cores. *Nature,* 333:493–497.

Gieskes, J. M., Elderfield, H., and Palmer, M. R., 1986. Strontium and its isotopic composition in interstitial waters of marine carbonate sediments. *Earth Planet. Sci. Lett.,* 77:229–235.

Gieskes, J. M., and Lawrence, J. R., 1981. Alteration of volcanic matter in deep-sea sediments: evidence from the chemical composition of interstitial waters from deep-sea drilling cores. *Geochim. Cosmochim. Acta,* 45:1687–1703.

Heath, G. R., and Dymond, J., 1977. Genesis and transformation of metalliferous sediments from the East Pacific Rise, Bauer Deep and Central Basin, Northwest Nazca Plate. *Geol. Soc. Am. Bull.,* 88:723–733.

Holler, P., 1989. Mass physical properties of sediments from Bransfield Strait and northern Weddell Sea. *Mar. Geotechnol.,* 8:1–18.

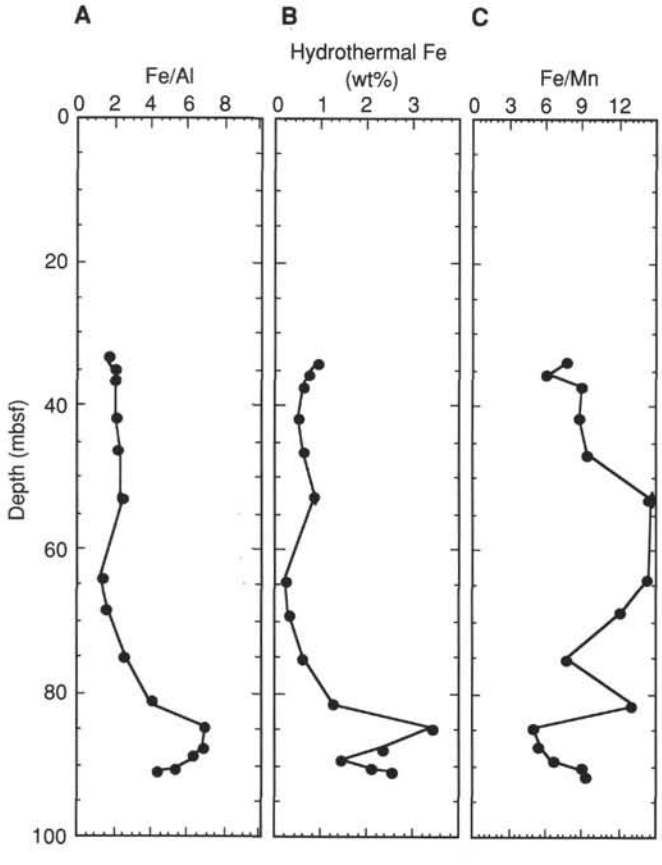

Figure 34. **A.** Fe/Al ratio. **B.** Weight percent hydrothermal Fe, calculated by assuming that all Fe is either terrigenous or hydrothermal and that the Fe/Al ratio of terrigenous sediment is 0.6. **C.** Fe/Mn ratio.

Table 9. Control points for accumulation rates.

Depth (mcd)	Sediment rate (m/m.y.)	Age (Ma)	Top sedimentary section
0		0	
12.45	17.05	0.73	Brunhes (o)
16.2	20.83	0.91	Jaramillo (t)
17.45	17.86	0.98	Jaramillo (o)
26.3	13.01	1.66	Olduvai (t)
27.35	4.77	1.88	Olduvai (o)
31.15	6.44	2.47	Gauss (t)
33.85	6.00	2.92	Kaena (t)
34.2	5.00	2.99	Kaena (o)
34.5	3.33	3.08	Mammoth (t)
35.05	5.50	3.18	Mammoth (o)
36.55	6.82	3.4	Gauss (o)
39.0	5.10	3.88	Cochiti (t)
39.63	7.00	3.97	Cochiti (o)
40.55	7.08	4.1	Nunivak (t)
42.1	11.07	4.24	Nunivak (o)
44.95	17.81	4.40	Sidujfall (t)
46.2	17.86	4.47	Sidujfall (o)
47.65	14.50	4.57	Thvera (t)
81.05	15.68	6.7	C4-n1 (t)
82.0	11.88	6.78	C4-n1 (o)
82.25	3.57	6.85	C4-n2 (t)
84.4	5.00	7.28	C4-n2 (o)
84.7	4.29	7.35	C4-n3 (t)
85.3	10.00	7.41	C4-n3 (o)
87.6	4.69	7.9	C4A-n1 (t)
89.7	6.77	8.21	C4A-n1 (o)
90.95	6.25	8.41	C4A-n2 (t)
92.05	12.22	8.50	C4A-n2 (o)
94.15	10.00	8.71	C4A-n3 (t)
94.4	2.78	8.80	C4A-n3 (o)
94.5	0.83	8.92	C5-n1 (t)
102.8	5.53	10.42	C5-n1 (o)
103.35	4.58	10.54	C5-n2 (t)
103.65	6.00	10.59	C5-n2 (o)

o = onset of event, t = termination of event (from "Paleomagnetism" section, this chapter).

Leinen, M., 1977. A normative calculation technique for determining opal in deep-sea sediments. *Geochim. Cosmochim. Acta,* 41:671–676.

———, 1979. Biogenic silica accumulation in the central equatorial Pacific and its implications for Cenozoic Paleoceanography. *Geol. Soc. Am. Bull.,* 90 (Pt. 2):1310–1376.

Lyle, M., 1986. Major element composition of Leg 92 sediments. *In* Leinen, M., Rea, D. K., et al., *Init. Repts. DSDP,* 92: Washington (U.S. Govt. Printing Office), 355–370.

Mammerickx, J., 1989. The Eastern Pacific Ocean and Hawaii. *In* Winterer, E. L., Hussong, D. H., and Decker, M. (Eds.), *The Geology of North America, Vol. N: The Eastern Pacific Ocean and Hawaii.* Geol. Soc. Am. Bull., Plate 1C.

Martini, E., 1971. Standard Tertiary and Quaternary calcareous nannoplankton zonation. *Proc. 2nd Int. Conf. Planktonic Microfossils, Roma 1970:* Rome (Ed. Tecnoscienza), 739–785.

McDougall, I., Watkins, N. D., Walker, G. P. L., and Kristjansson, L., 1976. Potassium-argon and paleomagnetic analysis of Icelandic lava flows: limits on the age of anomaly 5. *J. Geophys. Res.,* 81:1505–1512.

McDuff, R. E., 1981. Major cation gradients in DSDP interstitial waters: the role of diffusive exchange between seawater and the upper ocean crust. *Geochim. Cosmochim. Acta,* 45:1705–1713.

Okada, H., and Bukry, D. 1980. Supplementary modification and introduction of code numbers to the low-latitude coccolith biostratigraphic zonation (Bukry, 1973; 1975). *Mar. Micropaleontol.,* 5:321–325.

Plank, T., and Ludden, J., 1991. Geochemistry of sediments in the Argo Abyssal Plain at Site 765: a continental Margin reference section for sediment recycling in subduction Zones. *In* Gradstein, F. M., Ludden, J., et al., *Proc. ODP, Sci. Results,* 123: College Station, TX (Ocean Drilling Program), ___–___.

Theyer, F., Vincent, E., and Mayer, L. A., 1989. Sedimentation and paleoceanography of the central equatorial Pacific. *In* Winterer, E. L., Hussong, D. M., and Decker, R. (Eds.), *The Geology of North America, Vol. N: The Eastern Pacific Ocean and Hawaii.* Geol. Soc. Am., 347–372.

van Andel, T. J., Heath, G. R., and Moore, T. C., Jr. 1975. Cenozoic tectonics, sedimentation, and paleoceanography of the central equatorial Pacific. *Geol. Soc. Am. Mem.,* 143:1–134.

Ms 138A-113

NOTE: For all sites drilled, core description forms ("barrel sheets") and core photographs have been reproduced on coated paper and can be found in Section 8, beginning on page 1099. Forms containing smear-slide data can be found in Section 9, beginning on page 1435.

Formation microscanner images for this site are presented on microfiche in the back of Part 2.

Table 10. Interstitial-water geochemical data for Holes 848A and 848B.

Core, section, interval (cm)	Depth (mbsf)	pH	Salinity	Chloride (mM)	Sodium (mM)	Akalinity (mM)	Sulfate (mM)	Magnesium (mM)	Calcium (mM)	Potassium (mM)	Strontium (μM)
138-848A-1H-1, 145–150	1.5	7.35	34.8	555	483	2.941	28.13	53.25	10.66	10.9	86.9
1H-3, 145–150	4.5	—	34.5	555	484	—	28.04	53.19	10.57	11.1	86.5
1H-5, 145–150	7.5	—	35.2	556	485	—	27.62	53.02	10.33	11.0	94.8
-848B-3H-6, 145–150	20.7	7.29	35.8	559	487	2.915	28.40	53.54	10.86	11.1	112.7
6H-6, 145–150	49.2	7.32	35.8	562	488	2.914	28.99	53.82	11.06	10.7	116.9
7H-6, 145–150	58.7	7.31	36.0	561	485	2.880	28.43	54.08	11.04	10.7	111.7
8H-6, 145–150	68.2	7.33	35.8	560	484	2.854	27.75	54.54	10.42	10.7	108.7
9H-6, 145–150	77.7	7.48	35.2	557	482	2.817	28.16	53.64	10.84	10.7	100.5
10H-6, 145–150	87.2	7.34	35.2	558	485	2.452	27.81	52.62	10.81	10.5	95.2
11H-3, 145–150	92.2	7.36	35.2	550	476	2.372	27.75	53.46	10.22	10.7	91.0

Note: (—) indicates samples that were not measured.

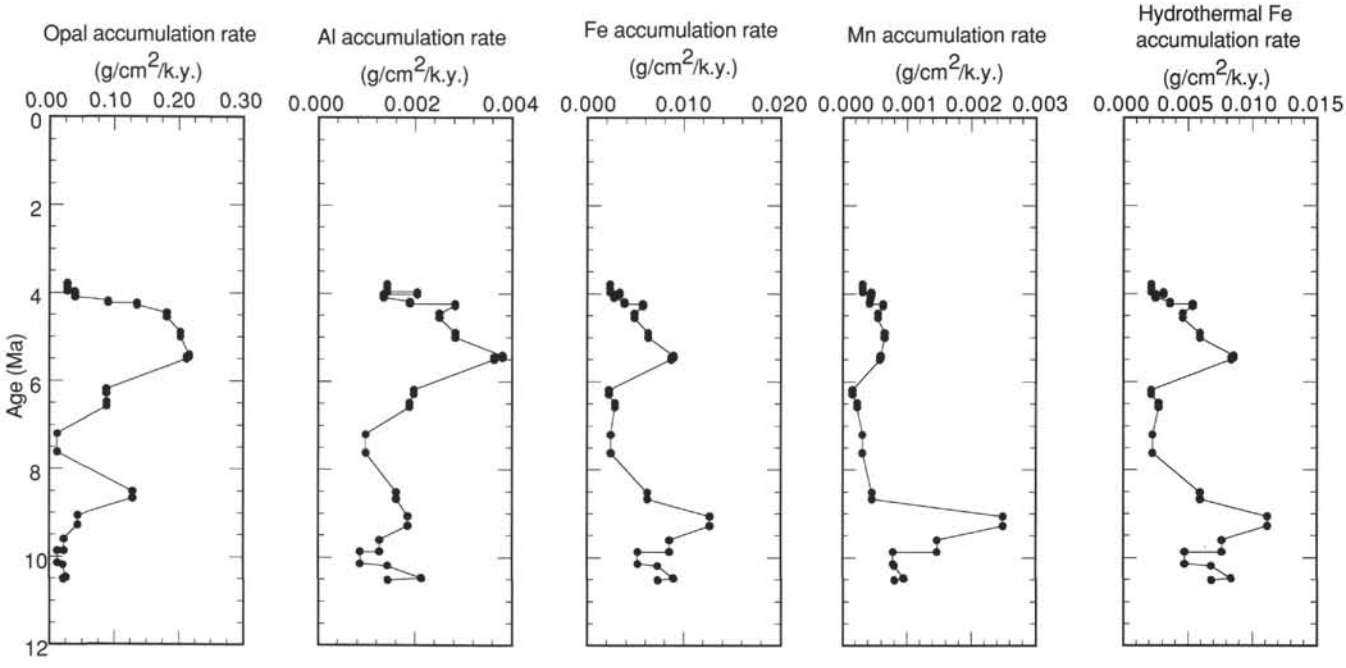

Figure 35. Accumulation rates (g/cm^2/k.y.) of biogenic silica (opal), Al, Fe, Mn, and the hydrothermal component of Fe.

Table 10 (continued).

Core, section, interval (cm)	Lithium (μM)	Silica (μM)	Ammonia (μM)
138-848A-1H-1, 145–150	26.5	888	<10
1H-3, 145–150	25.9	838	<10
1H-5, 145–150	25.2	869	<10
-848B-3H-6, 145–150	22.9	824	<10
6H-6, 145–150	22.1	851	<10
7H-6, 145–150	22.3	844	<10
8H-6, 145–150	23.2	809	<10
9H-6, 145–150	26.0	766	<10
10H-6, 145–150	26.6	694	<10
11H-3, 145–150	25.5	382	<10

Table 11. Changes in concentrations of interstitial-water constituents at Site 848 compared to the precision of these measurements.

Parameter	Units	Range[a]	Change (%)	Precision[b] (%)	Measurable change
Diagenesis					
Alkalinity	(mM)	2.817–2.941	4.2	3	Yes
Sulfate	(mM)	27.62–28.99	4.7	4	No
Ammonia	(μM)	<10		5	No
Crystallization					
Calcium	(mM)	10.33–11.06	6.6	2	Yes
Silica	(μM)	766–888	14	3	Yes
Strontium	(μM)	86.5–117	26	5	Yes
Lithium	(μM)	22.1–26.5	17	5	Yes
Alteration					
Magnesium	(mM)	53.02–54.54	1.5	1	No
Potassium	(mM)	10.7–11.1	3.6	5	No
Advection					
Sodium	(mM)	482–488	1.2	1.2	No
Chloride	(mM)	555–562	1.3	0.8	No

[a] Ranges for samples down through Sample 138-848-9H-6.
[b] Precisions are 2σ values.

Table 12. Bulk-sediment major oxide composition from X-ray fluorescence spectroscopy and loss on ignition in sediments from Hole 848C.

Core, section, interval (cm)	Depth (mbsf)	SiO_2 (wt%)	TiO_2 (wt%)	Al_2O_3 (wt%)	Fe_2O_3 (wt%)	MnO (wt%)	MgO (wt%)	CaO (wt%)	Na_2O (wt%)	K_2O (wt%)	P_2O_5 (wt%)	Total (wt%)	LOI (wt%)
138-848C-5H-1, 0–150	34.00	23.68	0.00	1.80	2.47	0.32	0.00	69.53	0.00	0.00	0.25	98.05	38.10
5H-2, 0–150	35.50	22.20	0.00	1.20	2.05	0.32	0.00	71.67	0.00	0.00	0.16	97.60	38.82
5H-3, 0–150	37.00	26.38	0.00	0.93	1.58	0.17	0.00	69.15	0.00	0.00	0.09	97.37	38.02
5H-6, 0–150	41.50	32.37	0.00	0.78	1.28	0.14	0.00	64.71	0.00	0.00	0.11	99.39	36.77
6H-3, 0–150	46.50	34.47	0.00	0.84	1.57	0.16	0.00	61.15	0.00	0.00	0.10	98.29	36.21
7H-1, 0–75	53.00	36.37	0.00	1.10	2.15	0.14	0.00	57.19	0.10	0.00	0.12	97.17	34.33
7H-1, 75–150	53.00	36.38	0.00	1.07	2.14	0.14	0.00	57.41	0.00	0.00	0.11	97.25	35.56
8H-2, 0–150	64.00	16.78	0.00	0.63	0.60	0.04	0.00	82.00	0.00	0.00	0.80	100.85	40.57
8H-5, 0–150	68.50	16.74	0.00	0.60	0.77	0.06	0.00	81.83	0.00	0.00	0.09	100.09	40.65
9H-3, 0–150	75.00	8.36	0.00	0.88	1.83	0.23	0.00	87.59	0.00	0.00	0.14	99.03	41.91
10H-1, 0–150	81.50	43.17	0.00	0.95	3.08	0.22	0.00	45.43	1.99	0.10	0.16	95.10	31.57
10H-3, 0–150	84.50	24.05	0.02	1.54	8.82	1.70	0.97	57.90	0.00	0.00	0.28	95.28	30.90
10H-5 ,0–150	87.50	15.00	0.00	1.19	6.66	1.13	0.00	72.08	0.00	0.00	0.27	96.33	38.60
10H-6, 0–150	89.00	8.74	0.00	0.82	4.14	0.61	0.00	83.67	0.00	0.00	0.16	98.14	39.24
11H-2, 130–132	90.50	15.12	0.02	1.39	5.92	0.64	0.00	74.26	0.00	0.00	0.29	97.64	39.12
11H-2, 0–150	91.00	18.65	0.07	1.99	6.98	0.73	0.00	67.37	0.00	0.00	0.34	96.13	37.02

LOI = loss on ignition.

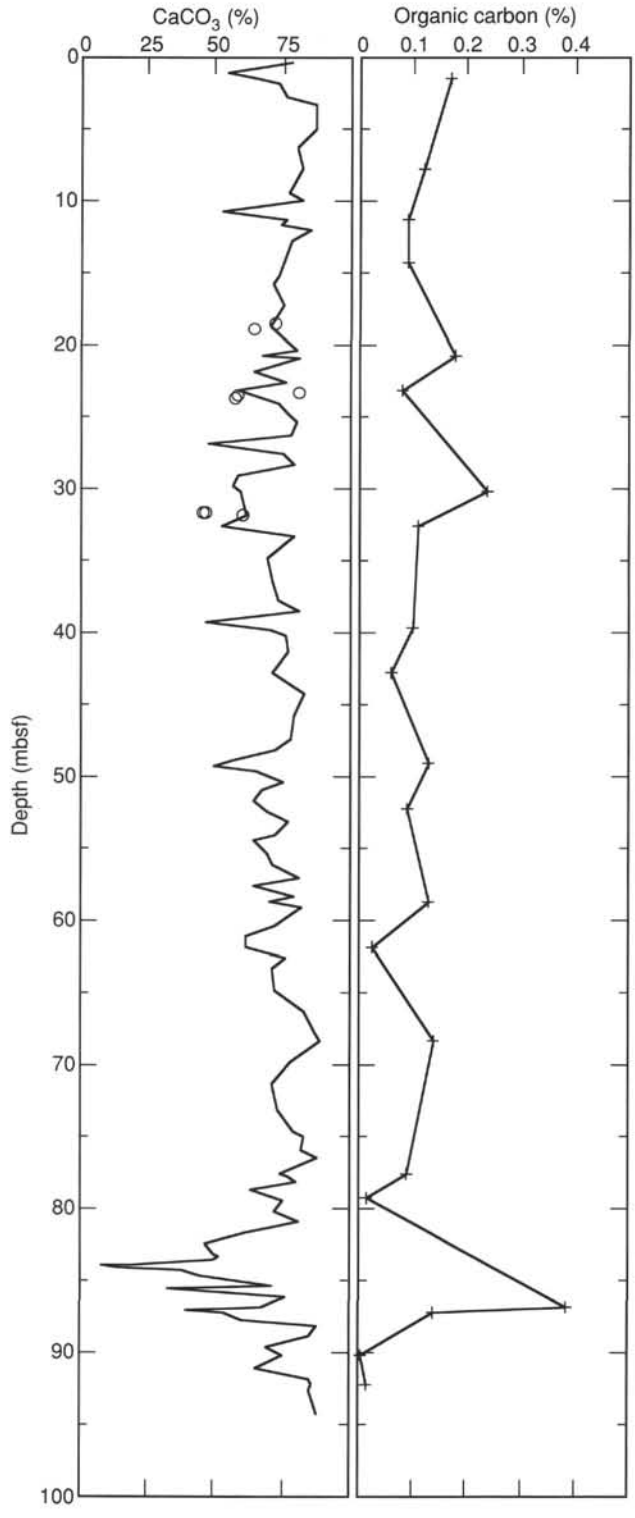

Figure 36. Downhole records of percentages of $CaCO_3$ (Hole 848D = open circles; Hole 848B = line) and C_{org} vs. ODP depth (mbsf) for Hole 848B.

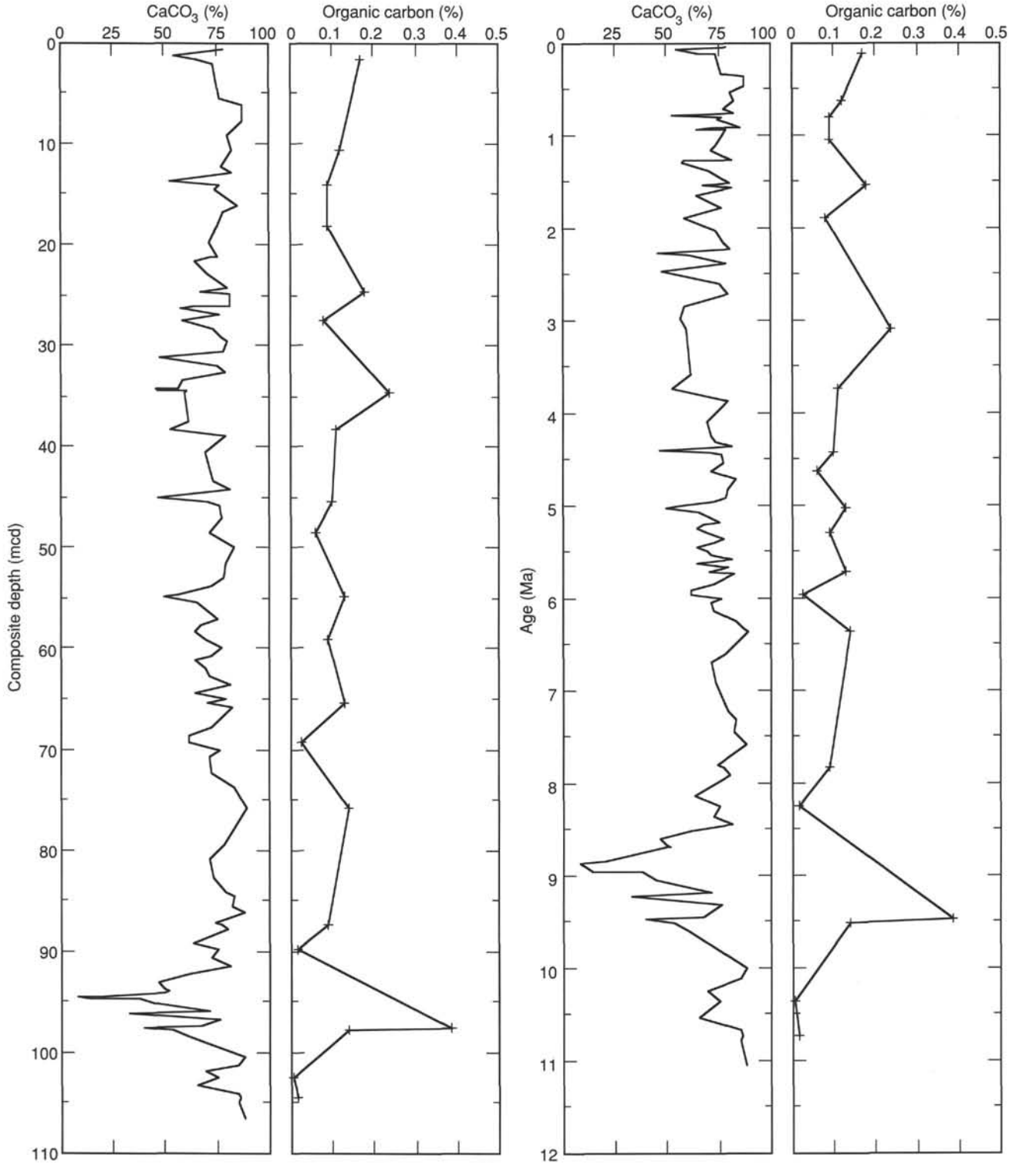

Figure 37. Plots of percentages of $CaCO_3$ and C_{org} vs. composite depth and age for Hole 848B.

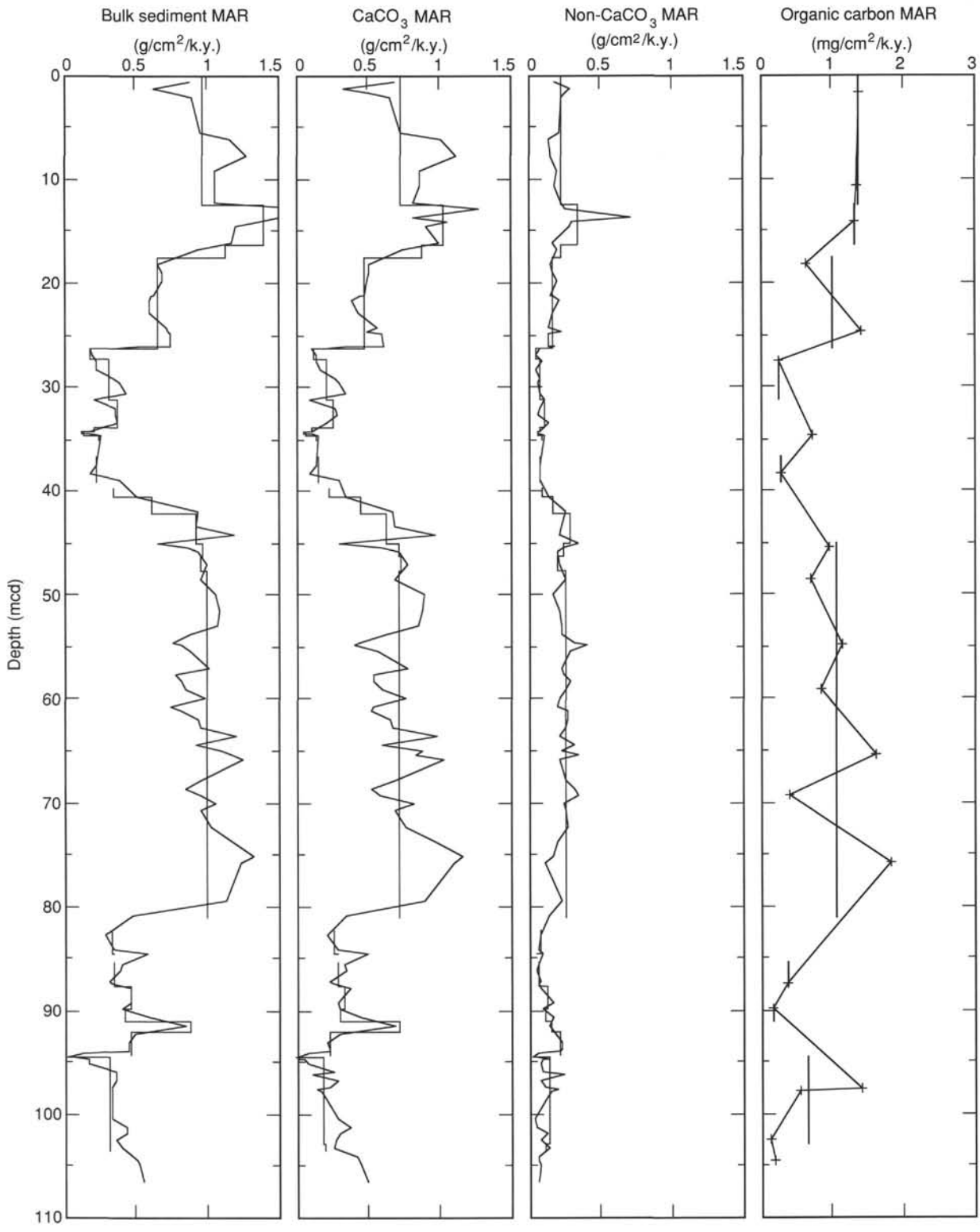

Figure 38. Mass accumulation rates of bulk sediment, $CaCO_3$, non-$CaCO_3$ (100%–$CaCO_3$%), and C_{org} sedimentary components vs. composite depth at Site 848. Note different units for C_{org}. Thick line indicates mean value between each stratigraphic datum plane; thin line shows discrete accumulation rates calculated for each sample.

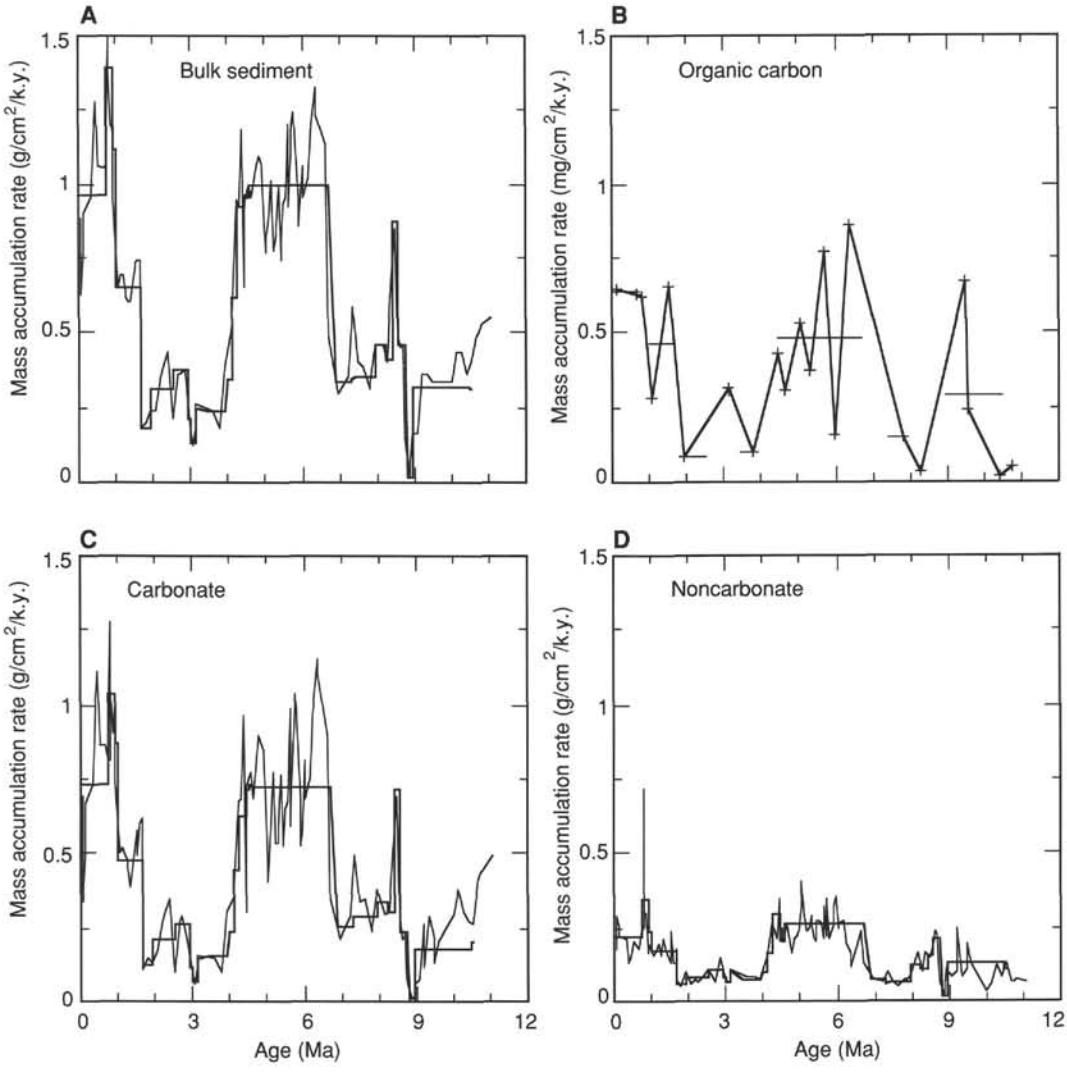

Figure 39. Accumulation rates of bulk sediment (**A**), C_{org} (**B**), $CaCO_3$ (**C**), and non-$CaCO_3$ (**D**) vs. age in sediments from Site 848. Thick line indicates mean value between each stratigraphic datum plane; thin line shows discrete accumulation rates calculated for each sample.

Table 13. Comparison of X-ray fluorescence normative $CaCO_3$ with coulometric $CaCO_3$ measurements.

Core, section, interval (cm)	Depth (mbsf)	CaO (wt%)	non-volatile (wt%)	LOI (wt%)	100%-LOI (wt%)	Ca in unignited sample (%)	Estimated wt% $CaCO_3$ in unignited sample	Measured wt% $CaCO_3$ in unignited sample
138-848C-5H-1, 0–150	34.00	69.53	98.05	38.10	61.90	30.76	76.81	71.95
5H-2, 0–150	35.50	71.67	97.60	38.82	61.18	31.34	78.25	74.82
5H-3, 0–150	37.00	69.15	97.37	38.02	61.98	30.63	76.49	71.78
5H-6, 0–150	41.50	64.71	99.39	36.77	63.23	29.24	73.02	71.03
6H-3, 0–150	46.50	61.15	98.29	36.21	63.79	27.88	69.61	65.46
7H-1, 0–75	53.00	57.19	97.17	34.33	65.67	26.84	67.03	63.01
7H-1, 75–150	53.75	57.41	97.25	35.56	64.44	26.44	66.02	
8H-2, 0–150	64.00	82.00	100.85	40.57	59.43	34.83	86.97	84.10
8H-5, 0–151	68.50	81.83	100.09	40.65	59.35	34.71	86.67	84.61
9H-3, 0–150	75.00	87.59	99.03	41.91	58.09	36.36	90.80	86.71
10H-1, 0–150	81.50	45.43	95.10	31.57	68.43	22.22	55.48	51.03
10H-3, 0–150	84.50	57.90	95.28	30.90	69.10	28.59	71.40	62.51
10H-5, 0–150	87.50	72.08	96.33	38.60	61.40	31.63	78.98	75.58
10H-6, 0–150	89.00	83.67	98.14	39.24	60.76	36.33	90.73	82.75
11H-2, 130–132	90.50	74.26	97.64	39.12	60.88	32.31	80.68	
11H-2, 0–150	91.00	67.37	96.13	37.02	62.98	30.32	75.72	76.85

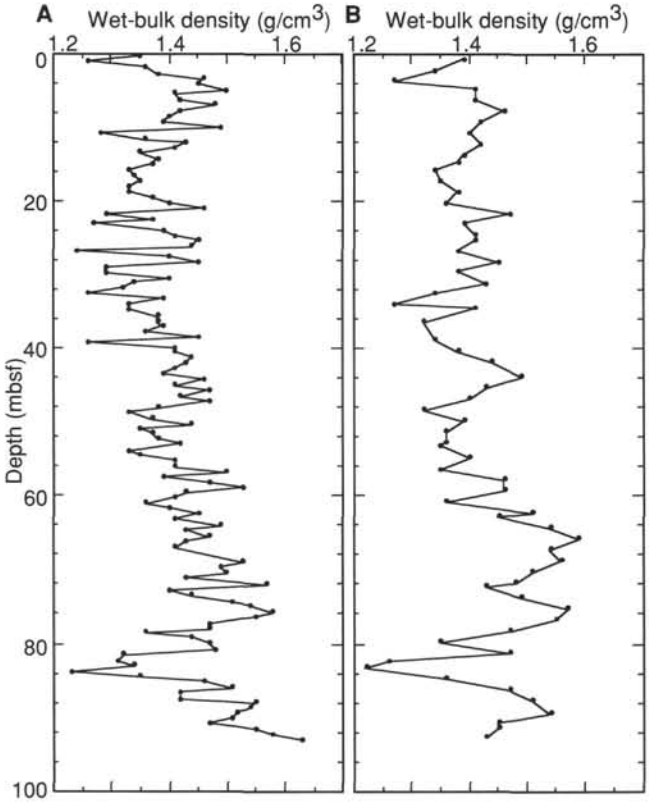

Figure 40. Plot of wet-bulk density vs. depth for Holes 848B (**A**) and 848C (**B**).

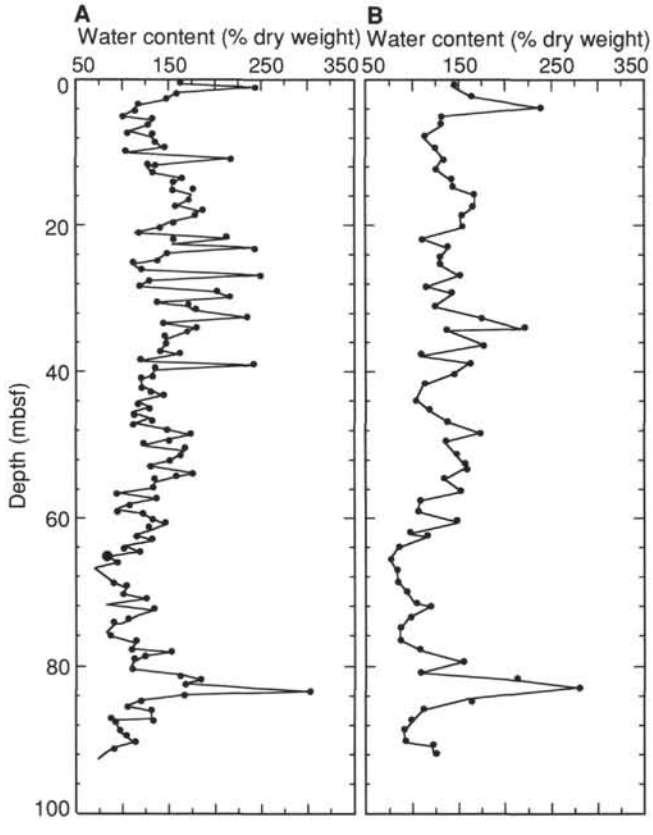

Figure 41. Plot of water content (%-dry weight) vs. depth, Holes 848B (**A**) and 848C (**B**).

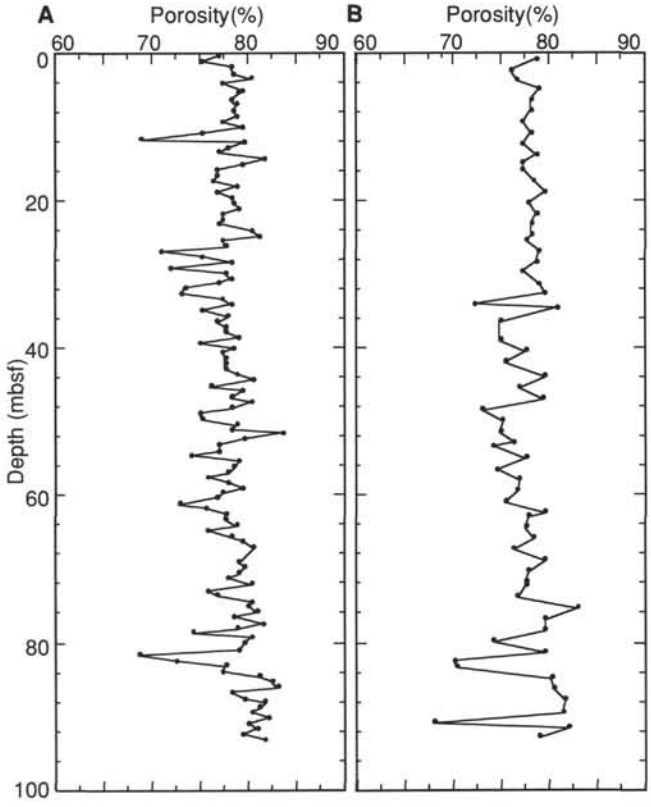

Figure 42. Plot of porosity vs. depth for Holes 848B (**A**) and 848C (**B**).

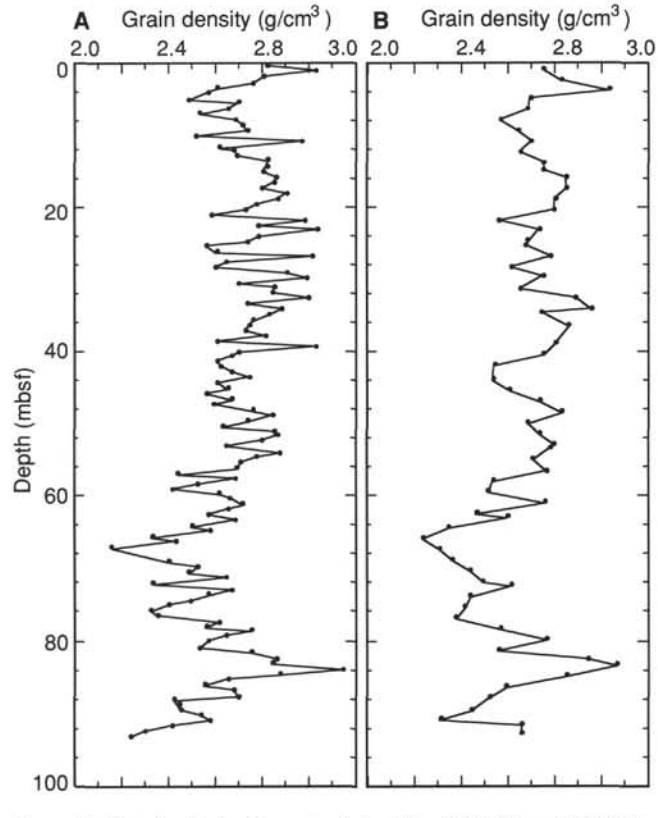

Figure 43. Plot of grain density vs. depth for Holes 848B (**A**) and 848C (**B**).

Table 14. Elemental composition in bulk-sediments and on a carbonate-free basis.

Core, section, interval (cm)	Depth (mbsf)	Al (wt%)	Si (wt%)	Ca (wt%)	Fe (wt%)	Mn (wt%)	Ti (wt%)	P (wt%)	est $CaCO_3$ (wt%)	Al (CF) (wt%)	Si (CF) (wt%)	Fe (CF) (wt%)
138-848C-5H-1, 0–150	34.00	0.59	6.85	30.76	0.97	0.13	0.00	0.29	76.81	0.14	6.84	0.22
5H-2, 0–150	35.50	0.39	6.35	31.34	0.79	0.13	0.00	0.18	78.25	0.08	6.34	0.17
5H-3, 0–150	37.00	0.30	7.64	30.63	0.62	0.07	0.00	0.10	76.49	0.07	7.63	0.15
5H-6, 0–150	41.50	0.26	9.56	29.24	0.51	0.06	0.00	0.13	73.02	0.07	9.56	0.14
6H-3, 0–150	46.50	0.28	10.27	27.88	0.63	0.07	0.00	0.12	69.61	0.09	10.27	0.19
7H-1, 0–75	53.00	0.38	11.16	26.84	0.89	0.06	0.00	0.15	67.03	0.13	11.15	0.29
7H-1, 75–150	53.00	0.36	10.95	26.44	0.87	0.06	0.00	0.13	66.02	0.12	10.94	0.30
8H-2, 0–150	64.00	0.20	4.66	34.83	0.23	0.02	0.00	0.86	86.97	0.03	4.66	0.03
8H-5, 0–150	68.50	0.19	4.64	34.71	0.29	0.02	0.00	0.10	86.67	0.03	4.64	0.04
9H-3, 0–150	75.00	0.27	2.27	36.36	0.67	0.09	0.00	0.15	90.80	0.02	2.27	0.06
10H-1, 0–150	81.50	0.34	13.80	22.22	1.33	0.10	0.00	0.22	55.48	0.15	13.78	0.59
10H-3, 0–150	84.50	0.56	7.77	28.59	3.86	0.76	0.04	0.40	71.40	0.16	7.75	1.10
10H-5, 0–150	87.50	0.39	4.30	31.63	2.59	0.45	0.00	0.31	78.98	0.08	4.30	0.54
10H-6, 0–150	89.00	0.26	2.48	36.33	1.59	0.24	0.00	0.18	90.73	0.02	2.48	0.15
11H-2, 130–132	90.50	0.45	4.30	32.31	2.28	0.25	0.03	0.32	80.68	0.09	4.30	0.44
11H-2, 0–150	91.00	0.66	5.49	30.32	2.78	0.30	0.11	0.40	75.72	0.16	5.48	0.68

cf = carbonate-free.

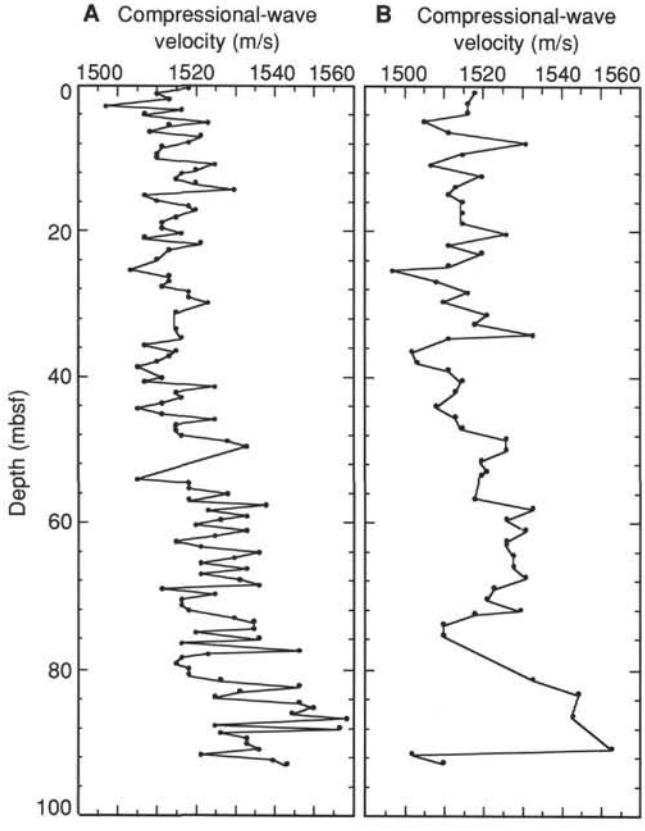

Figure 44. Plot of compressional-wave velocity vs. depth for Holes 848B (**A**) and 848C (**B**).

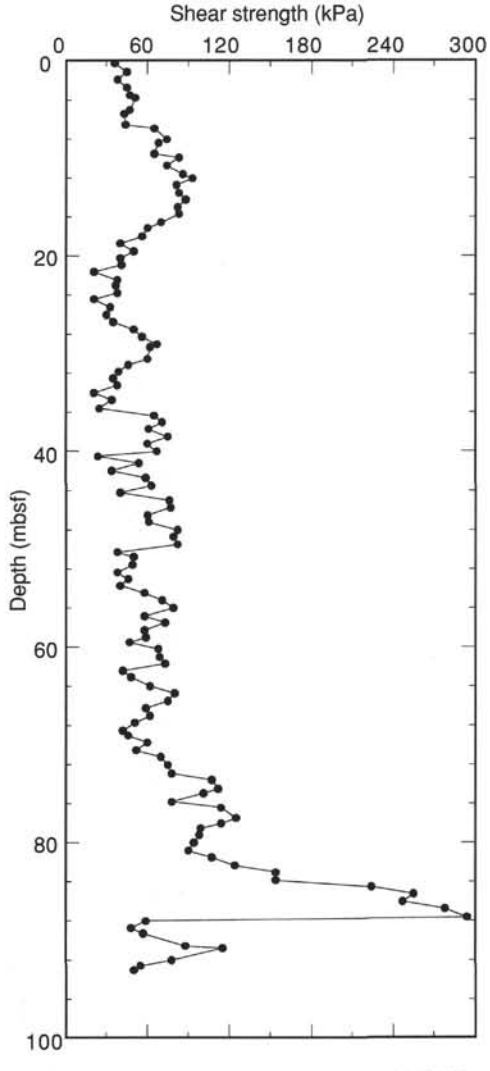

Figure 45. Plot of undrained shear strength vs. depth, Hole 848B.

Table 14 (continued).

Core, section, interval (cm)	Mn (CF) (wt%)	Ti (CF) (wt%)	P (CF) (wt%)
138-848C-5H-1, 0–150	0.13	0.00	0.29
5H-2, 0–150	0.13	0.00	0.18
5H-3, 0–150	0.07	0.00	0.10
5H-6, 0–150	0.06	0.00	0.13
6H-3, 0–150	0.07	0.00	0.12
7H-1, 0–75	0.06	0.00	0.15
7H-1, 75–150	0.06	0.00	0.13
8H-2, 0–150	0.02	0.00	0.86
8H-5, 0–150	0.02	0.00	0.10
9H-3, 0–150	0.09	0.00	0.15
10H-1, 0–150	0.10	0.00	0.22
10H-3, 0–150	0.76	0.04	0.39
10H-5, 0–150	0.45	0.00	0.30
10H-6, 0–150	0.24	0.00	0.18
11H-2, 130–132	0.25	0.03	0.32
11H-2, 0–150	0.30	0.11	0.40

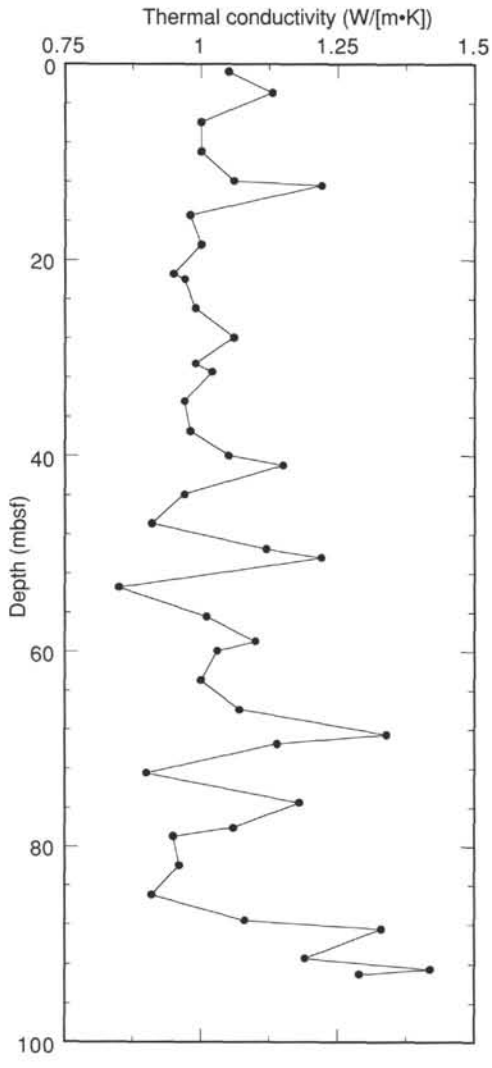

Figure 46. Plot of thermal conductivity vs. depth, Hole 848B.

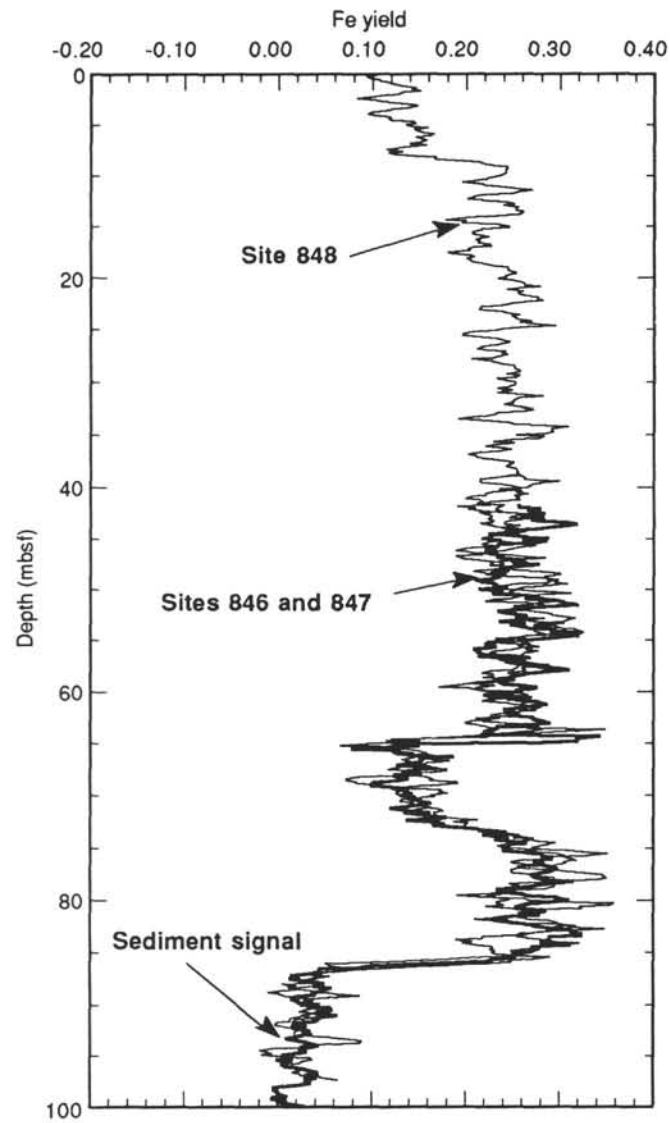

Figure 47. Comparison of Fe yields from the GST through the same BHA used at Sites 846, 847, and 848. Note that the correction to the sediment signal is large, but consistent from site to site. Data from Sites 846 and 847 have been depth-shifted to match those from Site 848.

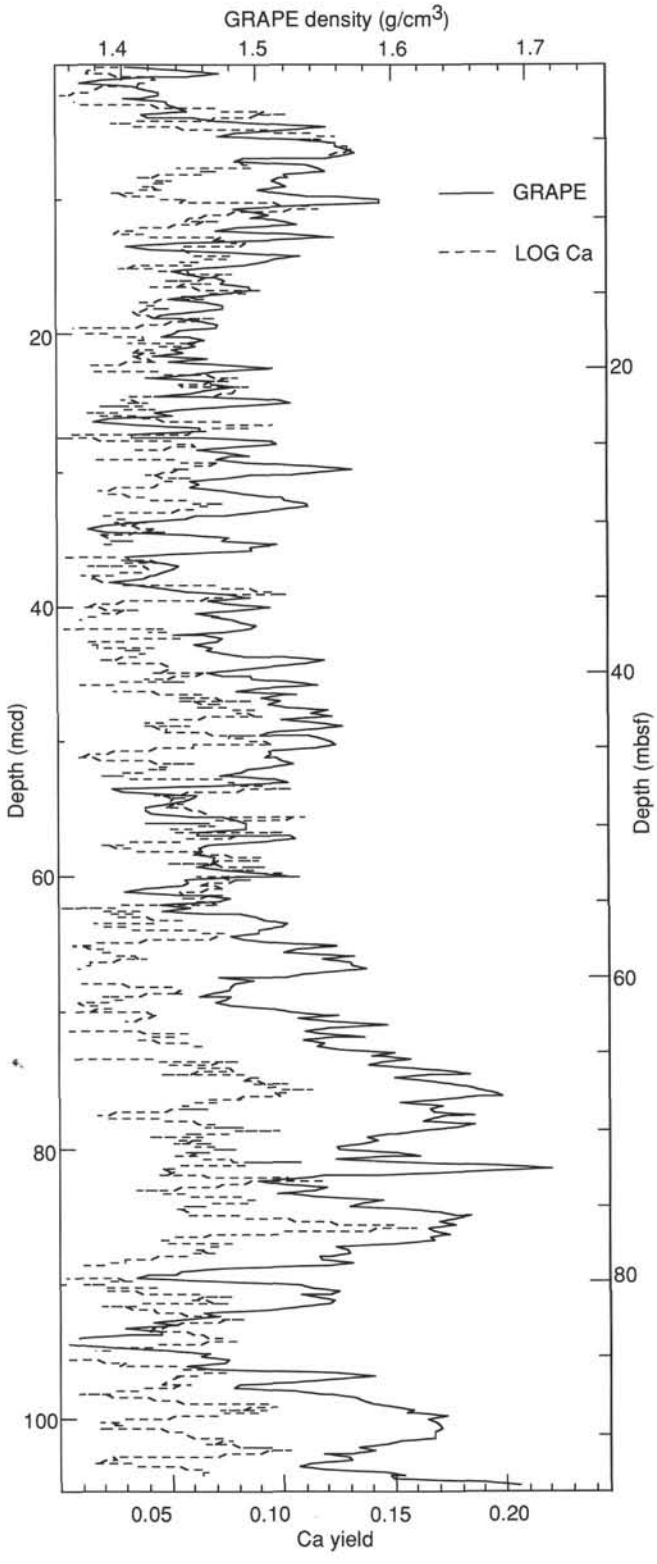

Figure 48. Comparison of Hole 846B GST Ca yields to composite GRAPE density profile from sediments at Site 848. Ca yield has been plotted vs. ODP depth (mbsf) and GRAPE density has been plotted vs. composite depth (mcd). GRAPE density reflects the calcite content of the sediments, with high density equivalent to high calcite. The two curves match reasonably well to about 60 mbsf, but then diverge below that depth. We consider that this divergence is the result of uncorrected effects of the BHA upon the Ca yield.

Table 15. Mass accumulation rates for selected elements and for opal.

Core no.	Depth (mbsf)	Depth (mcd)	Age (Ma)	Bulk MAR (g/cm²/k.y.)	Accumulation Rate (g/cm²/k.y.) Al	Fe	Mn	Fe (hydroth)	Opal
138-848C-5H-1	34.00	38.55	3.79	0.24	0.0014	0.0023	0.00031	0.0022	0.027
		39.00	3.88	0.24					
C-5H-1		39.00	3.88	0.24	0.0014	0.0023	0.00031	0.0022	0.027
		39.63	3.97	0.24					
C-5H-1		39.63	3.97	0.35	0.0020	0.0034	0.00044	0.0031	0.039
	35.50	40.05	4.03	0.35					
C-5H-2	35.50	40.05	4.03	0.35	0.0013	0.0028	0.00044	0.0025	0.039
	36.00	40.55	4.10	0.35					
C-5H-3	37.00	41.55	4.19	0.62	0.0019	0.0038	0.00042	0.0036	0.091
		42.10	4.24	0.62					
C-5H-3		42.10	4.24	0.93	0.0028	0.0057	0.00063	0.0054	0.135
	38.50	43.05	4.29	0.93					
C-5H-6	41.50	46.05	4.46	0.96	0.0025	0.0049	0.00055	0.0046	0.182
	43.00	47.55	4.56	0.96					
C-6H-3	46.50	52.85	4.90	1.00	0.0028	0.0063	0.00066	0.0059	0.203
	48.00	54.35	5.00	1.00					
C-7H-1, 0–75	53.00	60.75	5.41	1.00	0.0038	0.0089	0.00059	0.0086	0.217
	53.75	61.50	5.45	1.00					
C-7H-1, 75–150	53.75	61.50	5.45	1.00	0.0036	0.0087	0.00058	0.0084	0.213
	54.50	62.25	5.50	1.00					
C-8H-2	64.00	73.10	6.19	1.00	0.0020	0.0023	0.00015	0.0022	0.088
	65.50	74.60	6.29	1.00					
C-8H-5	68.50	77.60	6.48	1.00	0.0019	0.0029	0.00023	0.0027	0.088
	70.00	79.10	6.58	1.00					
C-9H-3	75.00	84.30	7.20	0.36	0.0010	0.0024	0.00031	0.0023	0.012
	76.50	86.30	7.62	0.36					
C-10H-1	81.50	92.25	8.52	0.47	0.0016	0.0062	0.00046	0.0060	0.129
	83.00	93.75	8.67	0.47					
C-10H-3	84.50	95.25	9.06	0.33	0.0019	0.0127	0.00249	0.0112	0.044
	85.75	96.50	9.28	0.33					
C-10H-5	87.50	98.25	9.60	0.33	0.0013	0.0085	0.00147	0.0076	0.023
	89.00	99.75	9.87	0.33					
C-10H-6	89.00	99.75	9.87	0.33	0.0009	0.0052	0.00079	0.0048	0.013
	90.50	101.25	10.14	0.33					
C-11H-2	91.00	101.75	10.19	0.32	0.0014	0.0073	0.00081	0.0068	0.021
	92.50	103.25	10.52	0.32					

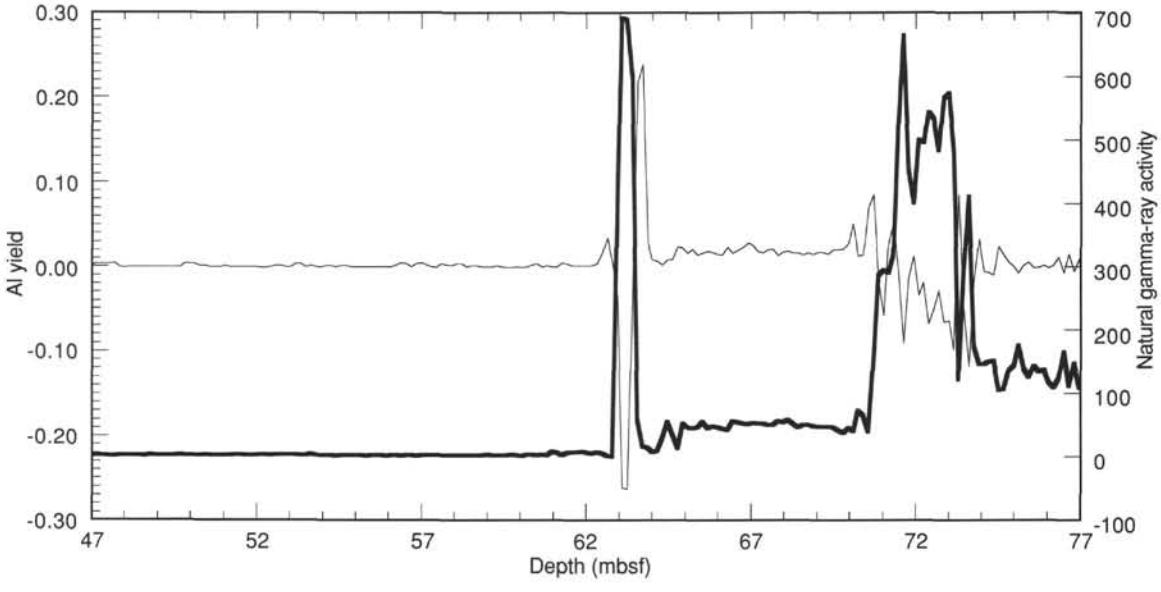

Figure 49. Correlation between high induced "natural gamma-ray" activity (thick line) and negative Al yields (thin line) measured by the NGT. High concentrations of Mn produce negative Al artifacts.

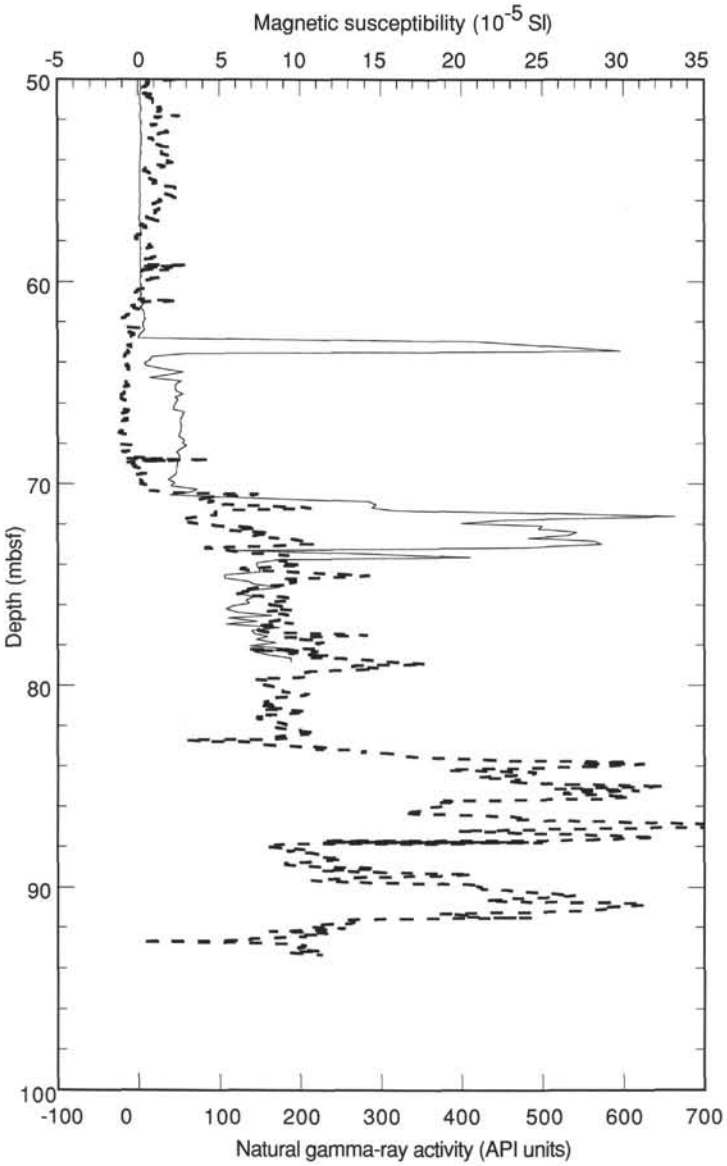

Figure 50. Comparison of gamma-ray activity (solid line) induced by activation of the borehole during tool calibration to sedimentary magnetic susceptibility (dashed line) measured in cores. Changes in magnetic susceptibility most probably reflect the metalliferous sediment content in the basal sediments, while the induced gamma-ray activity results from, in large part, the Mn content of the sediments. The large spike at 63.2 mbsf is where the tool was stopped during calibration. Sediments above this level were not activated and show baseline values for natural gamma-ray activity. Note the correlation between the step in natural gamma-ray activity and magnetic susceptibility at 70.5 mbsf, probably due to Mn in metalliferous sediments.

Table 16. Average values of sedimentary parameters calculated over time intervals defined by chronostratigraphic levels.

Composite depth (mcd)	Age (Ma)	Mean $CaCO_3$ (%)	Mean C_{org} (%)	Sediment rate (m/m.y.)	Mean DBD (g/cm^3)	Mean bulk MAR ($g/cm^2/k.y.$)	Mean $CaCO_3$ MAR ($g/cm^2/k.y.$)	Mean non-$CaCO_3$ MAR ($g/cm^2/k.y.$)	Mean C_{org} MAR ($mg/cm^2/k.y.$)
0.00	0.00								
12.45	0.73	76.67	0.15	17.05	0.57	0.97	0.74	0.23	1.4
16.20	0.91	74.74	0.09	20.83	0.67	1.40	1.04	0.35	1.3
17.45	0.98	78.59		17.86	0.63	1.13	0.88	0.24	
26.30	1.66	72.44	0.18	13.01	0.51	0.66	0.48	0.18	1.2
27.35	1.88	67.51		4.77	0.41	0.19	0.13	0.06	
31.15	2.47	70.03	0.08	6.44	0.49	0.32	0.22	0.09	0.2
33.85	2.92	71.62		6.00	0.63	0.38	0.27	0.11	
34.20	2.99	56.75		5.00	0.43	0.22	0.12	0.09	
34.50	3.08	51.41		3.33	0.41	0.14	0.07	0.07	
35.05	3.18	60.42	0.24	5.50	0.45	0.25	0.15	0.10	0.6
36.55	3.40			6.82					
39.00	3.88	64.87	0.11	5.10	0.47	0.24	0.16	0.08	0.3
39.63	3.97			7.00					
40.55	4.10	70.17		7.08	0.49	0.35	0.24	0.10	
42.10	4.24	71.92		11.07	0.56	0.62	0.45	0.17	
44.95	4.40	67.55		17.81	0.52	0.93	0.63	0.30	
46.20	4.47	74.01	0.10	17.86	0.54	0.97	0.72	0.25	1.0
47.65	4.57	77.76		14.50	0.66	0.96	0.74	0.21	
81.05	6.70	72.90	0.10	15.68	0.64	1.00	0.73	0.27	1.0
82.00	6.78			11.88					
82.25	6.85			3.57					
84.40	7.28	76.88		5.00	0.68	0.34	0.26	0.08	
84.70	7.35	83.84		4.29	0.82	0.35	0.29	0.06	
85.30	7.41			10.00					
87.60	7.90	80.92	0.09	4.69	0.78	0.36	0.29	0.07	0.3
89.70	8.21	72.09		6.77	0.70	0.47	0.34	0.13	
90.95	8.41	74.17	0.02	6.25	0.68	0.42	0.31	0.11	0.1
92.05	8.50	82.17		12.22	0.72	0.88	0.72	0.16	
94.15	8.71	52.20		10.00	0.47	0.47	0.24	0.22	
94.40	8.80			2.78					
94.50	8.92	14.98		0.83	0.30	0.02	0.00	0.02	
102.80	10.42	58.86	0.18	5.53	0.59	0.33	0.19	0.14	0.6
103.35	10.54	65.59		4.58	0.70	0.32	0.21	0.11	
103.65	10.59			6.00					

Note: See "Sedimentation Rates" section (this chapter) for details. Parameters are percentages of $CaCO_3$ and C_{org}; LSR = linear sedimentation rate; DBD = dry-bulk density; Bulk MAR = bulk mass accumulation rate. Other parameters are $CaCO_3$ MAR, non-$CaCO_3$ MAR (calculated as 100% – %$CaCO_3$), and C_{org} MAR.

Table 18. Duplicate analyses of percentage of $CaCO_3$ in samples from Site 848.

Core, section, interval (cm)	depth (mbsf)	depth (mcd)	First run $CaCO_3$ (%)	Second run $CaCO_3$ (%)	Absolute value of $CaCO_3$ (difference)
138-848B-1H-1, 33–35	0.34	0.54	79.17	78.76	0.42
1H-1, 103–105	1.04	1.24	54.84	54.42	0.42
2H-4, 104–106	7.75	10.55	82.84	81.84	1.00
2H-6, 23–25	9.94	12.74	82.76	83.67	0.92
2H-6, 102–104	10.73	13.53	51.42	54.67	3.25
4H-1, 50–52	21.71	26.06	66.01	64.09	1.92
4H-1, 126–128	22.47	26.82	76.34	77.51	1.17
4H-2, 34–36	23.05	27.40	58.92	60.00	1.08
4H-4, 104–106	26.75	31.10	48.34	48.42	0.08
-848D-4H-3, 123–124	31.64	34.24	46.00	46.09	0.08
4H-3, 127–128	31.68	34.28	47.00	47.25	0.25
4H-3, 146–147	31.87	34.47	60.84	61.25	0.42
5H-6, 104–106	39.25	44.90	46.92	47.34	0.42
6H-6, 104–106	48.75	54.45	55.17	58.42	3.25
8H-2, 104–106	61.75	69.20	62.17	62.17	0.00
10H-4, 115–117	83.86	94.46	9.17	9.08	0.08
10H-5, 104–106	85.25	95.85	71.92	71.59	0.33
10H-6, 104–106	86.75	97.35	68.01	68.84	0.83
Average					0.88

Note: The average difference between the original and the duplicate analyses was 0.9% for %$CaCO_3$. The average value of the original and the duplicate analyses is reported in Table 17.

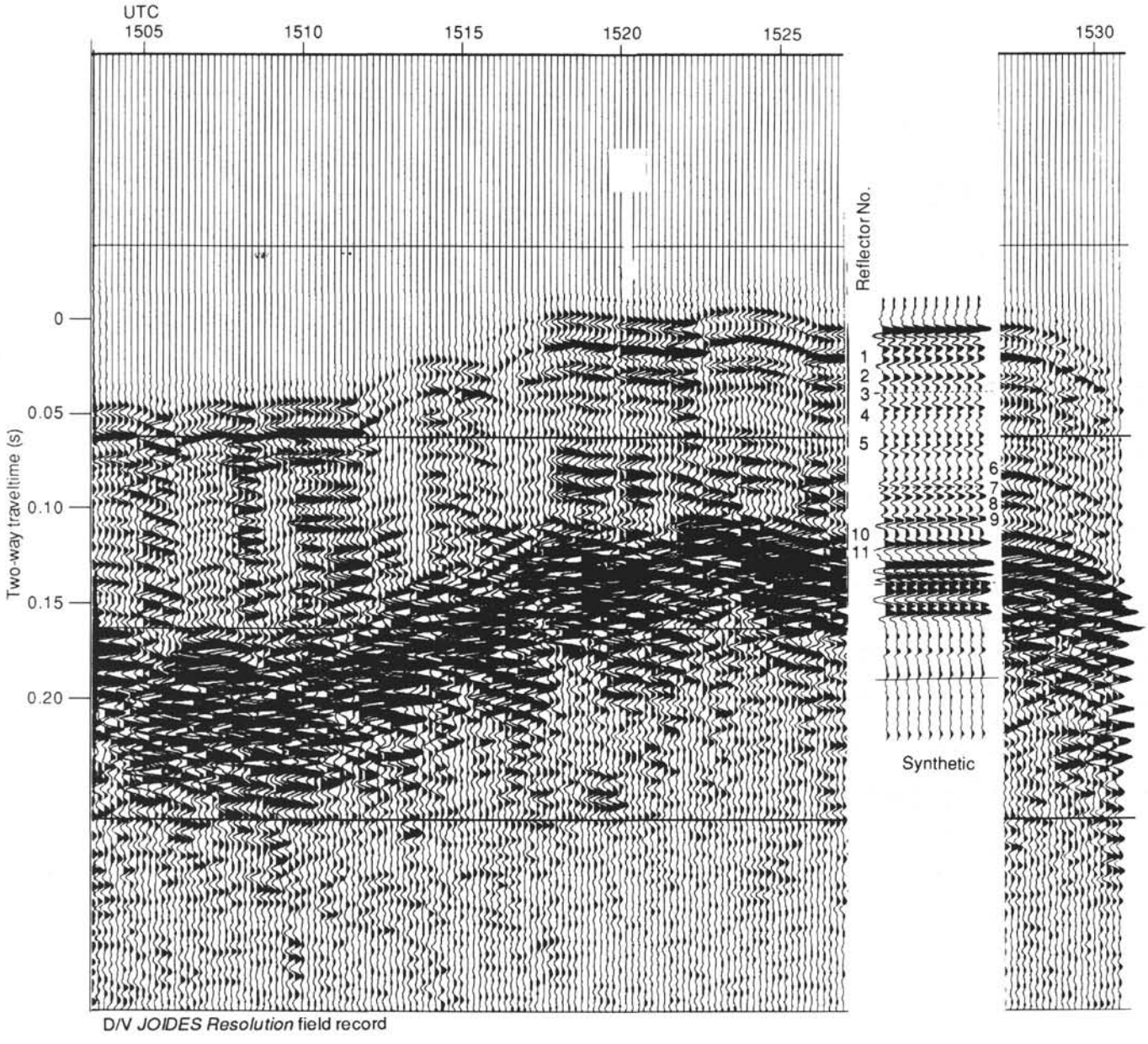

Figure 51. Comparison of synthetic seismogram with field record, Site 848.

Table 19. Concentrations of methane in sediments of Hole 848B.

Core, section, interval (cm)	Depth (mbsf)	Methane (μL/L)
138-848B-1H-1, 145–150	1.45	1.2
2H-6, 145–150	11.45	2.4
3H-6, 145–150	20.65	2.5
4H-6, 145–150	30.15	1.0
5H-6, 145–150	39.65	0.4
6H-6, 145–150	49.15	1.6
7H-6, 145–150	58.65	1.2
8H-7, 0–5	68.20	1.5
9H-6, 145–150	77.65	0.0
10H-6, 145–150	87.15	3.1
11H-3, 145–150	92.15	4.5

C_{org} and $\%CaCO_3$ were measured in sediment samples used for gas desorption.

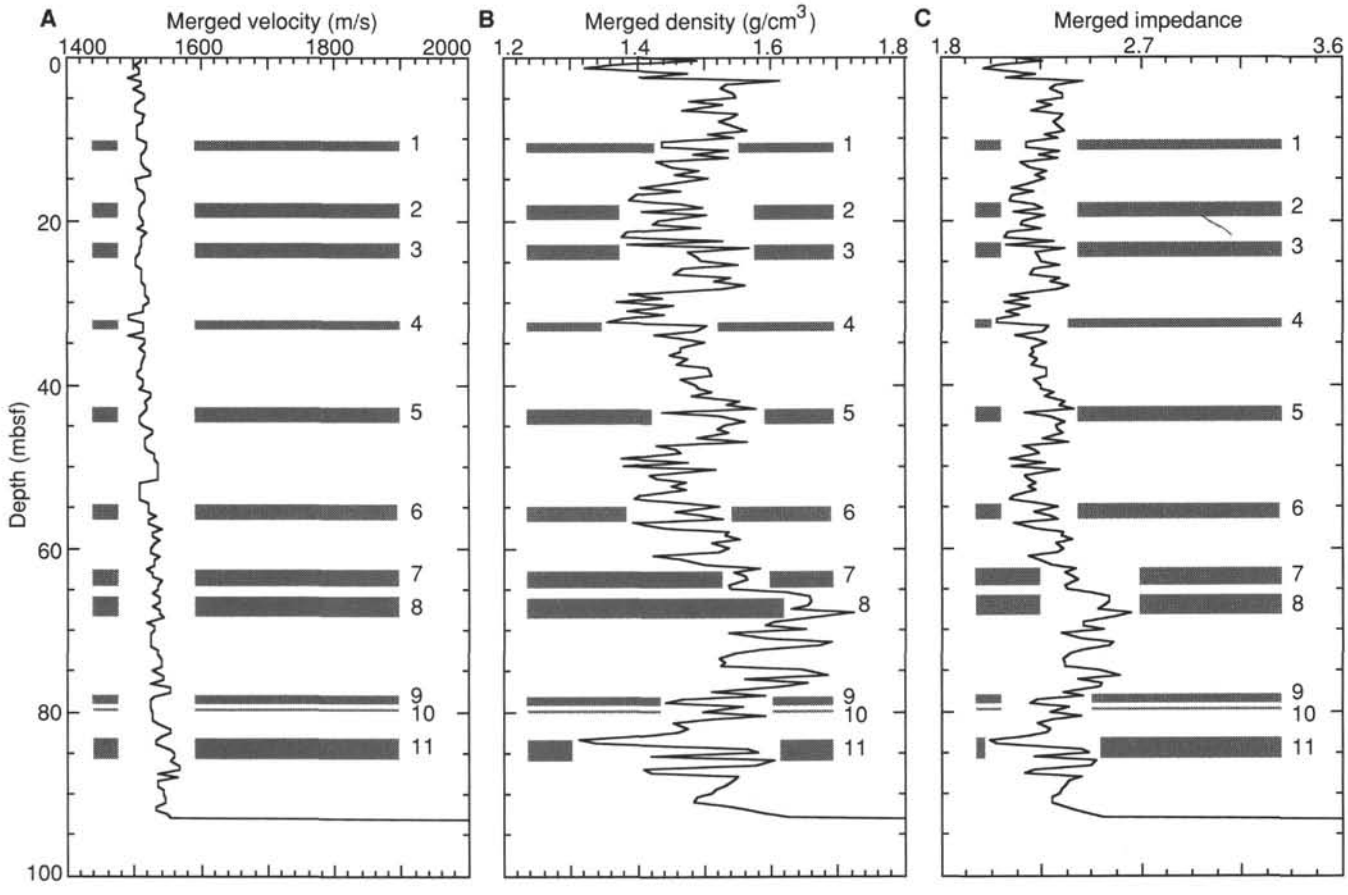

Figure 52. Date used for generating Site 848 synthetic seismograms. **A.** Velocity. **B.** Density. **C.** Acoustic impedance. The 11 reflectors selected from the synthetic seismogram are shown for comparison.

Table 24. Summary of traveltimes, depths, and ages for Site 848 reflectors.

Reflector	Traveltime (s)	Synthetic depth (m)	Depth (mbsf)	Depth (mcd)	Age (Ma)
R1	0.014	10.50	10.20	13.00	0.76
	0.017	12.80	11.50	14.30	0.82
R2	0.024	18.10	18.00	22.00	1.33
	0.027	20.40	19.50	23.50	1.44
R3	0.030	22.70	22.50	26.90	1.78
	0.034	25.70	24.50	28.90	2.12
R4	0.041	30.90	32.00	37.65	3.62
	0.047	35.30	33.50	39.15	3.90
R5	0.055	41.50	42.50	48.20	4.61
	0.059	44.50	44.50	50.20	4.73
R6	0.072	54.40	54.20	60.90	5.41
	0.076	57.50	56.50	63.20	5.56
R7	0.082	62.10	62.50	70.00	5.99
	0.085	64.40	64.50	72.00	6.12
R8	0.087	65.90	66.00	73.45	6.21
	0.090	68.20	68.00	75.50	6.34
R9	0.099	75.10	77.00	86.60	7.69
	0.103	78.20	78.50	89.10	8.13
R10	0.105	79.70	79.00	89.60	8.20
	0.109	82.80	80.00	90.60	8.36
R11	0.111	84.30	83.00	93.60	8.66
	0.114	86.70	86.00	96.60	9.30

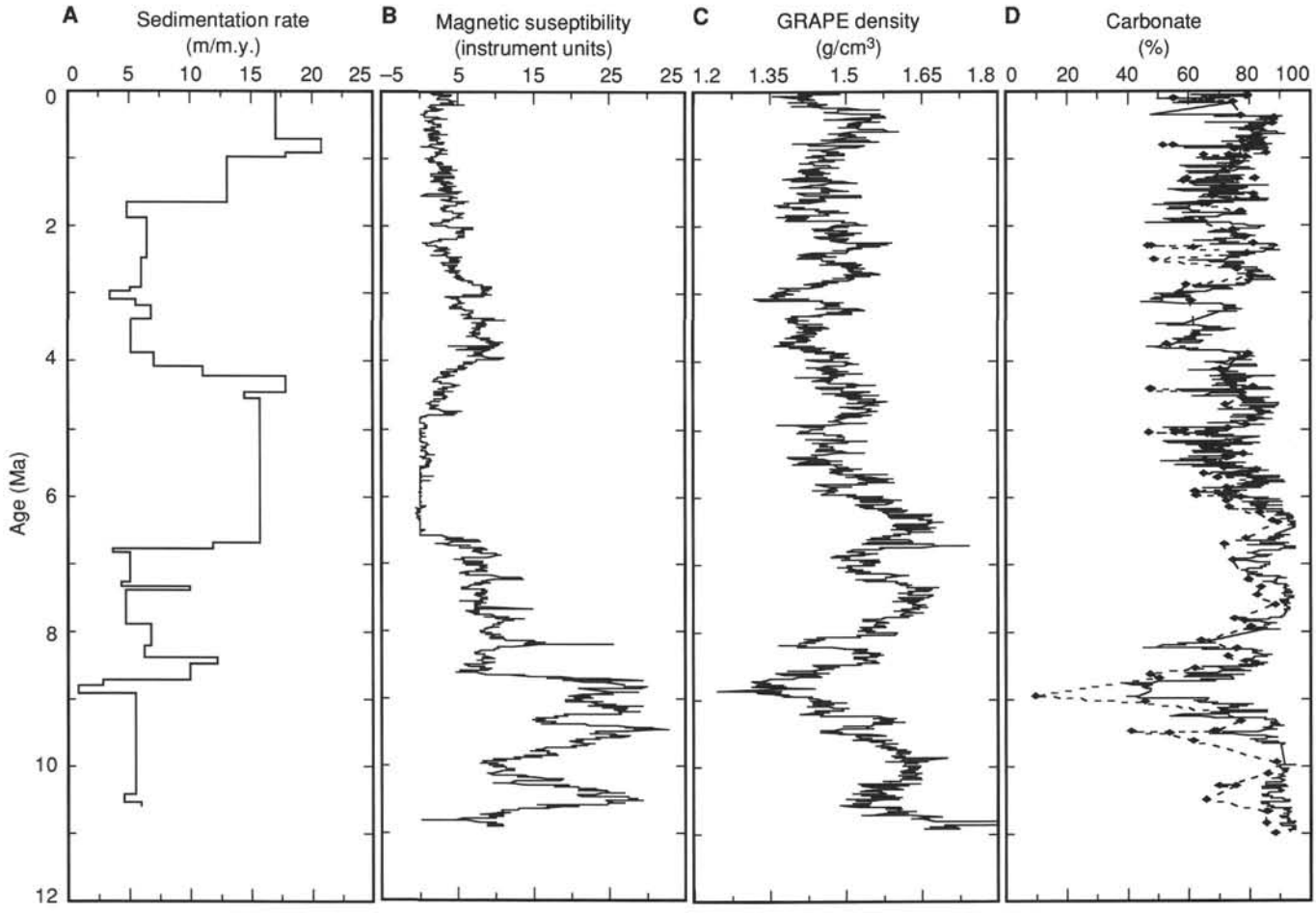

Figure 53. **A.** Sedimentation rate vs. sediment age. **B.** Sediment magnetic susceptibility vs. age. **C.** Sediment density vs. age. **D.** Carbonate content (predicted = solid line; core measurement = dashed line with symbol) vs. age.

Table 25. Backtracked path of Site 848 using pole of rotation.

Age (Ma)	Latitude (°S)	Longitude (°W)
1	3.25	109.72
2	3.50	108.95
3	3.75	108.17
4	3.99	107.39
5	4.23	106.61
6	4.47	105.83
7	4.71	105.05
8	4.94	104.27
9	5.17	103.48
10	5.39	102.70

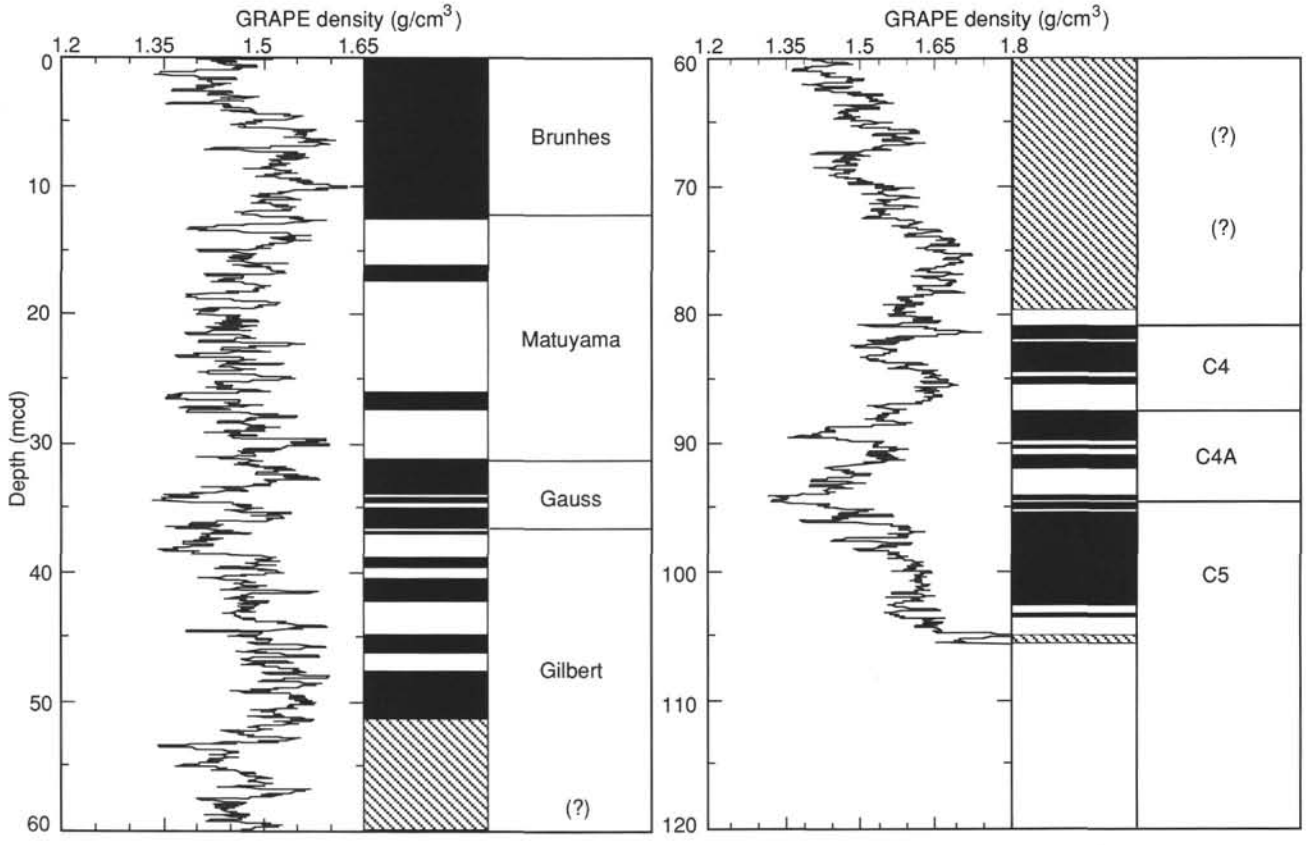

Figure 54. Spliced GRAPE density record vs. composite depth shown with results of paleomagnetic studies of all four holes at Site 848. The spliced record was constructed by selecting from each of the four holes drilled the core that contained the most representative GRAPE record within any depth interval. Data were smoothed with a nine-point Gaussian filter.

Hole 848B: Geochemical Log Summary

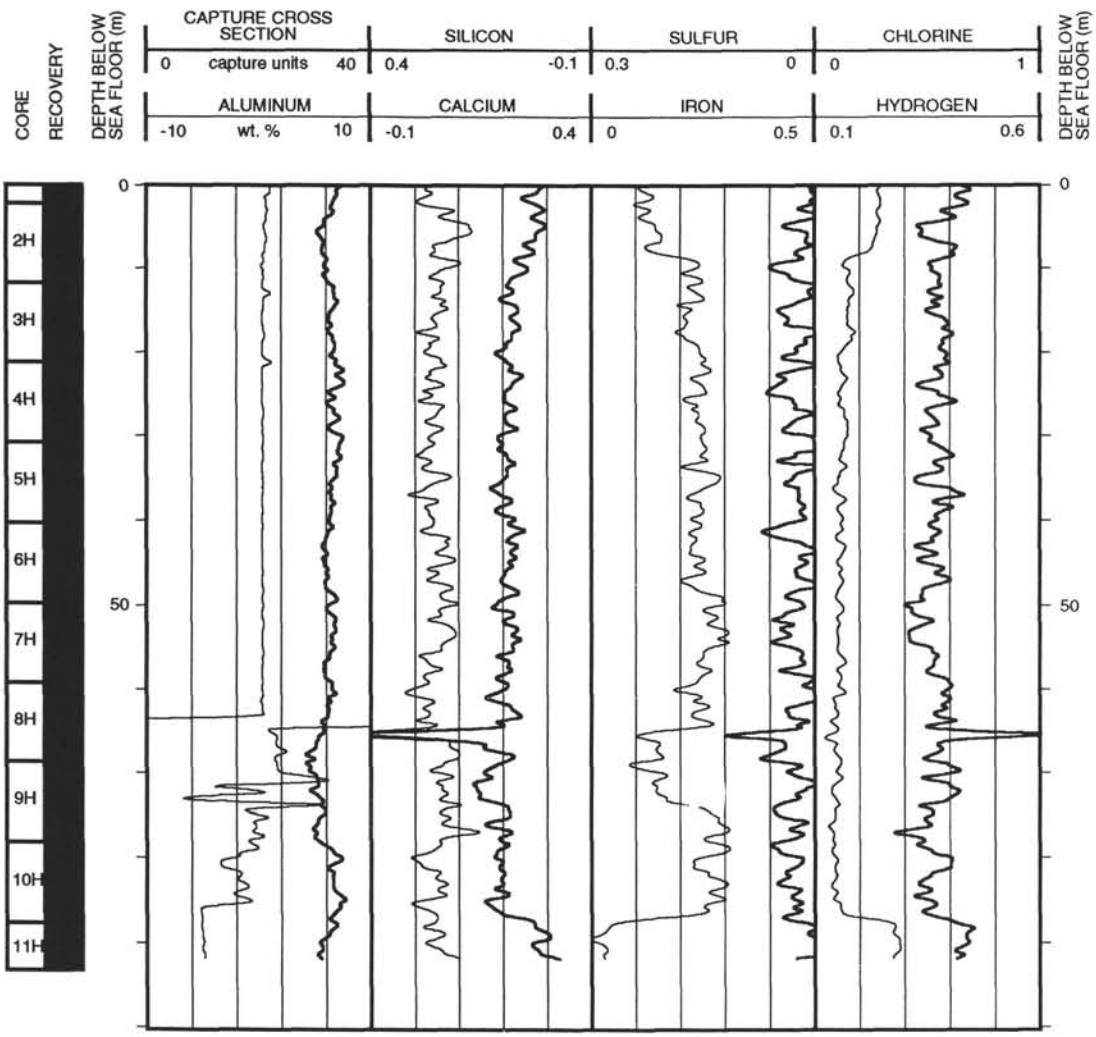

Hole 848B: Natural Gamma Ray Log Summary